POLYTECHNIC OF TURIN

College of Chemical and Materials Engineering

Master's degree
in Chemical Engineering and Sustainable Processes

Master Thesis

PA12 Multi Jet Fusion 3D printed samples: dependence of chemical, thermal and mechanical properties by printing direction, position inside the JOB and accelerated aging

Supervisors:

Prof. Sangermano Marco
Prof. Rosso Carlo
Prof. Bonisoli Elvio
Dr. Conigliaro Christian

Candidate:

Rapalino Rachele

December 2022

I would like to thank all the colleagues in Valeo Santena for having welcomed me for almost a year in their offices and offering me the possibility of carrying out this project, giving me the support that I needed. I would highlight a great APU Quality and Laboratory Manager, Christian Conigliaro, for sharing his knowledge about 3D Printers with me, for his professionalism and for his unconditional support even in difficult times.
A big thank also goes to Raquel Mayor, R&I and Valeo Group Additive Manufacturing Manager, and all her colleagues in Valeo Martos, which shipped to me all the samples I needed to support this study.

Index

Abstract

This study is devoted to broaden the knowledge on the conformity and applicability of the components produced through the Additive Manufacturing technology created by the company HP Inc., the Multi Jet Fusion (MJF). This research was defined and developed with the collaboration of three entities: Valeo Santena, Polytechnic of Turin and Valeo Martos. Valeo, a multinational in the automotive field, has been using these types of processes for rapid prototyping, for about 30 years. In recent years, Valeo Santena has been looking to take this technology to the next level: series production.

The purpose is to analyse the evolution of the chemical, thermal and mechanical properties of Polyamide 12 (PA12) components, 3D printed with MJF 4200, in relation to their position in the printing area, orientation and aging. Assuming the specimen's characteristics as symmetrical in the printing area, three points considered cruxes are analysed. The samples, with their dimensions dictated by the specific standards, are printed in these points, and with different printing orientations. Regarding accelerated aging, the *"Environmental specification for electrical/electronic (E/E) components"* is followed, relating to Valeo Santena product line, the "Interior Switches and Control" (ISC). This means that the specimens, tested in a climatic chamber where Temperature and Humidity are controlled, are inspected at ⅓ and at the end of the vehicle's life. The typical service life target refers to the 95th percentile of customer usage over the period of 10 years, which means 150.000 miles, or 15 years, depending on the device application.

The material is characterized by means of infrared spectrophotometry in attenuated total reflectance (FTIR-ATR), to examine the functional groups. The thermal analysis used is differential scanning calorimetry (DSC). As for the mechanical tests, the evolution of Young modulus (E), elongation at break, yield and ultimate tensile strength, are observed through the tensile testing. The maximum load and stroke at break, through the three-point bending flexural test. To determine the notch toughness of the material, the Izod impact strength test is also carried out, designing the indenter and the base with the annexed vise. Lastly, the hardness with a Shore durometer type D and the microindentation hardness testing with the Vickers indenter.

1. Introduction

High customer demand for variety, rising expectations, and nearly constant innovation, define today's product development scene. In this competitive market, where time is getting shorter, Additive Manufacturing (AM) gives the possibility to meet and exceed new release timelines in their product development cycles. These types of methods, which differ in how the different layers of material are moulded, enable the direct fabrication of actual objects from digital models, also with incredibly complex shapes (Wang, Y. et al., 2020). For this reason, they have been used mainly as rapid prototyping technology for decades. This study is dedicated to the readers who dream about the transition from prototype to serial production, for the Additive world.

Currently, no approach satisfies all market demands for manufacturing, each has its own advantages and disadvantages, but one technology has taken the first step toward this goal: *HP Multi Jet Fusion Industrial 3D Printing Solution (MJF)*. This powder bed 3D printing system provides new opportunities for industries. It is faster, more precise and produces more constant mechanical properties throughout the part. MJF leads to a reduction in production costs and, thanks to its process, reduces material wastage (Singh, A.P. and Pervaiz, S., 2021).

Existing studies regarding this technology focus on the mechanical and thermal properties that raw objects overcome after printing (O'Connor et al., 2018, Alomarah, A. et al., 2019, Rosso, S. et al., 2020). Valeo, a multinational in the automotive sector that is used to investing in innovation, has seized the opportunity to expand this research, to draw closer and closer to mass production. This company understands that this step is not immediate, it must be faced in a pragmatic and structured way, achieving a reliable process and production volumes. Therefore, the goal of this thesis is to broaden knowledge on the compliance and applicability of Polyamide 12 (PA12) components, produced through Multi Jet Fusion, in the automotive world. In this sector the specifications for validating the different types of products are clear and defined. For the components handled by Valeo Santena, electrical/electronic (E/E) ones, the corresponding FCA specification is CS.00056 (FCA US - Quality & Reliability Engineering - 5200 and FCA ITALY - Electrical/Electronics - Electronic Architecture, Talevski, M. and Molina, A., 2015). Valeo estimated the accelerated aging testing as the most useful and critical evidence to carry out, to evaluate the effective applicability of this technology through time. This simulates the behavior of the product at the end of the vehicle's life through testing in a climatic chamber at high temperature and humidity, for 700 hours. Furthermore, if the target is to generate the number of pieces needed for series production, it is likely to optimize the moulding times, filling the entire work area of the printer. For this reason, it is necessary to become aware of the difference in dimensional characteristics and properties that may exist between the various areas of the machine, in order to assess if these fall within the allowed tolerance. Finally, this technology has been considered by HP Inc. itself (HP Inc., 2020, 2022) as isotropic, or rather, with mechanical characteristics independent of the printing direction. The thesis wants to verify the effectiveness of this assertion in the most thermally stressed region, that is in the first layers, in contact with the mobile surface of the Build Unit. Therefore, in short, the study analyses the evolving chemical, thermal, and mechanical properties of 3D-printed PA12 components in relation to their location in the printing area, orientation, and aging. The research was performed on standard specimens, to eliminate the dependence on geometry. The samples have not been treated with post-processing processes, such as chemical attacks, which can alter the durability and mechanical characteristics. Valeo Santena collaborated with the Polytechnic of Turin, which owns appropriate mechanical, chemical and thermal equipment for the characterization. The standards developed by the US standardization organism ASTM

International have been adopted (American Society for Testing and Materials International, 2017, 2008, 2013, 2014, 2017, 2010, 2015).

The thesis is structured into five chapters: the introduction with the state of the art, the definition of the case study, the explanation of the procedures followed, the results and the general conclusion. In the first chapter, after a brief overview of Valeo's Additive Manufacturing path and its history, the readers are brought into this world. There are listed the advantages and disadvantages of this type of process and those that thus far are the options that can be obtained. To better understand the innovative potential of Multi Jet Fusion 3D Printing, it's reported the classification of AM techniques according to the starting material. Below, the operating procedure of the 3D printer of interest, the units that compose it and the advantages of its use, can be found in detail. Regarding the material employed, Polyamide 12 (PA12), its chemical and morphological characteristics and information regarding the production process have been listed. Since this is a semi-crystalline-crystalline thermoplastic polymer, useful definitions can be found, to better understand the analyses and the results obtained.

Entering the heart of the study, the reader finds how the project was defined and developed: the description of the case study in more detail, with the scenarios examined and the assumptions made. In addition, in this second chapter, it is also possible to obtain technical information on the printing phase: printing machine settings, the material used, and the size and quantity of printed specimens. In the corresponding sub-chapter, the dimensional characterization of the printed samples is found to obtain the capability, or rather, the repeatability and accuracy of the process.

In the third chapter, on the other hand, readers can find out the experimental methodologies that are the basis of the work, through the description of the instrumentation and procedures used, referring to the ASTM standards followed.

In the fourth chapter, the presentation and discussion of the results will follow, with the help of graphs and tables. This part has been divided, like the previous chapter, into three macro-chapters corresponding to the type of tests performed. The first concerns the means of infrared spectrophotometry analysis in attenuated total reflectance (FTIR-ATR); the second the thermal analysis, the differential scanning calorimetry (DSC); in the third there are the mechanical ones: tensile testing, three-point bending flexural test, Izod impact strength test and hardness tests, with a Shore durometer type D and the Vickers indenter. In each one, the readers find out the results divided by the variables analysed: position in the printing area, orientation perpendicular or parallel to the flat surface and aging stage, with the corresponding description.

Lastly, the conclusions, where is recalled the method of reasoning followed in the work, reported the most important results that emerged and mentioned the possible future developments of the research.

In the attachment are reported the drawing tables of the indenter and the base with the annexed vise, projected and used for the Izod impact strength test.

1.1 Valeo

1.1.1 A bit of History

Valeo is a French multinational in the automotive sector founded in 1923 nearby Paris, which has become a leader in the clutch segment. Around the sixties, it diversifies the range of its products with the production of braking systems, thermal systems and, subsequently, lighting and electrical systems.

As his website illustrates (Valeo S.p.a, 2021), in 1974, driven by innovation and increasing specialization, the Study and Research Centre of Santena (Turin) was inaugurated to guarantee customers an increasingly technically advanced product at competitive prices. In

September 2014, the production and staff of the Valeo plant in Felizzano were transferred to Santena, expanding the activity of the site with the introduction of the area production, in addition to that one dedicated to the aftermarket sector (Valeo Service Italy S.p.A.).

Nowadays Valeo Group is located all over the world, especially in Europe and Asia. It touches the car at 360 degrees and is divided into main business groups: “Comfort and Driving Assistance Systems”, “Powertrain Systems”, “Thermal Systems”, “Visibility Systems” and “Valeo Service”. In Italy, this company includes 4 production sites, of which 3 plants in Piedmont and 1 in Lazio, 3 research centres and 1 distribution platform.

Figure 1.1: Valeo Logo*, by Valeo S.p.a, 2021*

1.1.2 Additive Manufacturing in Valeo

In all these business groups there are Additive Manufacturing applications for validations prototypes, mockups, series production, supports for industrialization and spare parts. The company has been using additive technologies for about 30 years, it has got 77 machines of different technologies: FDM, MJF, POLYJET, SLA, and SLS. As well as the brands that are among the main suppliers of additive technology on the market: Stratasys, HP Jet, Formlabs, EOS, 3D System, etc. These machines produce approximately 50.000 parts per year, using the main materials on the market.

1.1.3 Valeo Santena

Valeo Santena is a small factory near Turin, it is part of the business group “Comfort and Driving Assistance Systems” section, in particular for a range of products that is identified as “Interior Switches and Control” (ISC). That stands for every human-machine interface found in the vehicle, buttons with mechanical or capacitive technology. This company has the most advanced techniques and tools for the design, development, and testing of the group’s products. The main customers of this plant are in the luxury sector: Ferrari, Maserati, Bentley, Aston Martin, Alpine, Rolls Royce, and McLaren.

Figure 1.2: Ferrari and Maserati's Steering wheels with respectively capacitive and mechanical buttons and switches*, by Ferrari, (2019), Maserati's (2013)*

This high-end reality goes well with Additive Manufacturing because needs small production volumes, from hundreds to thousands of parts per year, for small component dimensions. Furthermore, Valeo Santena is lucky enough to have internalized design; it can take care of the evolution of the product from 0 to 100, starting from the style skin, passing through the internal design, developing and testing of prototypes, and then the products deriving from a definitive process. Those projects need a very rapid and compressed development over time and numerous minor design changes. On the other hand, additive represents an attractive business case only in case of low production volumes. Moreover, AM allows great responsiveness to problems and to have an object from CAD to physical in less than twenty-four hours. It is a type of design that can be defined as revolutionary, although it has a limited printing size.

For the reasons seen, this company has started investing in research and in the effective application of the additive for serial production, with the focus on providing their customer with a different design and above all a customization that is increasingly requested *ad hoc* on the various products.

1.2 Additive Manufacturing

Additive Manufacturing (AM) encompasses methods of fabrication that build physical objects through the successive addition of material, directly from digital models. This technology differs from traditional mechanized and subtractive process techniques, which are based mainly in the removal of material by methods of abrasion or chipping, such as milling, cutting, turning and drilling, as O'Connor et alt. explain (2018). In AM is the design that determines the production, which is why we also speak of "design-driven manufacturing". Therefore, its production process has, as its starting point, the creation of a 3D model of the object to be produced, which is then converted, using specific software, into a file in STL format. Subsequently, dedicated software will allow the production of the machine file necessary for manufacturing, through the "slicing" of the 3D file, appropriately "oriented" and "supported". This process includes within it different technologies that exploit materials for different applications. From plastic to metal, the procedure is quite similar, in that a source (laser, electron beam, ultraviolet lights, etc.) is used to bind the layers generated by the "slicing" of the 3D file to be reproduced (Wohlers, T. and Campbell, R.I., 2017).

The nature of AM has been revolutionized with the advent of the 3D printing industry. In this operation, objects are specifically created by depositing layers of material. The CAD software tells the printer where and how much material to deposit. For the past several decades, 3D printing technologies have advanced rapidly and recently reached a state of mainstream adoption, particularly for rapid prototyping. They can quickly generate very complex geometries. There are many applications for Additive Manufacturing across many different industries. Whether used to generate small and medium series manufacturing or visual and functional prototypes. This approach offers compelling benefits that traditional approaches just cannot match. Agile product modification and functional integration can be completed more rapidly and more affordably, dramatically accelerating product development and market entrance (Wang, Y. et al., 2020). It is totally free from the shape to be produced, the deposition of the material layer by layer allows the creation of truly complex shapes and geometries. Another advantage of Additive Manufacturing is to be able to produce components in a single solution, that were previously produced separately, and then assembled or welded, significantly increasing the final performance of the object.

1.2.1 Advantages and Disadvantages

The advantages of AM can be divided into two class: product and process, (Quinlan et alt., 2017, Wohlers, T. and Campbell, R.I., 2017). About the product, it can give maximum freedom of design without the need to over-assemble, the possibility of making light structures, even integrating several pieces into a single component, and an ergonomic and customizable design. Instead, about the process, these technologies can generate unlimited shapes without tools, moulds, or clamping devices and with minimum operator intervention. The products are not assembled downstream and, at last, times and costs are related to the overall dimensions, they are almost independent of the geometric complexity. However, unlike traditional production technologies, it allows not waste production material by removing it.

Concerning the disadvantages of Additive Manufacturing's product, the quality of the surface finish is inferior to traditional manufacturing, and there are a limited and expensive number of materials. The process has limited working volumes and limited construction speeds, each machine processes contained materials. Lastly, there are no automation systems, which means that one operator is needed for the loading-unloading phases.

1.2.2 Classification of AM techniques according to the starting material

Chronologically, liquids are the first material to be used, through **photopolymerization**, as classified by Wang, Y. et al. (2020). This involves the hardening of a resin under the effect of ultraviolet, used by dentists for fillings. There are two types of applications, through a laser or through a lamp. The first one is called *Stereolithography (SLA)*. It is based on a work platform immersed in or emerged from a light-cured resin bath. The ultraviolet light laser activates the polymerization of the liquid photopolymer, solidifying it. Subsequently, the base moves downwards so that the laser exerts its action again (Wohlers, T. and Campbell, R.I., 2017). With this method, figures with great detail are obtained, even if a certain amount of material is wasted depending on the pieces due to the support material that is subsequently eliminated. Therefore, SLA offers high-resolution printing, clear part details, compatibility for painting, plating, and finishing, as well as a range of premium materials for a variety of tasks, making it especially well-suited for prototyping.

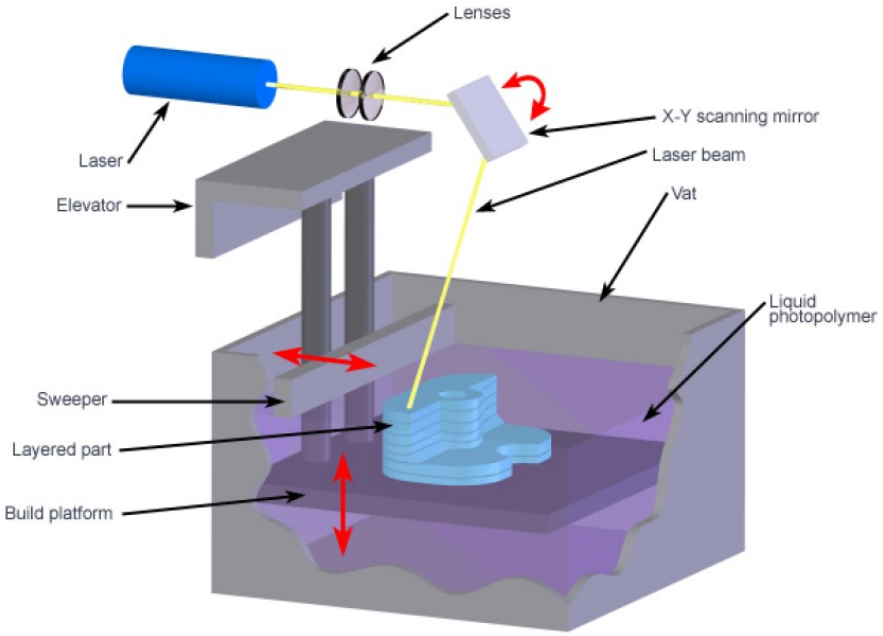

Figure 1.3: Schematic representation of SLA technology*, by CustomPartNet (2008)*

The second method hardens the photopolymer through a UV lamp, it can be *PolyJet/Project* or *Direct Light Processing*. The first one is a powerful layer-by-layer Additive Manufacturing method. The deposition takes place with a multi-nozzle head since the piece and the support are made up of two different liquid photopolymers. The latter is soluble in water, so there are fewer problems in the removal phase. In the upper part, it has a UV lamp that immediately hardens the material deposited by the head (Wohlers, T. and Campbell, R.I., 2017). The accumulation of these thin layers in the build tray creates a highly accurate 3D model. Liquids can also be used in **jet printing**, a head injects the construction material, it is called *Drop on Demand*.

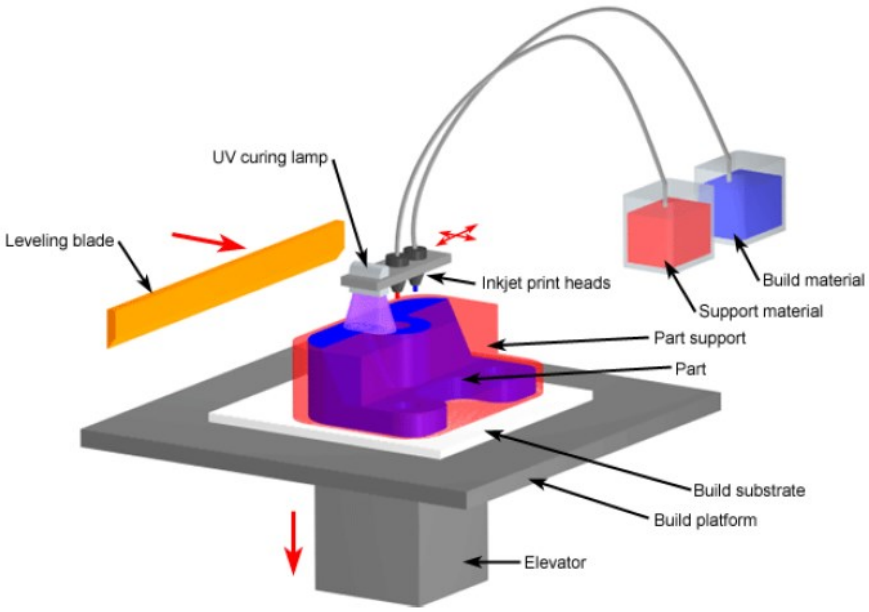

Figure 1.4: Schematic representation of PolyJet technology*, by CustomPartNet (2008)*

Solids can use **extrusion**, for example with *Fused Deposition Modeling (FDM)*, from which all low-cost printers derive, it makes polymers and, in particular ways, metals. Thermoplastic filaments are extruded by a nozzle and deposited on a work platform that moves along the Z-axis, while the head along the X/Y plane. The impression starts from the bottom layer, creating a surface on a support material, whose properties are more fragile, to be able to separate the piece. The thermoplastic solid material is in the form of wires, brought to fusion and subsequently solidified, in a highly controlled and automated manner (Wohlers, T. and Campbell, R.I., 2017).

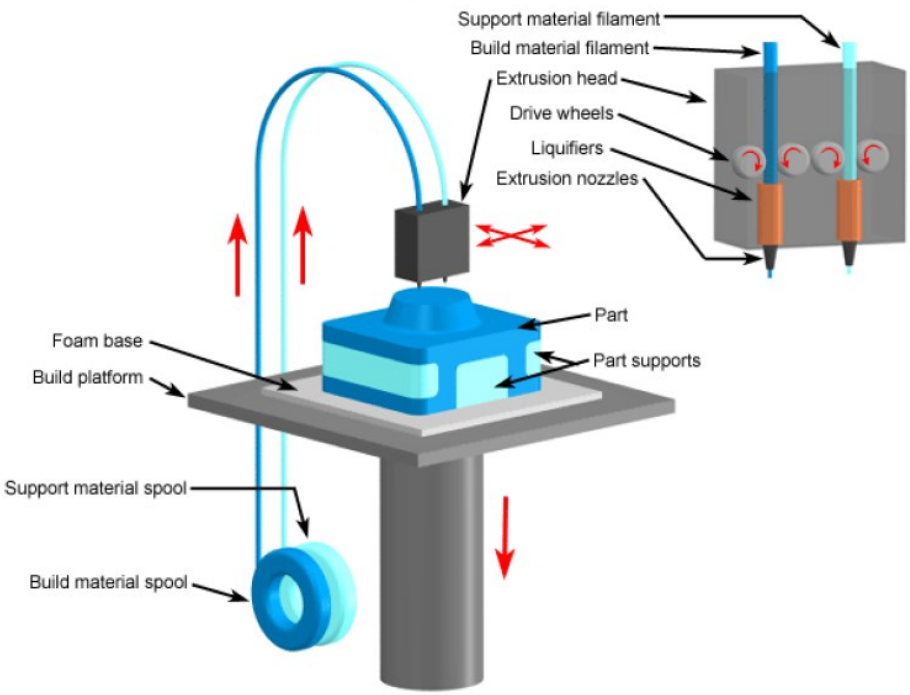

Figure 1.5: Schematic representation of FDM technique*, by CustomPartNet (2008)*

With the powder, the Additive Manufacturing techniques can use only **one component** with one energy source. *Selective Laser Sintering (SLS)* refers to fusion with a laser source of polymeric material particles; this printer works layer by layer. As Wang, Y. et al. (2020) explain in their paper, at the top, there is the fixed laser source which is focused by mirrors and a lens called $ff{-}\theta\theta$. This structure is able to move the laser beam and make it always perpendicular to the surface avoiding divergence phenomena in the machine work plane. In the lower part, there is an elevator that deposits the first layer of powder, the laser radiation selectively melts the powder particles to create the section. Once the material has been consolidated, the second layer of powder is applied with the aid of the piston system, and so on until the complete realization of the piece. The laser power is adjusted in such a way as to melt and make the layers adhere to each other, so the previous layer must be partially re-melted. All the powder material that is not sintered is still where it was initially and serves as a support for the pieces. Once the job is done, that material can be removed and reused for printing future pieces (Singh, A.P. and Pervaiz, S., 2021).

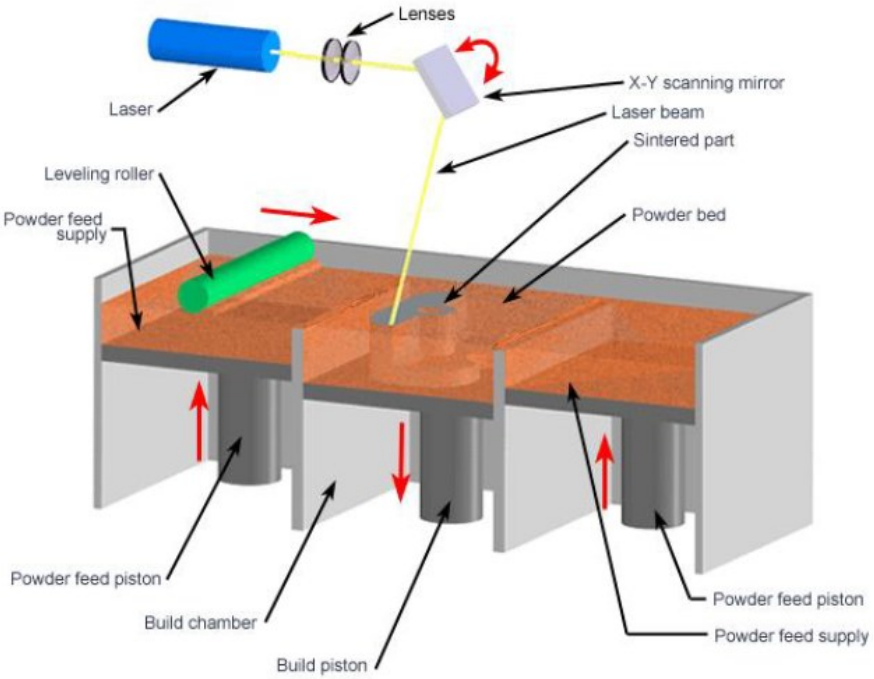

Figure 1.6: Schematic representation of SLS technique*, by CustomPartNet (2008)*

Selective Laser Melting (SLM) is identical to SLS but metal powders are used. *Electron Beam Melting (EBM)* is the fusion of powder with an electron beam source, the characteristics change even if the concept is the same, only metals are made. Instead, *Laser Deposition* uses metals with a laser source. The variant of this type of technology uses **one component with** the addition of a **binding agent**. *3 Dimensional Printing* is part of this group, it is formed by a print head that deposits the glue on the powder bed. Lastly, there is the *HP Multi Jet Fusion (MJF)* printing process. It's a recent AM technology, that allows reduced construction times, without compromising the strength and quality of the print (Wang, Y. et al., 2020, HP Inc., 2020). It is a powder bed fusion 3D printing system, with no support involved. MJF produces unique parts with high resolution and mechanical strength, a smoother surface, in a short time and at a lower cost, compared to any other 3D printing method. This technology has been designed to selectively distribute across the entire bed two types of inks, called Detail Agent and Fusing Agent. These define and melt together the sections of the printed object, using infrared light (IR). Readers will be able to learn more about how it works in the next chapter.

1.3 Multi Jet Fusion

The American multinational information technology company, HP Inc., entered the Additive Manufacturing scene in 2016 with the launch of its 4200 series Multi Jet Fusion (MJF) polymer 3D printing platform. It's a revolutionary technology, which produces economic, quality and functional parts with best-in-class isotropy thanks to a multi-agent printing process. Furthermore, it has a speed production that is up to 10 times faster than today's competing products, due to the area-level processing of the technology (HP Inc., 2022). In fact, it processes parts in two quick passes throughout the area, this leads to the same amount of time being spent on each layer, regardless of how many sections need to be printed. So, the MJF time process depend on the Z direction of the JOB, if the products are developed along this axis, the time will increase. It also has more performing hardware, it's easier to use, cleaner and more precise. In the same work area, the MJF can produce identical pieces or different from each other, from 100 to 1000, depending on the size (Singh, A.P. and Pervaiz, S., 2021). It gave the greatest opportunity for plastic material manufacturers, to develop and innovate their own materials and supply them for this technology, giving competition on prices and performance.

1.3.1 The machine

As the HP brochures and Website (HP Inc., 2020, 2022) describe, the HP Jet Fusion 3D printing solution consists of three different units: the Printer, the Build Unit and the accompanying Processing Station, used for powder handling. The Build Unit is a mobile unit, formed by the work area, called JOB, a chamber with dimensions 380x284x380 mm and two lateral storage tanks for the fresh material used during the printing process. The Printer consists of a carriage with print heads depositing two different inks, called Fusing Agent and Detailing Agent. The Fusing Agent has a high carbon black content and thus has a higher tendency for light absorption. The second agent is applied to modify fusing and create fine detail and smooth surfaces; it consists mainly of water, which lowers the temperature of the heated surface and part contour locally, due to evaporation energy being removed. Scherer et al. (2020), in their work, identified the ingredients of the agents in real samples of printed parts. Therefore, on each layer, the machine draws the section of the part in detail, with the Fusing Agent inside and the Detail Agent on the perimeter. In the Printer there are also two types of IR lamps: the Heating Lamp and the Fusing Lamp. The Heating Lamp keeps the chamber Temperature constant at 175 °C, close to the powder melting temperature which is around 185 °C, but not yet enough to trigger the transition. The Fusing Lamp, on the other hand, passing after the agents have been applied, gives sufficient energy to the areas where the Fusing Agent has been deposited, absorbing more energy, they melt. Printing takes a maximum of 15 hours, the same time as the cooling in the Processing Station if the setting is "fast cooling". This unit features cooling, material discharge and mixing capabilities via a semi-automatic process that reduces labour costs. To be more precise, the Processing Station is able to read the chamber contents information, the temperature, measured by an insertion thermometer, and how long has it been since the print was completed, and indicates the cooling options available. Is possible to use "natural cooling" or intermediate methods, leaving the build unit in the machine for long enough to cool naturally, or "quick cooling" by connecting the laminar airflow suction mechanism, which pulls air through the build car (Mele, M. et al., 2020). This mechanism is used also to remove unfused powder and unpack the printed parts.

1.3.2 The process

Before submitting everything to print, HP software makes it simple to prepare the items to be printed, by reviewing the files for flaws and automatically aligning the 3D models within the work volume. For material loading, the Build Unit is inserted into the HP Jet Fusion 3D Processing Station. Pre-packed HP material cartridges are installed and quantity and mix options are selected. Once the material has been transferred, the Build Unit is inserted into the Printer, in order to start production. The material is lifted from inside the Build Unit and a layer, which thickness reaches 80 μm, is spread evenly on the printing surface through a roller. The heads place the two agents and the Fusing Lamp selectively melts the material, only where the Fusion Agent has been deposited. Once the fusion has taken place, the platform is lowered by a further 80 μm, the roller restores another layer of PA12 powder and the process is repeated, until the conclusion of the JOB project. The fusing process requires accurate temperature control across the entire material layer to determine which areas receive more energy to raise the temperature and which areas are cooled, allowing for control of thermal bleed and layer-to-layer fusing and cooling (Singh, A.P. and Pervaiz, S., 2021). The result is the control over mechanical properties, dimensional accuracy and repeatability. At this point the Build Unit is removed from the printer and brought to the Processing Station, giving the possibility to insert a second Build Unit, in order to continue with production. Once the powder core temperature is below 50 °C, the parts are ready for cleaning. All excess powder on the parts was first removed by hand, through a vacuum system and a brush, followed by powder removal by glass-bead blasting with a pressure of three bars, before proceeding with any final finishes. As is shown in Alomarah, A. et al.'s microscope images (2019) of the printed materials before the blasting treatment: non-fused powder with 40-100 μm particles still adheres to the fused powder. It is well known that adherence of unmelted or partially melted particles to the part in other additive manufacturing methods, such as Selective Laser Melting (SLM), results in dimensional deterioration and porosity that affect the density of the printed parts.

The unused powder is recycled, usually 80%, and mixed with new material, 20%. An MJF system-provided processing station handles the various powder mixing ratios. The processing facility vacuum-cleans both recycled and virgin material from system-integrated waste powder reservoirs. A mixing device, which is a component of the processing station, enables the assumption that the old and new powders are mixed uniformly.

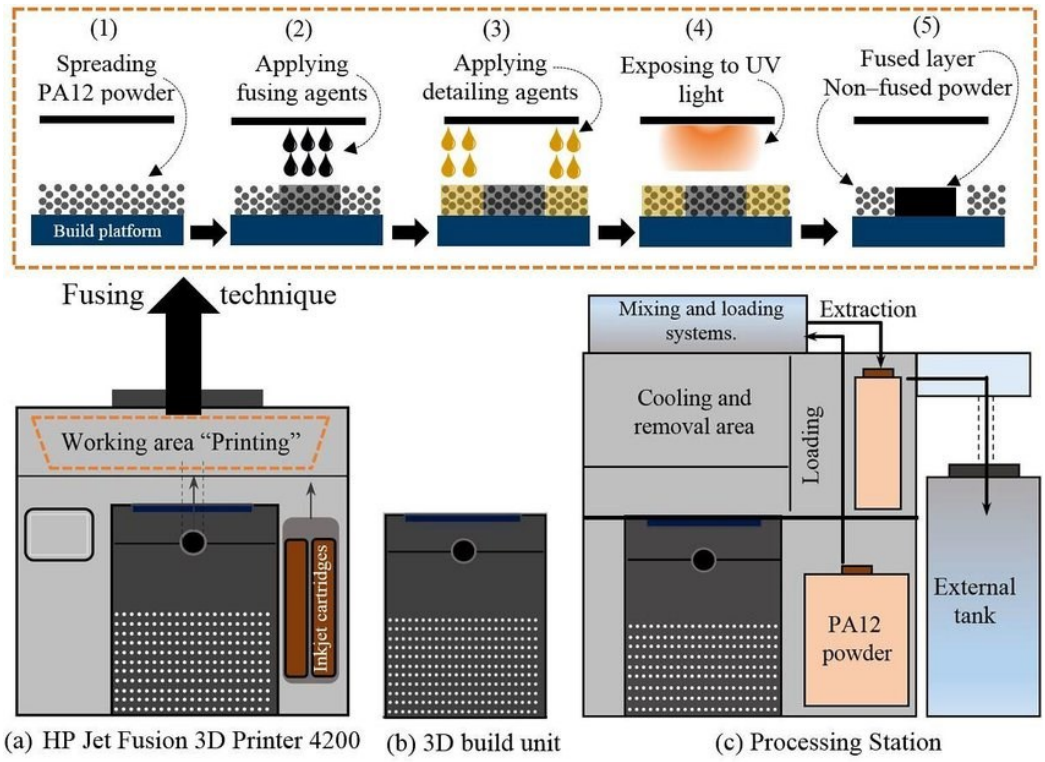

Figure 1.7: Schematic representation of Multi Jet Fusion (MJF) process: (a) HP 3D 4200 printer; (b) 3D build unit; (c) processing station, *by Alomarah, A. et al. (2019)*

Checks before and during printing allow reliable, high-quality products with excellent dimensional accuracy and optimal mechanical properties in a shorter time. In fact, it is possible to examine each part's individual voxels using the multi-agent printing technique. Equivalent to a pixel with volume, a voxel represents a value on a regular grid in three dimensions (Alomarah, A. et al., 2019). By controlling the processes of each individual voxel through agents, HP Multi Jet Fusion can produce parts that can't be made by other methods. The printer has 4 different printing modes including fast, balance, cosmetic and mechanical. The mode changes the print time and performance mechanics of the printed parts (HP Inc., 2022).

A distinguishing feature of the Multi Jet Fusion process is the capillarity effect, which influences the top planar surfaces of printed items (Mele, M. et al., 2021). This flaw, which happens during component manufacture, is caused by the interaction of the surrounding powder that has been impregnated with Detail Agent and the molten polymer. The liquid meniscus expands due to the difference in surface energy between the liquid substance and the wet powder. Surfactants, that are a part of the Detail Agent's chemical makeup, lessen this action. In the case of curved edges, the Mele, M. et al. paper suggests an analytical model for the prediction of the capillarity effect (2021).

1.4 Polyamide 12

Nylon 12 is a long-chain carbon polymer, $[(CH_2)_{11}C(O)NH]_n$, more precisely, a linear semi-crystalline-crystalline thermoplastic. It is composed of ω-aminolauric acid, a bifunctional monomer with one amine and one carboxylic acid group, or laurolactamic monomers. Each of these has 12 carbon atoms, hence the name "Nylon 12" (Umeda R.E. et al., 2022). Nylons are also called polyamides, due to the characteristic amide group present in the principal chain. These amide groups are very polar and can bind to each other with hydrogen bonds. For this

reason, and thanks to the fact that the main chain of nylon is regular and symmetrical, nylons are often crystalline, and they form very good fibers (Rahim T. N. A. T. et al., 2017).

Nylon 12 can be produced either by polycondensation of ω-aminolauric acid or by ring-opening polymerization of laurolactam. The second one is the preferred way for commercial production, as it results in a more stable product; readers can explore its reaction steps in Umeda and his team's article (Umeda R.E. et al., 2022).

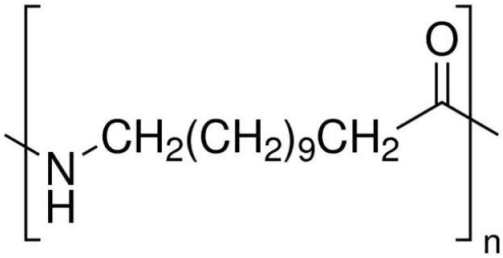

Figure 1.8: Polyamide 12 formula

The typical application areas for PA12 are the automotive, photovoltaic (PV), construction of gas and oil pipelines, electrical and electronics, leisure and sports sectors.

1.4.1 Polymers properties

To better understand the characteristics of this polymer it is necessary to introduce some fundamental concepts. The books "Corrosion Engineering " by Fontana, M.G. (2005) and "Food Packaging Materiali, Tecnologie e qualità degli alimenti" by Piergiovanni, L. and Limbo, S. (2010), come to our aid. Polymers are macromolecules, organic substances formed by a set of large molecules with a high molecular weight. These interact with each other through secondary bonds. Each of these macromolecules is in turn formed by the repetition of *n* small structural units linked together with covalent bonds: these units are called monomers. The number *n* of average repeating units is also called the degree of polymerization. It is important because highlights the distinction between oligomers (n <10) and polymers (n> 10).

In the field of polymers, there are two different types of chemical reactions: polyaddition and polycondensation. In the PA12 production process, these two reactions occur simultaneously after the opening of the acid ring (ROR). Polycondensation is the kind of polymerization in which the monomers are joined by reactive end groups, with the dissociation of volatile secondary products (water, ammonia). A part of the monomer molecule is eliminated when the monomer becomes part of the polymer, some atoms of the monomer do not end up in the polymer. It is a slow-step mechanism, as the reaction is difficult, for the formation of the polymer there must be an effective collision between favourably oriented monomers. Otherwise, in polyaddition, the monomer molecule with double bonds becomes part of the polymer.

Another way to classify them is through the solid state, it is possible to distinguish amorphous polymers from crystalline polymers. A crystalline polymer is distinguished by organized, regular-shaped structures that combine to form lamellae, which are thin plates with a thickness between 10-20 nm and a length of 10 μm. These provide high thermal and mechanical resistance, thanks to strong inter- and intra-molecular bonds. Such lamellae (up to 60-80 repetitive units) fold due to strong intermolecular bonds, the strength of which depends precisely on the number of folded chains. There are no 100% crystalline polymers, except for a few rare examples produced in the laboratory. So, we always talk about semi-crystalline polymers, characterized by a certain degree of crystallinity. Having a certain degree of crystallinity implies the presence of crystalline domains dispersed in an amorphous matrix. There are three types of crystalline morphologies:

- Lamellar crystals, obtained by precipitation in a solvent, subsequently evaporated;
- Spherulite crystals, a melt polymer solidifies by cooling. They have a central nucleus or germ from which helical chains made of lamellae start. The sipes grow like the spokes of a bicycle wheel from a central core. They expand in three directions, resembling a sphere which is called a spherulite. The single-folded chain lamellar crystals are separated by amorphous material and the individual lamellae are held together by connecting molecules. There are billions of spherulites in a crystal sample. They are 3D spheres, the amorphous state is present both inside and outside the spherulite. This is the PA12 case (Aharoni, S.M., 1997, Riedelbauch, J. et al., 2019);

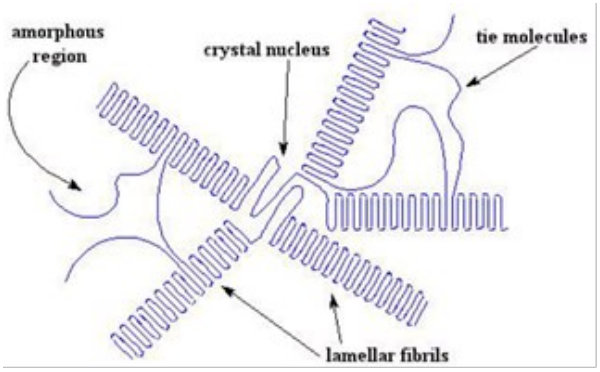

Figure 1.9: A crystalline polymer spherulite and its parts, *by Aharoni, S.M. (1997)*

- Fibrous-lamellar crystals are obtained by solidification of the polymer under flow conditions. The melt is sent to an extruder, cooling it. The nucleation centres become lines and the fibrous-lamellar crystal is formed. These lines allow to have proprietary anisotropy: along a certain direction, it brings to higher mechanical resistance.

The degree of crystallinity of the polymers is strongly influenced by the cooling rate. Lastly, for this study is important to understand the effect of crystallinity on polymers. A polymer with a higher degree of crystallinity, or rather, with ordered polymer chains, will have more packing. It will be stiffer, and denser and will resist dissolving and swelling more. Water will have a harder time passing between polymer chains, so the object will more easily retain its shape. It will have higher intermolecular forces, higher softening points, higher tensile strength, and higher stiffness and density.

Semi-crystalline polymers are characterized by the crystallization or melting temperature T_m and by the glass transition temperature T_g (Aharoni, S.M., 1997) The melting process is the inverse process of crystallization, which occurs due to the heating of the polymer. It corresponds to the transformation of a solid material, having an ordered molecular chain structure, into a viscous liquid with a strongly disordered structure, therefore a real phase change takes place. This change in the structure of polymers develops over a range of temperatures and depends on the previous history of that polymer. Furthermore, T_m increases with the thickness of the lamellae and as the heating rate increases, decreases in the presence of impurities and imperfections in the polymer. In correspondence with the T_g, it doesn't have a phase change, but this indicates the passage of the plastic material from the amorphous glassy solid state, in other words, a stiffness behavior to the rubbery one. It manifests itself in the amorphous, non-crystalline part. Another definition of the glass transition temperature is the temperature at which the free volume reaches the constant critical value; this value is indicatively the same for all polymers and is approximately equal to 2,5% of the total volume. The passage through the glass transition is accompanied by sudden changes in some physical properties such as stiffness, heat capacity and coefficient of thermal expansion. More in

detail, it can be said that for $T < T_g$ the polymer is rigid, brittle and transparent like glass. Rigid plastics, such as polystyrene and polymethyl methacrylate, are used in ambient conditions below their transition temperatures. As their T_g's are above room temperature, both around 100 °C. On the contrary, for $T > T_g$, movements of molecular segments become possible, the molecules assume a curled configuration. By application of a force, they can unwind and assume an extended configuration. Rubber elastomers such as polyisoprene and flexible plastics, such as polyethylene and polypropylene, are used above their T_g, which is in the rubbery state when they are soft and flexible.

Polymers are divided into elastomers and plastomers, of which thermoplastics and thermosets are part of the latter, classified based on their behavior with increasing temperature.

1.4.2 Thermoplastics

Thermoplastics are formed by chains of C atoms arranged linearly with respect to each other, as the readers can find in the books mentioned (Fontana, M.G., 2005, Piergiovanni, L. and Limbo, S., 2010). In fact, the molecules are linearly polymerized with few and random transverse bonds and react to an increase in temperature with a reciprocal slip. They are recyclable by re-melting and giving them another shape, so they can be reused. They soften with heat and solidify by cooling in a reversible way, without altering the structure. They are processed by melding, at lower temperatures than other polymers, with extremely high production rates.

Regarding the mechanical properties of thermoplastic polymers, it is known that they have low elastic modulus (0,1-20 GPa) directly proportional to the degree of crystallinity, and secondary bonds are involved (Aharoni, S.M., 1997). Tensile strength lower than 80 MPa and a noticeable creep even at room temperature. Elastic modulus, tensile strength and brittleness generally increase with the percentage of crystallinity.

1.4.2 Polyamide 12 properties

Polyamide 12 characteristics are between those of short-chain aliphatic nylons, such as PA 6 and PA 66, and those of polyolefins. Its low water absorption and density, 1,01 g/mL, result from its relatively long hydrocarbon chain length, which also gives it dimensional stability and a nearly paraffin-like structure (Aharoni, S.M., 1997). The properties of Nylon 12 include the lowest water absorption properties of all polyamides, meaning that any PA 12 part should remain stable in humid environments. It is a good electrical insulator and, like other polyamides, it does not affect the insulation from moisture, furthermore, it has a good level of resilience and resistance to many chemicals.

The main characteristics of PA12 powder found in the literature (Rosso, S. et al., 2020, Salmoria, G.V. et al., 2009, Riedelbauch, J. et al., 2019) are:

Standard density = 1,01 g/cm^3
Melting temperature T_m = 185-187 °C
Glass transition temperature T_g = 37-55 °C
Crystallinity = 48,3 ± 0,4%

1.4.3 Polyamide 12 in MJF

As Alomarah, A. et al.'s research (2019) presents, regular deposition of the fused powder in the case of MJF is known to lessen orthotropic. This is the characteristic of a material that exhibits distinct and independent mechanical or thermal properties in the three mutually

perpendicular directions. Such unwanted property is characteristic of materials or structures produced by some 3D printing technology, like Fused Deposition Modeling (FDM).

Mele, M. et al. (2020) and Riedelbauch, J. et al. (2019) are two of the few in literature, to demonstrate two separate melting peaks for PA12 components, which are comparable to SLS. These two peaks correspond to the two phases of the PA12 powder: the melted exterior and the unmelted interior. Single melting peak temperatures may indicate effective melting in the area where the DSC samples are taken, either as a result of the Fusing Agent's action or higher temperatures.

According to Rosso, S. et al.'s analysis (2020), the crystallinity reduced during the printing process from $48{,}3 \pm 0{,}4\%$ in PA12 powder to $31{,}5 \pm 0{,}3$ %. Also the melting peak is translated to lower temperatures in the printed samples ($182{,}7 \pm 0{,}4$ °C), resulting in a broadening of the melting peak. The authors cited, also demonstrated no discernible changes between SLS and MJF's microstructure. That means that Salmoria, G.V. et al.'s study (2009) can also be applied to PA12 in this innovative technology. Their XRD analysis showed in the starting powders two crystalline forms, the monoclinic or triclinic α-phase and the pseudohexagonal γ-phase. While mostly γ-phase and a little α-phase shoulder can be seen after printing. Ellis and his colleagues also saw similar crystallinity between SLS and MJF, as the results show a decrease in this as the print density increases, and a linear increase of the degree of particle melting (Ellis, A., et al., 2014). They examined the quantity of carbon black ("Radiation Absorbing Material") deposited on the surface, which is correlated to the print density; therefore, the part's microstructure is not significantly affected by the radiation-absorbing substance, the Fusing Agent.

The cooling time is a key factor in determining the crystallinity of items using MJF, as shown by melting enthalpies reported by Mele, M. et al. (2020). Fast cooling techniques make distortions worse because layers along the Z-axis shrink at different rates. With regard to natural and intermediate cooling, this effect is negligible. This finding implies that the choice of cooling technique can shorten cycle times without significantly affecting the geometric precision of the components or affecting the operation of the parts. Since sections' tensile characteristics, which are unaffected by density, follow the trend of crystallinity. Mechanical resistance has risen with the higher crystallinity degree reached during progressive cooling.

As the readers have learned in the sub-chapter 1.3.2, MJF's printed items need glass-bead blasting to remove the loosely bonded, unfused PA12 particles that were stuck to the coupon surface prior. This technique leads to a rough and granular morphology with R_a between 2-11 μm, in O'Connor, H.J. et al.'s study (2018). Their results revealed roughness values for the top surface to be higher than the bottom. This was confirmed by the explanation that a superior sintering process caused greater diffusion of polymers to fill gaps at the bottom of the component. Quite the opposite, the study of Rosso, S. et al. (2020), revealed greater roughness at the bottom than the top because they did not use any post-processing methods advised before the experiment, so the powder that was only partially melted stuck to the part's bottom face and changed the texture of the surface. Furthermore, a porosity of 3-5 % was achieved with MJF, which is 5% smaller than the porosity of printed items produced by selective laser sintering (SLS)

Morales-Planas, S. et al. (2018) conducted studies on the high-pressure water tightness of samples made using MJF, demonstrating that this technique may be utilized to make fluid-handling parts because there is no open porosity in their structure.

The results of Riedelbauch, J. et al. (2019) study indicate that, in terms of mechanical properties, combining aged powder with virgin material is not required for at least five processing cycles. Additionally, no effect on mechanical qualities was found in the investigation of various mixing ratios. In terms of practical applications, this means that component manufacture is sufficient to replace the material that was removed from the

powder cycle. The findings of this investigation may be significantly impacted by increased thermal stresses caused by greater packing densities and larger build areas.

2. Study definition

As previously explained the goal of this thesis is to broaden knowledge on the compliance and applicability of Polyamide 12 (PA12) components, produced through Multi Jet Fusion technology (MJF), in the automotive world. It does this by analysing the variation in these specimens' chemical, thermal and mechanical properties in relation to their position in the printing work area, orientation, and aging. The research was defined and developed with the collaboration of three entities: Valeo Santena, Polytechnic of Turin and Valeo Martos. Each of these had a specific task to achieve this goal. Valeo Santena was the head of the operation, it took care of the study definition, the creation of the STL file of the printing area 3D model, the communication and the work management. Furthermore, they provided the instrumentation for dimensional and visual characterization, in addition, for accelerated aging, they supplied the climatic chambers used for the validation of their products. Valeo Martos, located in Spain, took charge of the production and shipment of the specimens requested by Valeo Santena. This branch is part of the "Visibility Systems" business group and has a department dedicated to rapid prototyping, in this area the MJF of interest for the study is located and used. Finally, the collaboration with the Polytechnic of Turin has allowed the deepening of the study, thanks to the lecturers' diversified knowledge, and the adequate characterization of the specimens, thanks to the mechanical, chemical and thermal equipment that the departments own.

In this chapter the readers can find the criteria with which the thesis is developed, it is divided by the variables, called scenarios, analysed: position in the printing area (α), orientation perpendicular or parallel to the flat surface (β) and aging stage (γ), with the corresponding description. In addition, in this second chapter, it is also possible to obtain technical information on the printing phase: printing machine settings, the material used, and the size and quantity of printed specimens. In the corresponding sub-chapter, the dimensional characterization of the printed samples to obtain the capability is found, or rather, to obtain the repeatability and accuracy of the process.

2.1 Scenario α) Dependence of the samples position inside the printed JOB;

The first scenario is the dependence on the characteristics of the specimens on the position within the working area. The JOB of the "HP MJF 4200 Series 3D Printing Solution" is a rectangular parallelepiped of dimensions 380(b)x284(b)x380(h) mm. Ideally, 9 points must be analysed in order to fully describe the working area, look Figure 2.1.

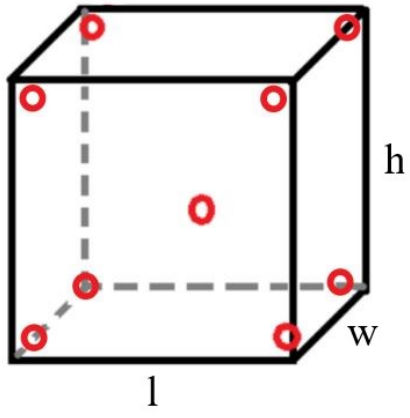

Figure 2.1: 9 points distribution into the JOB

This study assumes the specimen's characteristics as symmetrical in the printing area, in order to reduce the number of samples to be produced by Valeo Martos. Therefore, three points considered cruxes are evaluated, as shown in Figure 2.2:
A → corned at the bottom of the JOB;
B → in the middle of the JOB;
C → diagonally opposite corner than point A, at the top of the JOB.

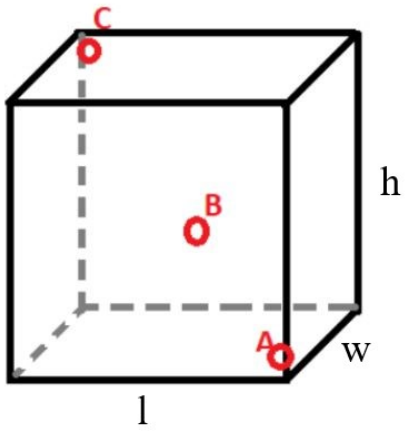

Figure 2.2: 3 points distribution into the JOB

For this scenario, due to the assumption done, the research examines the difference between three areas in which the heat losses are different: first layers (A), middle layers (B), last layers (C).

2.2 Scenario β) Influence of the samples orientation inside the printed JOB (XY or Z);

For this case of study, in which are evaluated the properties of the samples depend on the printing orientation (XY or Z planes), the thesis analyses this scenario in point A. It's a critical point for the orientation because the first layers are in contact with the flat surface, which dissipates heat with the environment even during the moulding of the other sections above it, this leads to uneven cooling temperatures. Furthermore, these samples have the weight of all the powder and the items above them. So this area is the best to see, if there are any mechanical and thermal differences in orientation.

2.3 Scenario γ) Effect of the aging over printed samples for 3-time steps (no aged, ⅓ aged, fully aged);

Being necessary to extend the materials library with information about PA12 components' stability over the years and wanting to monitor it on the parts followed by Valeo Santena product line, section 5.3.7 of the FCA Standard CS.00056 specification was followed (FCA US - Quality & Reliability Engineering - 5200 and FCA ITALY - Electrical/Electronics - Electronic Architecture, Talevski, M. and Molina, A., 2015).

This section, dedicated to the High Temperature & High Humidity Endurance test (HTHE), describes all the necessary information and the procedures to follow. This test is done to mimic the conditions and mechanisms of failure that could occur when electronic parts and devices are used in a vehicle and subjected to high temperatures and humidity. These failures include electrical shorts brought on by metals' oxidation, galvanic corrosion, and/or material absorption of water. In turn, materials may swell and become weaker as a

result of water absorption, which may cause failures in adhesive, potting, seal, and conformal coating compounds. All electronic parts must successfully complete the HTHE test. For all applications for interior cabin or trunk locations that are not PT-Emission/ Passive Safety applications or exterior packaging locations, the test duration is 700 Hours.

Test parameters:
a) Temperature → 85 °C + 4 °C (No negative tolerance);
b) Relative Humidity → 85% + 4% (No negative tolerance).

Test Procedure:
A. Set up the component in a controlled test chamber at 85 °C;
B. Add humidity to the chamber and keep the internal relative humidity at 85% RH;
C. Calculate the test duration when the temperature and relative humidity are 85 °C and 85%, respectively;
D. Test the component's functionality every 47 hours or as required by the Component Specific Performance Standard.

The thesis characterizes this scenario in point B, in the middle of the working area, because it's the less critical one. This point is the most convenient for filling in the design phase and printing. Moreover, it implies homogeneous cooling temperatures, therefore the variation of characteristics with aging can be better differentiated. Then, for this scenario, it is assumed that the aging does not depend on the point of the JOB where the specimens are printed. Furthermore, this research monitors the specimens' properties in an intermediate state after about 240 hours, that is ⅓ of the vehicle's life, to evaluate the aging trend. The typical service life target refers to the 95th percentile of customer usage over the period of 10 years, which means 150.000 miles, or 15 years, depending on the device application, as the *"Environmental specification for electrical/electronic (E/E) components"* explained.

The test was performed in a climatic chamber located in the Valeo Santena laboratory which can be seen in Figure 2.3: Climatic chamber Heraeus/Vötsch VCV 7057-5/S.

Figure 2.3: Climatic chamber in Valeo Santena and test setup

2.4 Samples definition

The number of specimens necessary to carry out this study also depends on the tests to be performed to characterize them. The following list of tests was defined with the Polytechnic of Turin: to investigate the variations in the chemical bonds, the functional groups were examined through the means of infrared spectrophotometry in attenuated total reflectance (FTIR-ATR). Differential scanning calorimetry (DSC) was used to analyse the variation of thermal properties. To investigate the mechanical properties, such as the evolution of Young modulus (E), elongation at break, yield and ultimate tensile strength, tensile testing was used. For the maximum load and stroke at break, the three-point bending flexural test was performed. To determine the notch toughness of the material, the Izod impact strength test is also carried out, designing the indenter and the base with the annexed vise, not being present in the mechanical department. Lastly, the hardness with a Shore durometer type D and the Microindentation hardness testing with the Vickers indenter.

For the tests to be reliable, the measurements must be carried out with repeatability. Therefore, several specimens must be tested while maintaining the same measurement method, the measurements must be carried out with the same measuring instrument, in the same place, with the same conditions of use of the instrument and the measurand, in a short period and must be conducted by the same operator. Therefore, to have this degree of agreement between the series of measurements of the same measurand, it was decided to print 5 specimens for each invasive test to be performed. Tests that lead to deformation or breakage of the specimen are considered invasive: three-point bending flexural test, tensile testing and Izod impact strength test. For differential scanning calorimetry (DSC), where splinters of the product are necessary, only three specimens were required. The remaining non-invasive tests, such as FTIR-ATR and hardness analysis, can be conducted on the specimens tested in the unstressed areas or on the specimens before testing. Thus, the total number of specimens needed for the repeatability of the tests is 18. These specimens should have different sizes based on the test being conducted. Following the American Society for Testing and Materials International, each of its standards indicates the necessary dimensions. For the Izod impact strength test and for the three-point bending flexural test, the specimens must be rectangular in shape and 80 mm long, 10 mm high and 4 mm thick, as seen in Figure 2.4 (American Society for Testing and Materials International, 2010, 2017). To simplify the project, the same dimensions are also used for the three specimens, which splinters are used for the DSC test. This type of specimen is called "R". For tensile testing instead, the dimensions of the bone specimen for “Rigid and Semirigid Plastics” (American Society for Testing and Materials International, 2014) can be obtained from the corresponding standard. Therefore, the test specimen, for our case of study is Type I with a thickness of 7 mm and the other dimensions reported in Figure 2.5. This type of specimen is called "S". Both types were designed using Solidworks drawing software.

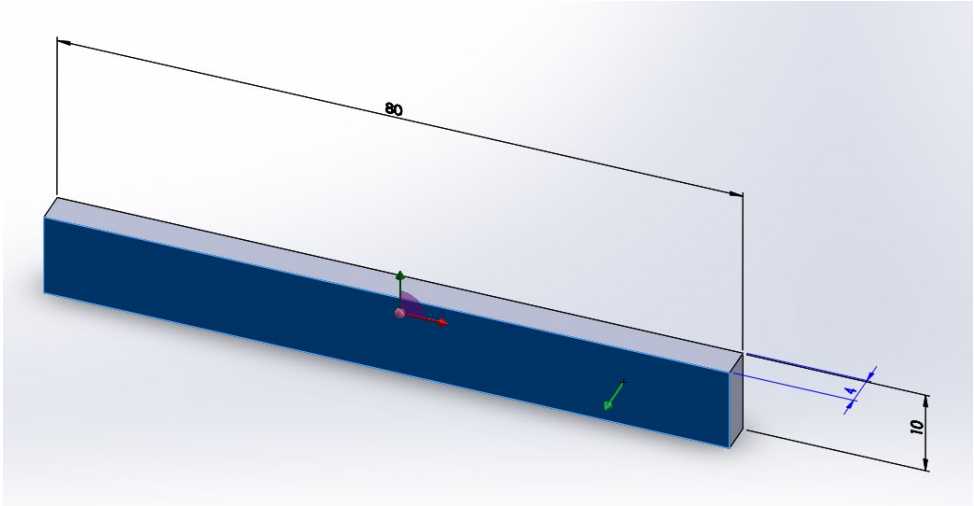

Figure 2.4: Specimen type R

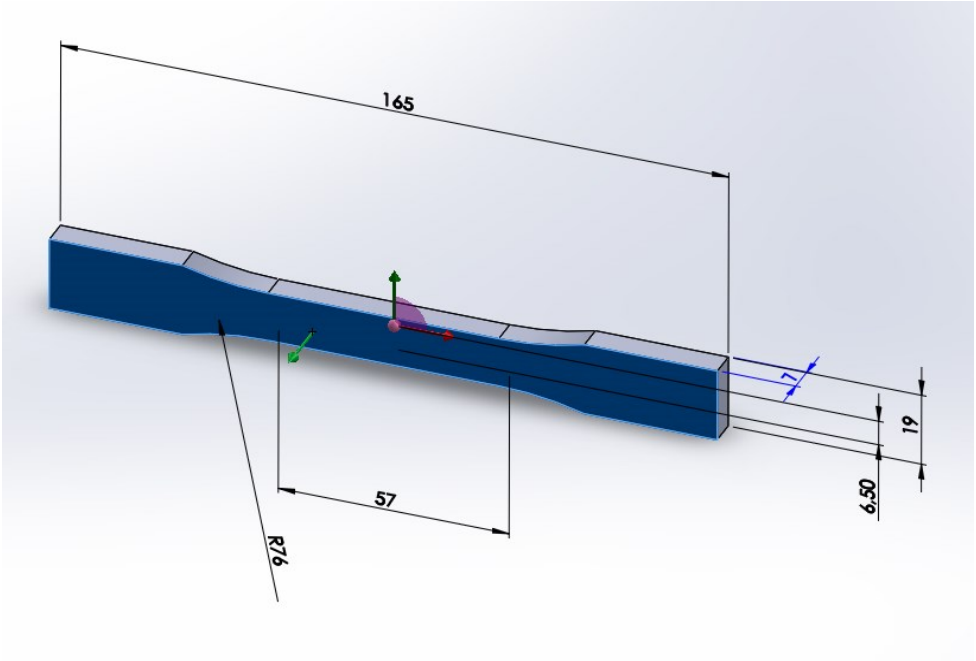

Figure 2.5: Specimen type S

Considering samples for preliminary tests, for example, to set up the equipment, or as master samples and to optimize the available space, 16 rectangular R-type samples are printed. In fact, two of exemplar R cover in length one of model S. Leaving the number of specimens that must be tested with tensile testing unchanged at 5, we have a total of 21 specimens.

Furthermore, the tests introduced are carried out for each type of case of study, whose variability is to be examined. This means that the block of 21 specimens must be printed, for scenario α, in the three positions A, B, and C, listed in sub-chapter 2.1. These are printed in a parallel direction to the support plane of the XY powder. For the β scenario, at point A, 21 specimens are also moulded in the Z direction. While, for the γ scenario, two other blocks are printed at point B, which have to face accelerated ageing, respectively, at 1/3 of the time or at all the 700 hours. These two blocks, for comparison, are also printed in the XY direction.

In total, therefore, as can be seen in Table 2.1, the total number of specimens needed to perform the study and printed by Valeo Martos, is 126.

Table 2.1: Summary of the number of specimens needed for each scenario

POINTS	SCENARIOUS	ORIENTATION	SPECIMENS	
			Total # (if produced in 1 JOB)	Total # (if produced in 1 JOB)
A	α	XY	16	R
			5	S
	β	Z	16	R
			5	S
B	α	XY	16	R
			5	S
	γ	XY	16	R
			5	S
	γ	XY	16	R
			5	S
C	α	XY	16	R
			5	S
Total number of specimens			126	

The creation of the STL file, which simulates the working area and the layout of the specimens in it, is done using Solidworks. The specimens in the 3D model printing area JOB simulation are spaced by a value between 4 ± 0.5 and 7 ± 0.5 mm, in order not to influence those nearby allowing complete thermal flow. At this point, the STL file was sent to Valeo Martos to proceed with the printing process.

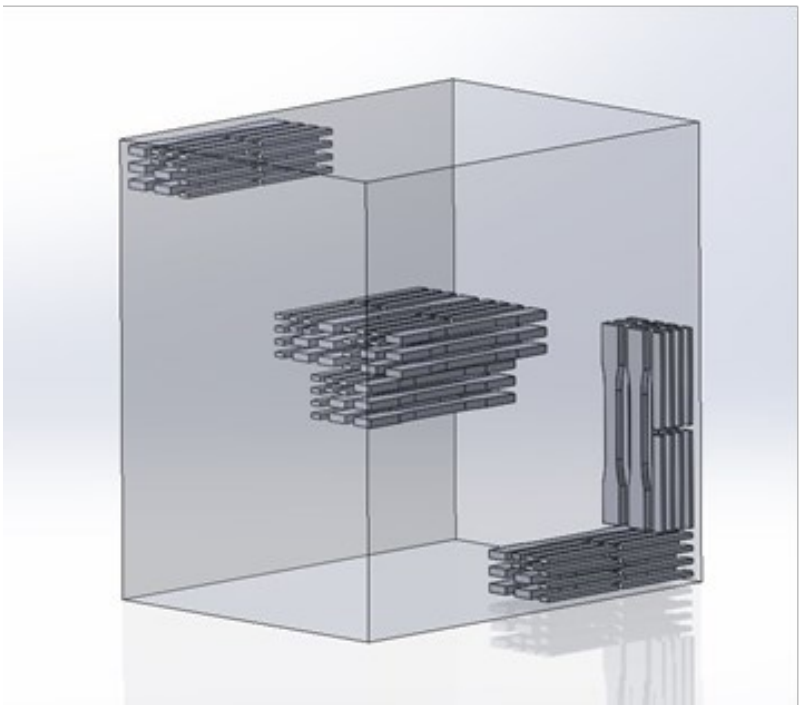

Figure 2.6: Printing area 3D model with all specimens in 1 JOB

2.5 Multi Jet Fusion Setup

This thesis is carried out on 126 specimens printed using the HP Jet Fusion 3D 4200 printer, placed in Valeo Martos prototypes department. In Figure 2.7 are shown the units assembling the printer and making up the printing process: the 3D printer and the post-processing station,

whose functioning is explained in the sub-chapter 1.3.1. Parts and powder are transferred using the modular build unit between the printer and the post-processing station. Parts are fabricated using “HP 3D High Reusability PA 12” powder, sourced from HP along with their detailing and fusing agents. The fresh material used is 20%. The print mode employed is “Balanced”, a parameter set designed to produce parts with an even ratio between mechanical and geometrical properties and print speed, allowing a good compromise between the mechanical strength and Young modulus (HP Inc., 2022). It’s the mode typically used in factories to produce parts. The layout of the print is shown in Figure 2.8. The samples were distributed in the build volume as explained in sub-chapter 2.4, with a space of 4 to 7 mm separating each part to allow complete thermal flow.

After printing, the parts are left cool in the powder bed, inside the Build Unit, before being unpacked, in fact, the selected cooling mode is “Natural”, the slower one. Compressed air is used to blow the loose powder off the parts before they are cleaned with a strong bristle brush to get rid of any remaining powder. The loosely bound polymer substance is subsequently removed from the printed items by bead-blasting with glass beads at 5-6 bars, using a Guyson Euroblast 6 blasting cabinet, leaving the surface smooth and uniform. All other parameters are pre-set by HP software and cannot be changed.

Figure 2.7: Prototype department of Valeo Martos (Spain)

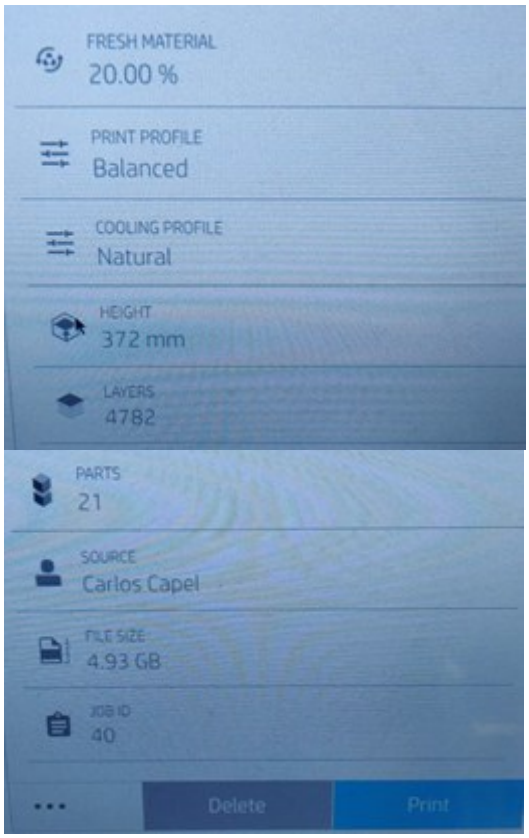

Figure 2.8: Printer Setup

2.6 Visual and Dimensional Characterization

Once printed, the 126 specimens were shipped from Valeo Martos to Valeo Santena. In Figures 2.9 and 2.10, the readers can see the specimens arrived, divided by type, R and S, and by position in the working area. Each specimen is visually analysed to note down the presence of moulding defects, identified by writing a number on it, photographed and its dimensions measured using a calliper. All specimens are therefore traceable through the notch made by Valeo Martos which distinguishes the position and direction of printing and through the number written with a felt-tip pen on them upon arrival. In fact, a big point in favour of Additive Manufacturing is to have the possibility of making the pieces individually traceable. If the factories take advantage of this advantage, the day they have problems with a component, can make a statistic and discover that one area of the moulding JOB is more compromised than the others. With injection mould they can have traceability only of the batches to do a risk analysis, it can't be so punctual.

It is important to note that the identification labels of each specimen is made in the center of the last printed section, the rougher one mentioned in chapter 1.4.3. Except for those printed in A in the Z direction of which the engraving is not very visible. This produces a decrease in the section therefore, in the absence of other defects, it is expected a failure during the mechanical tests triggered from this point.

Figure 2.9: Rectangular printed samples, type R

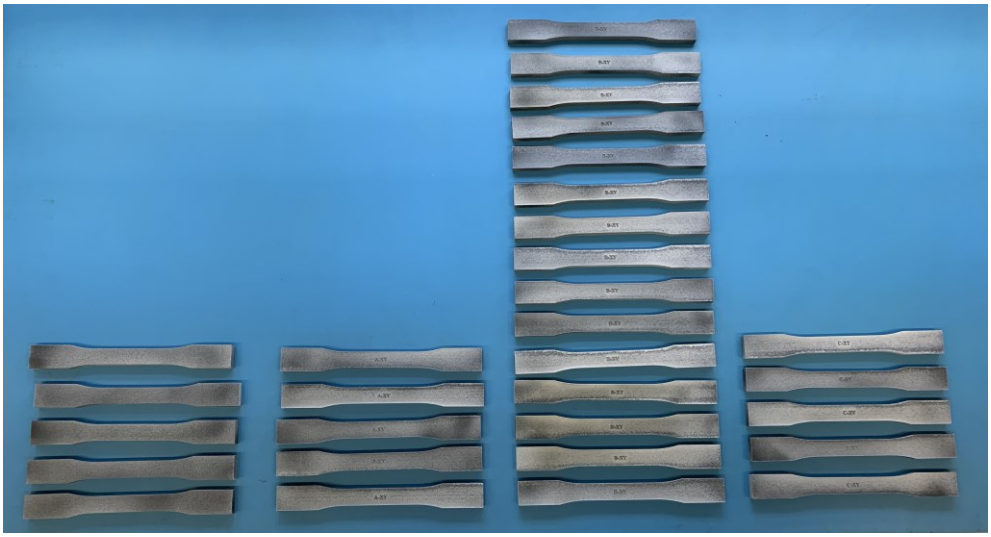

Figure 2.10: Printed tensile test-piece, type S

Visually, as photographed in Figure 2.11, it can be seen that the surfaces are not perfectly flat, especially for the specimens printed in position C, which have a slight warping defect.

Figure 2.11: Warping defect on the specimen surface

Furthermore, the defect on the edges of the specimen due to the capillarity effect, which is discussed in sub-chapter 1.3.2, is accentuated. This distinguishing feature of the Multi Jet Fusion process is shown in Figure 2.12, which influences the top planar surfaces of printed items. This flaw, which happens during component manufacture, is caused by the interaction

of the surrounding powder that has been impregnated with Detail Agent and the molten polymer. The liquid meniscus expands due to the difference in surface energy between the liquid substance and the wet powder. Surfactants, that are a part of the Detail Agent's chemical makeup, lessen this action. In the case of curved edges, the Mele, M. et al. paper suggests an analytical model for the prediction of the capillarity effect (2021).

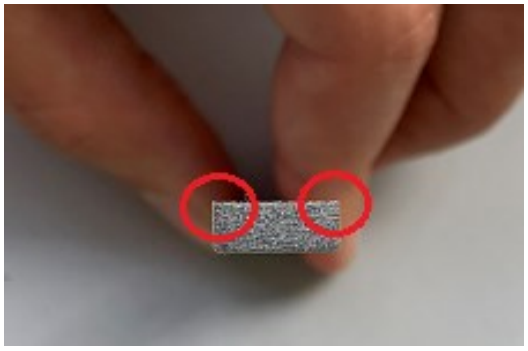

Figure 2.12: Capillarity effect on the edges of the specimen

It can be seen, with the "naked" eye and through the microscope positioned in Valeo Santena, that the surface corresponding to the initial layer fused (Figure 2.14 a) of each sample is smoother and more uniform than the side corresponding to the last layers fused in the JOB (Figure 2.14 b). This is in line with O'Connor, H.J. et al.'s results (2018), which detect higher roughness values for the top surface. The explanation is that a superior sintering process caused greater diffusion of polymers to fill gaps at the bottom of the component. This does not count for the specimens printed along the Z direction, both of whose surfaces are smooth, as the sections are fused perpendicular compared to the others. The type of equipment used is the Leica Microsystems Emspira 3 microscope, as shown in Figure 2.13. It's a digital video microscope with live images up to 60 frames per second and 4K resolution displayed immediately on the monitor, an 8:1 zoom range ratio with coded zoom that ensures the accuracy of the measurements, and other features.

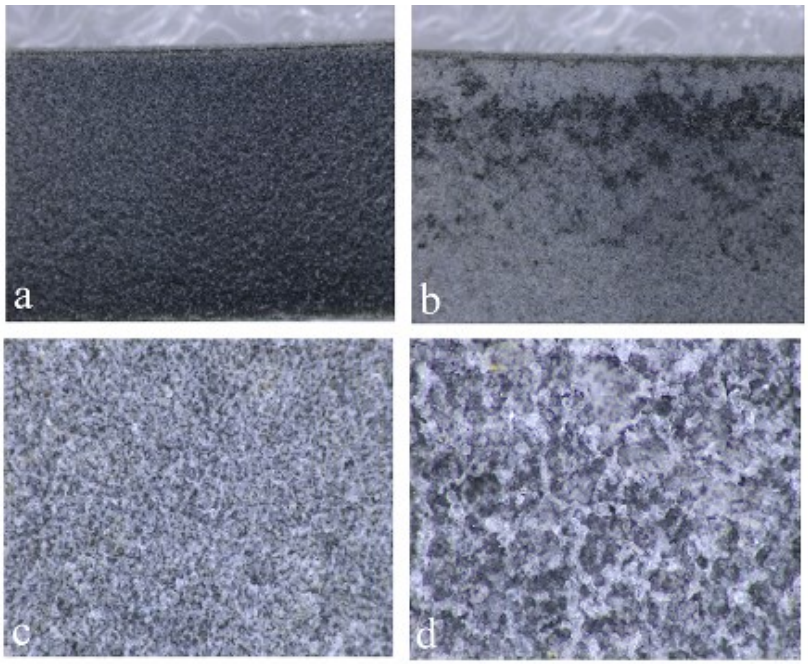

Figure 2.14: Specimen surfaces: a) bottom printed surface, b) top printed surface, c) microscope view of a, d) microscope view of b

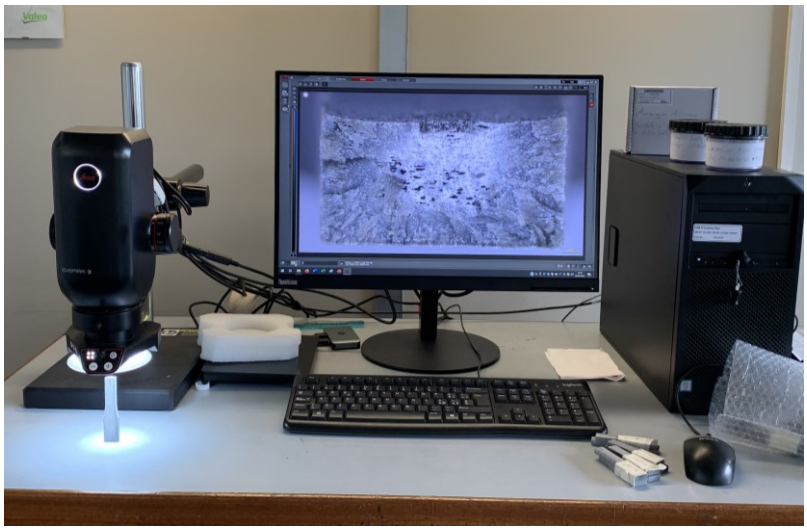

Figure 2.13: Microscopy emplacement in Valeo Santena

Subsequently, each sample is photographed and the visible defects and their dimensions are noted in a file using the digital caliper present in the Valeo Santena laboratory. This instrument, depicted in Figure 2.14, has a resolution of 0,01 mm.

Figure 2.14: Valeo Santena's digital caliper

The dimensions taken for the R and S types of specimens are numbered in Figure 2.15 where a stylised representation of these can be seen. Each dimension is measured three times and the average is entered into the table.

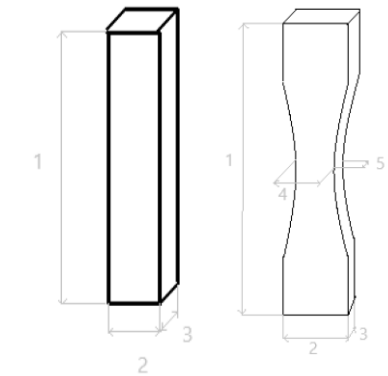

Figure 2.15: Stylised representation of the two types of specimens and the dimensions measured with the caliper

Subsequently, the repeatability and accuracy of the process are evaluated by calculating the Process Capability index (C_{pk}), a statistical measurement of a process's ability to produce parts within specified limits on a consistent basis. This calculation aims to provide dimensional information on the process distributed population achieved with the HP Jet Fusion 4200 Series 3D Printing Solution with HP 3D High Reusability PA12. Upper specification limits (USL) and lower specification limits (LSL), known as the process's "tolerance range," are established by dimensional quality control systems (equation 2.1). The center of this range, which is often the nominal dimension value, is the process's target. More measurements will fall inside the tolerance range the higher the C_{pk} number is. A procedure must be accurate and repeatable in order to be considered capable, so it's function of these two parameters (equation 2.2). The consistency of multiple measurements is referred to as repeatability or precision. It is contrasted with the C_p's measurement of the width of the specification limits. A measurement value's accuracy, which is determined by bias, is how closely it resembles the designated nominal. Process capability as evaluated by C_{pk} is only regarded as good if both requirements are satisfied. Bias is the discrepancy between the population's average value for a particular dimension and its desired value. While the process capability index C_P gauges a process's capacity to deliver consistent outputs by comparing its allowable spread to its actual spread (equation 2.3). This ignores the degree to which the output is centered around the desired nominal value. Standard deviation calculates the process's variability and dispersion and estimates sigma σ.

$$C_{pk} = \min\left[\frac{[USL-\mu]}{3\sigma}, \frac{[\mu-LSL]}{3\sigma}\right] \tag{2.1}$$

$$Capability = C_{pk} = C_p \cdot (1-2\cdot bias) \tag{2.2}$$

$$C_p = \frac{specification\ width}{process\ width} = \frac{(USL-LSL)}{6\sigma} \tag{2.3}$$

For statistical process control, a C_{pk} of 1,33 (4σ) is typically preferred, especially when working with multi-part complicated processes. To investigate the properties of the 3D printer present in Valeo Martos, are compared the capability values derived from the measurement of this research's specimens with the dimensional tolerance range given by HP for a target process capability of C_{pk} = 1,33. For nominal sizes between 0 and 30 mm, in XY the standard deviation found by HP is ± 0,25 mm while for values between 50 and 80 mm it is ± 0,37 mm. In Z direction the standard deviation is greater, for the first range it is ± 0,42 mm, while for the second it is ± 0,60 mm. The capability has not been calculated for the specimens in the Z direction as they are too few in number.

By setting the standard deviation introduced in the previous paragraph, for dimension number 3 in the rectangular sample, the thickness, with a nominal value of 4 mm, this study obtains a C_p of 0,87 and a C_{pk} of -0,13. As the readers can see also from the bar chart (Figure 2.17) and in the film of production (Figure 2.16) this dimension for the 80 items is not accurate and not repeatable. The specimens in the tolerance range are few and are located in the JOB, especially, in positions A and C.

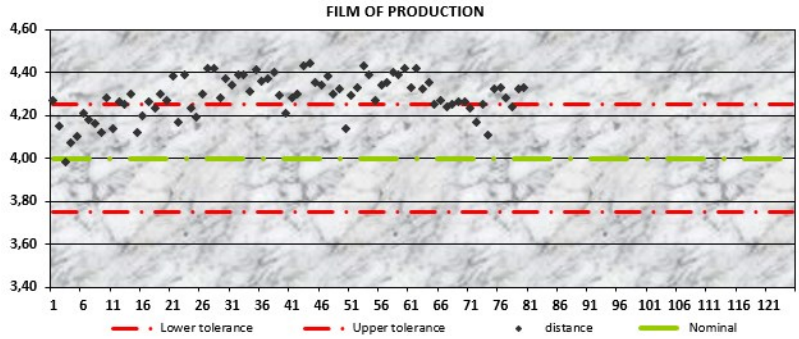

Figure 2.16: Film of production represented the tolerance range, the mean value and the measurements of the thickness of 80 specimens type R

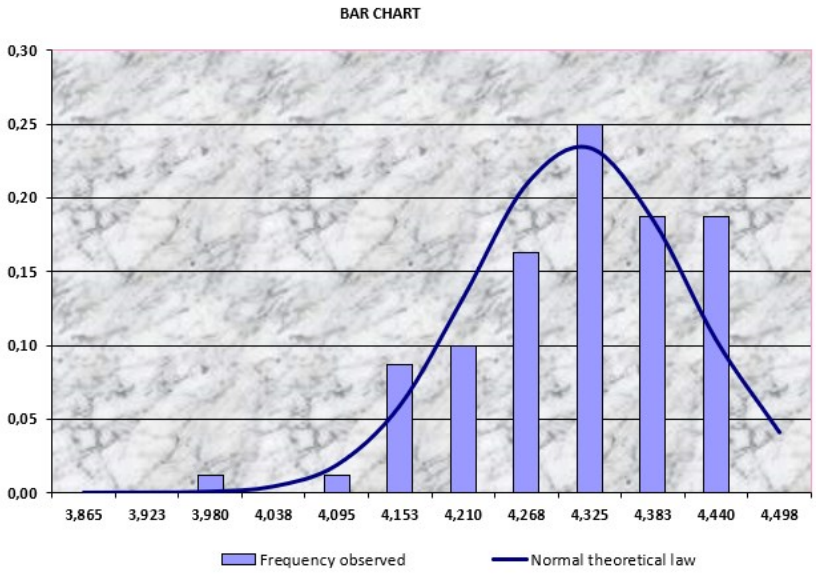

Figure 2.17: Bar chart represented the frequency observed and the normal theoretical law for the measurements of the thickness of 80 specimens type R

By setting the standard deviation introduced in the previous paragraph, for dimension number 2 in the rectangular sample, the width, with a nominal value of 10 mm, this study obtains a C_p of 1,72 and a C_{pk} of 0,04. As the readers can see also from the bar chart (Figure 2.19) and in the film of production (Figure 2.18) this dimension for the 80 items is repeatable, but not accurate. As a matter of fact, it has good C_p (low variability) but high bias. This time the specimens in position A have measurements out of range.

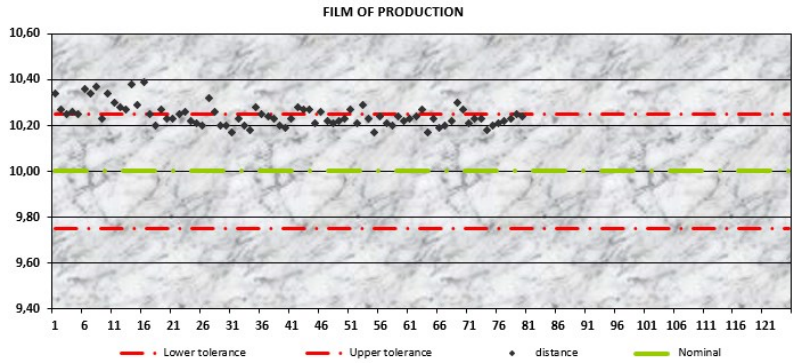

Figure 2.18: Film of production represented the tolerance range, the mean value and the measurements of the width of 80 specimens type R

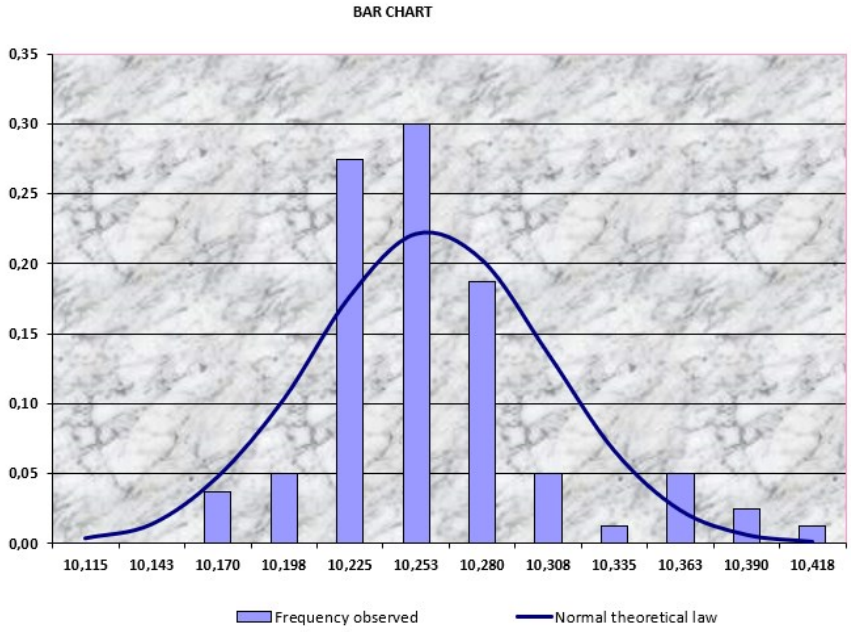

Figure 2.19: Bar chart represented the frequency observed and the normal theoretical law for the measurements of the width of 80 specimens type R

By setting the standard deviation introduced in the previous paragraph, for dimension number 1 in the rectangular sample, the length, with a nominal value of 80 mm, this study obtains a C_p of 1,31 and a C_{pk} of 1,13. As the readers can see also from the bar chart (Figure 2.21) and in the film of production (Figure 2.20) this dimension for the 80 items is both, repeatable and accurate. As a matter of fact, it has low bias and C_p so C_{pk} good, but the last is still not 1,33. For this dimension, it is found that the specimens printed in position B are the most accurate and repeatable, while those in the other positions have more dispersed measurements.

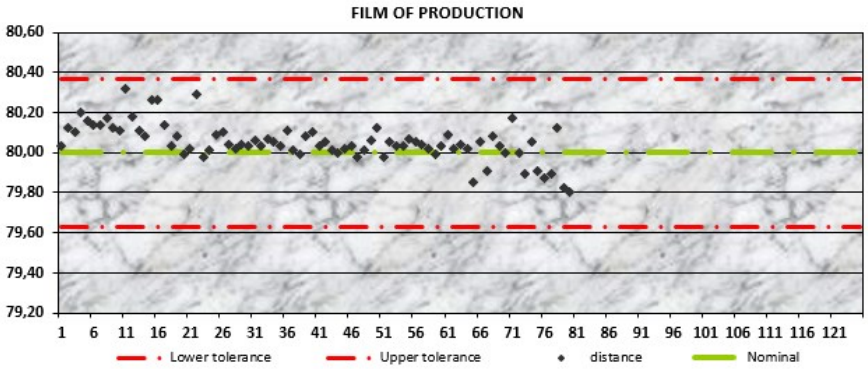

Figure 2.20: Film of production represented the tolerance range, the mean value and the measurements of the length of 80 specimens type R

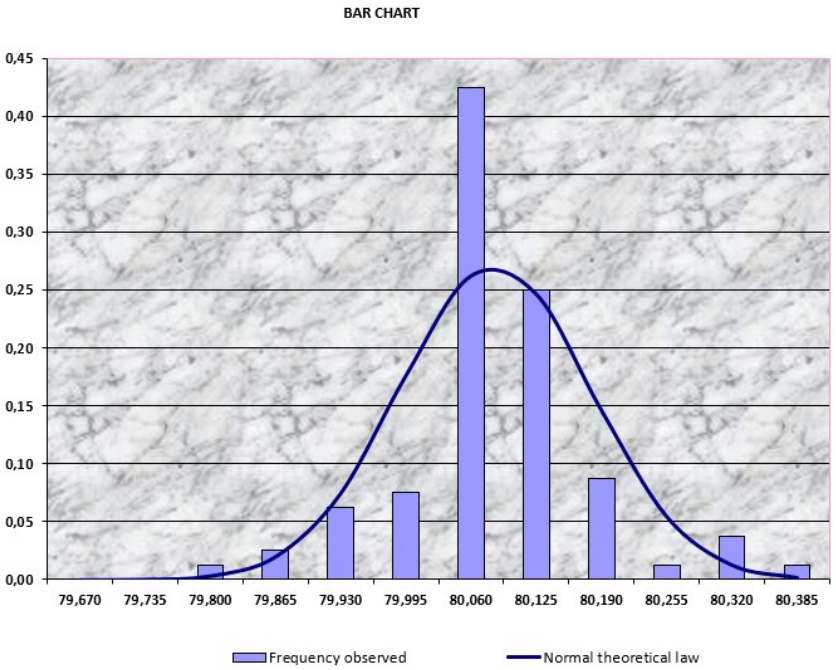

Figure 2.21: Bar chart represented the frequency observed and the normal theoretical law for the measurements of the length of 80 specimens type R

The capability for the specimens type S is not calculated due to a lack of sufficient quantity to adequately measure it, only in the XY direction, and because the same results were noted by taking the various dimensions.

3. Testing

This chapter debates the experimental methodologies that are the basis of this thesis work. It describes the instrumentation, the procedures used, the main formulas and the elaborations made of the collected data, reported in chapter 4. Specified rules that define the geometrical parameters of the test components, the machine features, the test settings, and the methods for processing the data govern how the tests are carried out. It is divided into various sub-chapters based on the type of test performed. The tests were conducted at the Polytechnic of Turin, in the laboratories of the DISAT, Materials Science and Technology, and DIMEAS, Mechanics departments, which have the appropriate characterization instrumentation.

3.1 Chemical Characterization

3.1.1 FTIR-ATR

FTIR-ATR is a technique of analysis and screening of the materials' surface for their characterization, which identifies the components present in them. Thanks to the high sensitivity towards organic chemical groups, the speed of execution and the absence of sampling and preparation of specimens, it is very suitable for multi-component materials with a predominantly organic nature.

The study of molecular movements and structure through the absorption, emission, and scattering of light is known as spectroscopy. As explained by Smith, J.G.et al. (2018), a molecule is in constant vibration, as its bonds lengthen or shorten, and they bend towards each other. In the first case, the book speaks of valence or stretching vibrations, in the second of deformation or bending vibrations. The absorption of infrared radiation, or rather, located beyond (lower frequency, length higher wave, lower energy) of the red end of the visible spectrum, causes a variation in the molecule vibration. The recording of the absorption of this type of radiation constitutes the infrared (IR) spectrum of the molecule. The units of measurement of the infrared spectrum are the wavelengths, expressed in microns [μm], or better, the frequencies expressed in numbers wave [cm^{-1}], corresponding to the reciprocal of the wavelength. The infrared spectrum is quite characteristic for every organic compound and, among other applications, it also serves to distinguish compounds from each other. In fact, if two compounds have exactly the same infrared spectrum this means that they have the same thousands, there are many different frequencies of absorption, of physical properties and consequently, with safety almost absolute, identical chemical structure. The examination of the infrared spectrum also helps to establish the structure of a compound unknown, specifying which functional groups are present in the molecule. Every single group of atoms has its own characteristic absorption band, or rather, it always absorbs light at a certain frequency, whatever the compound in which it is present. However, the interpretation of an infrared spectrum is not as simple: some bands can be hidden by the overlap of other bands, and absorption bands due to individual groups can be "shifted" from various structural features, consequently exchanged for bands of totally different groups. With the development of potent computers in recent decades, a new generation of spectrophotometers known as interference (FT-IR), which use a mechanical tool known as a Michelson interferometer instead of a monochromator. In addition to the traditional infrared transmission spectroscopy, a method based on the total attenuated reflectance concept appears (ATR). In this instance, infrared radiation travels through a certain crystal that is transparent to IR, allowing the electromagnetic wave to repeatedly reflect back inside. The IR radiation from the spectrometer reaches the crystal after the sample surface has been pressed against it. The IR radiation then reflects through the crystal and enters the sample for a small fraction of

microns before being somewhat absorbed or attenuated. The spectrophotometer can detect enough attenuation of the IR beam intensity following some reflections to produce an FT-IR spectrum with attenuated total reflectance (ATR).

Thermo Scientific Nicolet iS50 FT-IR Spectrometer, shown in Figure 3.1, was used in order to perform attenuated total reflectance-infrared spectroscopy (ATR-FTIR) on dried samples. For each sample, 32 ATR spectra with a resolution of 4 cm^{-1} were gathered in the 4000-500 cm^{-1} region. This instrument is located in the DISAT laboratory of the Polytechnic of Turin, Italy.

Figure 3.1: Thermo Scientific Nicolet iS50 FT-IR Spectrometer own by the Polytechnic of Turin, Italy

The test is carried out on the rectangular specimens, type R, printed for each position, printing orientation and aging time step (Figure 3.2), before testing them through the bending test. Since is a non-invasive test, it only needs a flat surface to perform it. The data taken from the machine, Wavenumbers [cm^{-1}] and Absorbance [-], were downloaded as text files and subsequently reprocessed with the software Origin, creating the corresponding graphs in subchapter 4.1. Information regarding the peaks of the waves found are researched from the web and compared with those present in the literature for PA12.

Figure 3.2: Thermo Scientific Nicolet iS50 FT-IR Spectrometer own by the Polytechnic of Turin measuring the PA12 specimen

3.2 Thermal Characterization

3.2.1 DSC

Direct measurements of transition enthalpies on solid and liquid samples can be made using the differential scanning calorimetry (DSC) technique. In a DSC experiment, the sample and a thermally inert reference are heated at a regulated rate, and a signal proportional to the gap in heat capacity between the sample and the reference is recorded as the temperature. The temperature range being sampled must be close to the transition temperature.

The DSC instrument is a calorimeter chamber with an integrated thermocouple that measures T inside the chamber and the heat emitted. It measures whether a given transition is exothermic (releases heat) or endothermic (absorbs heat). DSC is composed of the Heating Block, which is heated to a specific temperature T_b by the Heater. The Heating Block serves as a thermodynamic heat reservoir and has an endless heat capacity. The temperature gradient, also known as the "thermal ramp," or "temperature ramp," is controlled by the predetermined program and varies over time at a predetermined speed. The temperatures of the sample (T_S) and of the reference sample (T_R) will fluctuate as T_b fluctuates, and there will always be two heat flows, Q_S and Q_R, from the heating block towards the sample and reference compartment (Stagnaro, P. et al., 2016). During thermal scanning, the equipment uses thermocouples to monitor the temperature T_S and the temperature difference $\Delta T = T_S - T_R$. The reference is typically α-alumina, which is thermally inert in the temperature range where the measurement takes place. The transition occurs at constant T_S until the entire sample becomes liquid because the sample is thermally inert in the pre-transition temperature area and its temperature T_S will be different from T_R. After that, T_S begins to rise once more, and the ΔT value, which was $C_{P,solid} \neq C_{P,liquid}$ may differ from the value obtained prior to the transition. This produces a curve on the Heatflow-Temperature diagram, where the melting and crystallization phase transitions can be seen in Figure 3.3. These are of the first order because they depend on the first derivative of heat, so they are represented as peaks. These two peaks are in different directions due to the fact that, for crystallization, the reaction of the functional groups releases heat, so the peak is towards the exothermic part. While functional groups need heat for fusion, in fact, it is a process that takes place with heat absorption, it is therefore towards the endothermic part. On the other hand, the glass transition temperature is a second-order

property, so it is described by an inflection. The meaning of melting, crystallization and glass transition temperatures can be found in subchapter 1.4.1, where they are explained in detail. Lastly, if the specific heat of fusion of the sample ΔH_f (J/g), equation 3.1, is compared to the specific heat of fusion of 100% crystalline of same polymer ΔH_f^0, which for the PA12 is 209.3 J/g (Rosso, S. et al., 2020), can be determined the crystallinity percentage (C%), written in equation 3.2.

$$Heat\ of\ melting\ (\Delta H_f) = \frac{Area\ under\ the\ melting\ peak\ (W - °C/g)}{Heating\ Rate\ (°C/s)} = \left(\frac{J}{g}\right) \tag{3.1}$$

$$Crystallinity\ (\%) = \frac{\Delta H_f}{\Delta H_f^0} \times 100 \tag{3.2}$$

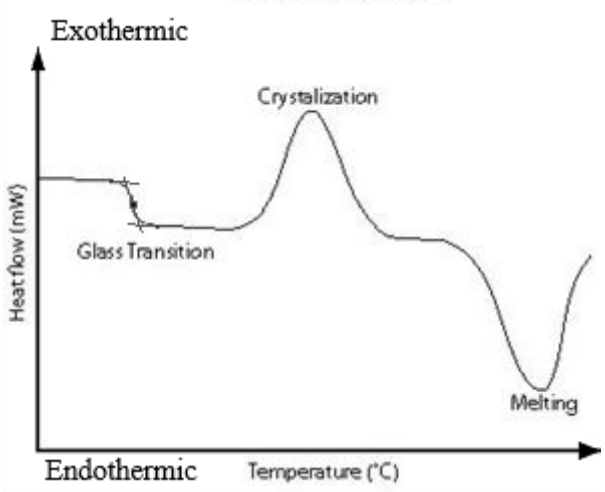

Figure 3.3: Features of a general DSC curve

Differential Scanning Calorimetry (DSC) analyses are performed on a Differential Scanning Calorimeter Mettler-Toledo DSC1 present in the DISAT laboratory of the Polytechnic of Turin, with a heating rate of 10 °C/min in a nitrogen atmosphere to analyse the thermal history of PA12 powder printed with MJF technology. The other instruments used for this test are a lancet, a razor blade and the sample container, the Radwag scales available and the laboratory press (Figure 3.5 a, b, c).

Figure 3.4: Differential Scanning Calorimeter Mettler-Toledo DSC1 own by the Polytechnic of Turin, Italy

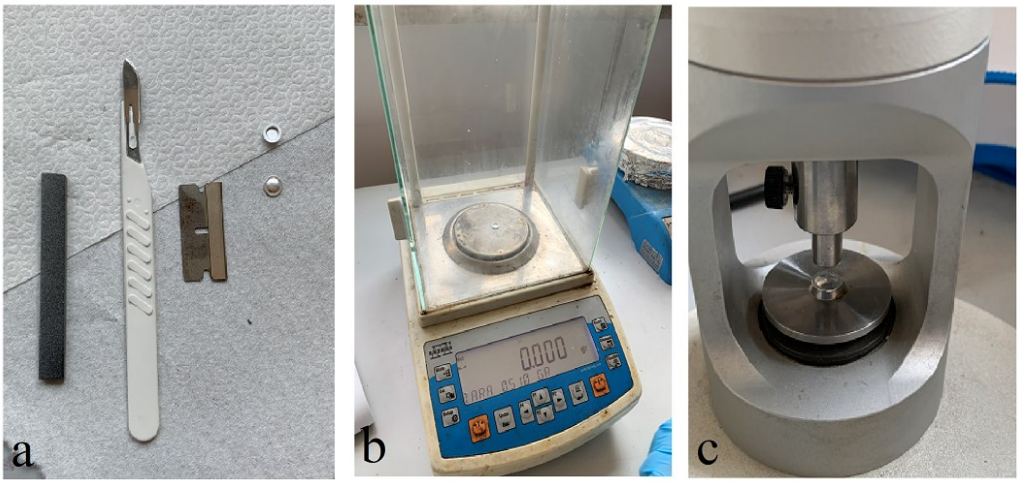

Figure 3.5: Equipment needed to carry out the DSC test: a) the designated specimen, a lancet, a razor blade and the sample container, b) Radwag scales, c) laboratory press

This study follows the D7426-08 procedure (American Society for Testing and Materials International, 2013). Each time a new day of analysis is started, it is advisable to calibrate the DSC based on the Indium (In) test specimen weighing 6,841 mg with the method saved on the computer software. Using a scalpel and a razor blade, an adequate quantity of splinters is collected for each specimen, prepared from the available section of the part, surface and bulk (Figure 3.6 a). After calibrating the Radwag scales on the weight of the sample holder, the splinters are introduced, checking that their weight is around 10 mg. The precise value to be entered in the software connected to the machine is noted, and the sample holder is closed with its corresponding cap, proceeding to seal it hermetically using a press as shown in Figure 3.5 c. Subsequently, the cap is pierced through a needle to decrease the

pressure inside the specimen holder during the test. Everything is inserted in the appropriate seat inside the chamber facing the standard aluminium specimen as shown in Figure 3.6 b. The thermal trend that the machine must follow has been entered in the software installed on the computer connected to the DSC machine. In this thesis, a first isotherm was applied at T = 25°C for five minutes. Subsequently, a ramp with a Heating Rate of 10 K/min., from a starting temperature of 25°C to a finishing one of 280°C, as shown in Figure 3.7. Then, measuring the heat difference in reference to the alumina sample, the DSC produced a text file with the results. The collected data are processed in Origin by plotting the Heatflow as a function of the temperature. Through the functions of this software are found: the minimum of the curve corresponding to the melting temperature and the inflection point, or rather, the midpoint of the tangent to the step. This corresponds to the glass transition temperature, a point is extrapolated, although this corresponds to a range. Lastly the area under the melting curve was found through Origin and the calculation reported in equation 3.2 is made on Excel to calculate the percentage of crystallinity of the specimen.

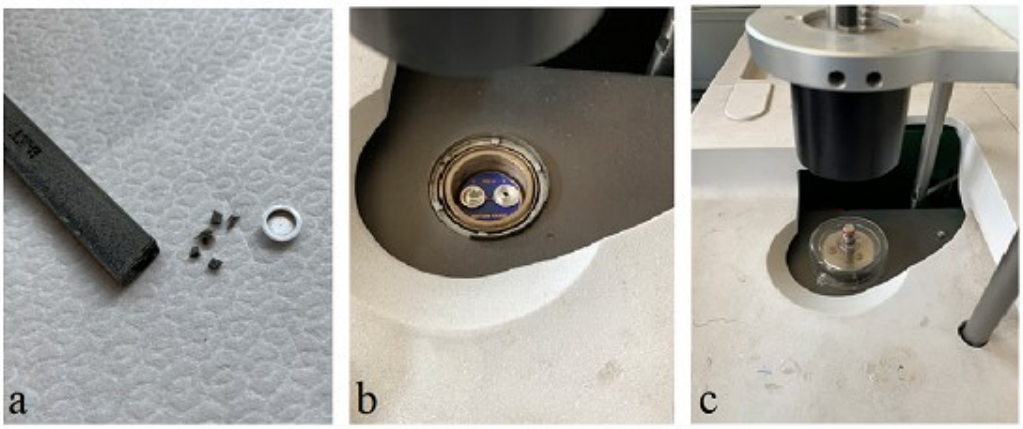

Figure 3.6: Procedure to perform the DSC test: a) designated specimen with the splinters collected, b) the calorimeter chamber opened, c) the calorimeter chamber closed

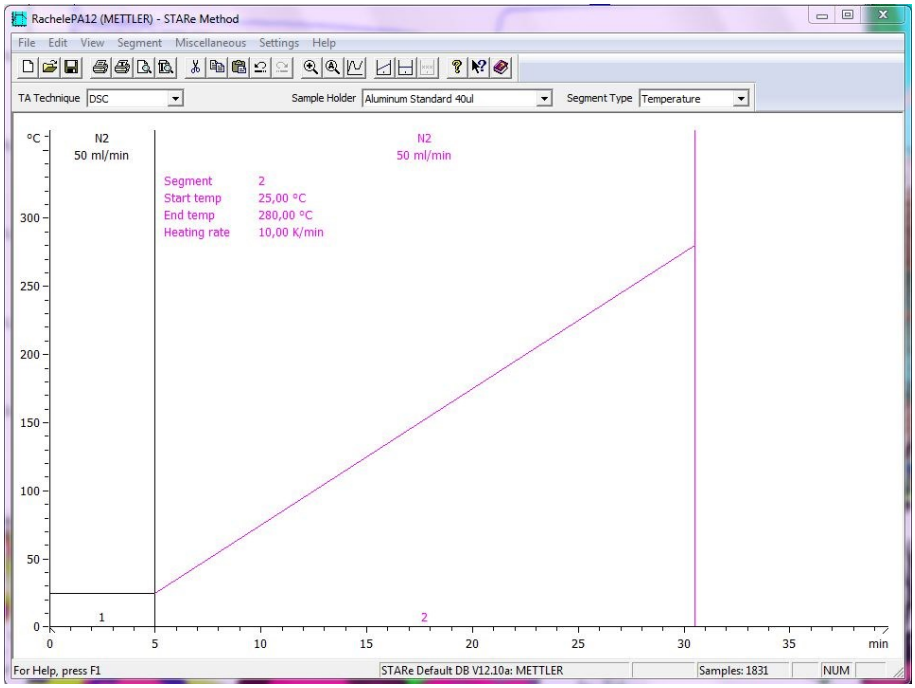

Figure 3.7: Thermal method setup

3.3 Mechanical Characterization

3.3.1 Tensile testing

The tensile test is the most used technique for experimentally assessing the mechanical properties of a material structure. A test specimen, cylindrical or prismatic, is subjected to increasing uniaxial tensile loads, usually until it breaks. During the test, load-elongation values are recorded in order to create the necessary diagram, an example is shown in Figure 3.8.

The way the tests are conducted is governed by specific criteria that specify the test samples' geometrical specifications, how the load is applied, and how the data are processed. Standardized tests D638 – 14 specify test tube geometry, machine characteristics, test conditions, and result processing (American Society for Testing and Materials International, 2014). The specimens to be used for the tensile tests have unified shapes and dimensions because the results obtained may be to some extent influenced by the geometry of these. In this case, the research employs the sample type S described in Chapter 2. The section is rectangular with distinguished: the calibrated part, the two gripping heads and the two connection areas. The calibrated part is the constant section area with controlled dimensions and length L_0, which is used for measurements (Goglio, L., 2015). The ends of the sample with a bigger section than the calibrated part that is grabbed by the machine clamps for the delivery of the tensile force are referred to as the gripping heads. By connecting the calibrated component to the gripping heads, the connection areas prevent abrupt section fluctuations. The test machines allow exerting traction on the test samples, in a controlled way, with the movement of the crosspiece generated by operating screws (mechanical drive) or by actuator cylinders (hydraulic drive). In this case, since the specimens were made of a polymer, therefore of a presumably ductile material, it is better to use the second type of traction machine. One clamp is connected to the base, the other is integral to the movable crosspiece; the displacement of the latter puts the sample in traction. A specific dynamometer known as a "load cell" that operates using a full bridge strain gauge circuit and is connected in series on the application of tensile force is used to measure the force. To be more precise, the measurement of the elongation of the sample is performed in two different ways: a sensor incorporated in the machine is used for the plastic phase, while an extensometer is used for the elastic behavior. The first one has moderate accuracy, so is good for big deformations, the second one is a special instrument that is hooked to the sample, and which measures the distance between two reference sections. It has a very high resolution (<1 μm) but the stroke measurement is short, a few mm, this technique is therefore used to measure elongation rubber bands that are small in size.

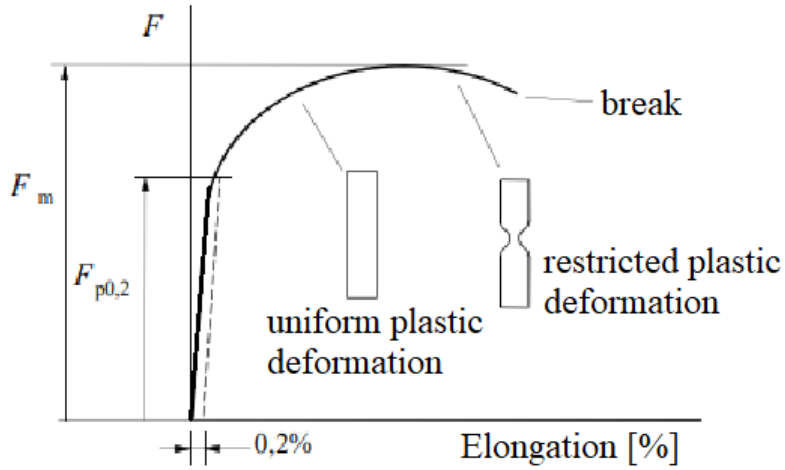

Figure 3.8: Features of a general Load-Elongation curve

Obviously, the response of different materials subjected to traction varies greatly depending on the type and the treatments that have been applied. In the initial phase of the test, as long as the load is kept low enough, the behavior of the material is elastic, and the corresponding section of the diagram is linear. Continuing to exert the traction on the test sample the curve reaches a certain level for which the force and the elongation ceases to be proportional and the diagram deviates from linearity; from this point onwards, the behavior differs according to the type of material under examination. For some materials, the force suddenly ceases to rise. The phenomenon is called enervation, it marks the end of the behavior elasticity of the material and the onset of permanent plastic deformations. Subsequently, continuing to exert traction on the specimen, the force starts to rise again, but with a slope much lower than that of the elastic section: we are in the deformation phase of plastics having a much higher entity than the elastic ones. In this phase the volume of the material is kept approximately constant, so the elongation is compensated by a contraction transversal. The fact that the force continues to rise, despite the reduction of the section, indicates that the unit load required to deform the material grows to such an extent that compensates for the loss of resistant section: this phenomenon is known as work hardening. This behavior continues until the curve has a maximum F_m, also called breaking load; from this point onwards if the reduction of the section occurs in a localized area, this phenomenon is known as nipping (Goglio, L., 2015). The force required to further stretch the tube decreases because the hardening of the material is no longer sufficient to compensate for the reduction in section. Finally, the specimen breaks, dividing into two parts at the restricted section. The definitions and equations useful for calculating the characteristic values to characterize any type of material will be listed below. Conventional deformation or “strain”, equation 3.3, is the ratio between the variation in the length of the calibrated section between the two references and the initial length of the section itself (L_0). For specimen type S the L_0 = 57 mm, type I on the Standardized tests D638 – 14 (American Society for Testing and Materials International, 2014). Conventional tension or “stress”, equation 3.4, is the ratio between the applied tensile force moment by moment and the area initial of the straight section of the calibrated section S_0. For this type of specimen printed $S_0 = 7 * 13 = 91$ mm^2. The slope of the linear elastic behavior in the diagram σ- ε represents the elastic or Young modulus E. The load of deviation from proportionality is the load to which it corresponds a non-proportional elongation equal to the percentage p of the distance between the references. $F_{p0,2}$ is the load that determines an elongation having a non-proportional share equal to 0.2% of the distance between the references, equation 3.5. The breaking load is the maximum value

of the curve, it is not necessarily the force under which the element breaks, this can be a subsequent lower force. The elongation after break (%), equation 3.6, is the difference between final value L_u and initial L_0 of the distance between the two references drawn before the test, compared to L_0. For definition the two pieces of the sample are brought closer together after the test and measuring their length, the permanent and irreversible extension is found, without the elastic one.

$$Strain = \varepsilon = \frac{\triangle L}{L_0} \tag{3.3}$$

$$Stress = \sigma = \frac{F}{S_0} \tag{3.4}$$

$$0,2\% Offset\ yield\ strength = R_{p,0,2} = \frac{F_{p,0,2}}{S_0} \tag{3.5}$$

$$Elongation\ after\ break\ (\%) = A = 100\,\frac{L_u - L_0}{L_0} \tag{3.6}$$

The tensile test is carried out using the INSTRON 8801 (Figure 3.9) machine present in DIMEAS laboratory of the Polytechnic of Turin, Italy, and an extensometer. This external sensor is formed by a bifurcation, the ends of which are fixed perpendicularly to the traction section of the specimen, by means of rubber bands, at an initial reference distance, moving them away by measuring ΔL.

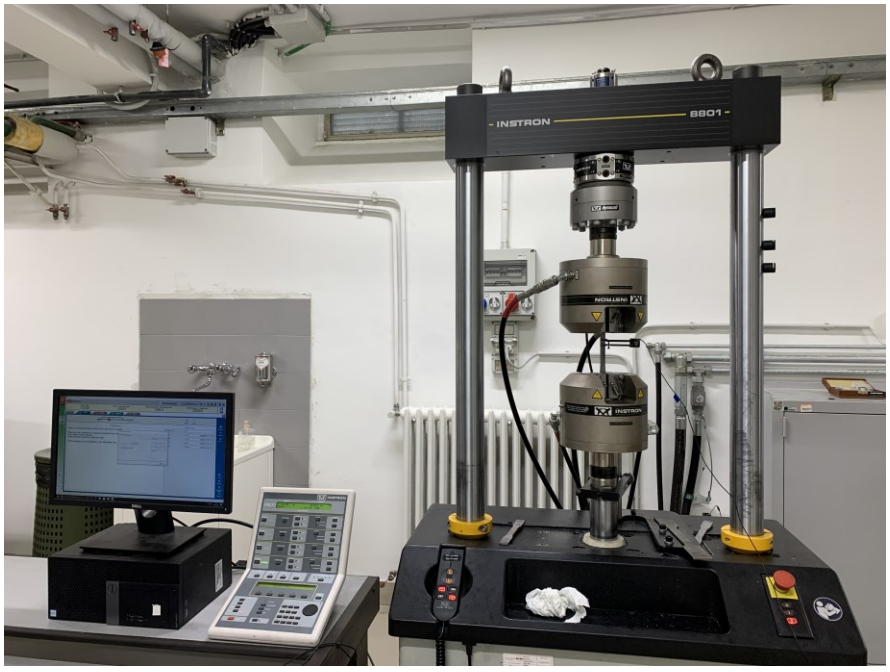

Figure 3.9: INSTRON 8801 tensile machine present in the DIMEAS laboratory of the Polytechnic of Turin, Italy

As photographed in Figure 3.10, the strain gauge is placed above the identification incision of each specimen, since it was assumed that this could be the breaking section. Once the correct pressure of the pump for the test sample has been set, we proceeded to insert it in the jaws and activate the test through the dedicated software installed in the computer connected to it. The software processes the data of the external strain gauge, and those of the

force applied and the stroke performed by the machine, inserting them in a text file and extrapolating a first view of the Force-Stroke curves, respectively in N and mm. The data processing is carried out through Excel 2020 and the Origin 2018 software. The load-stroke data obtained for each specimen, to be compared with each other, are shifted to the origin and graphed through Origin. To calculate the information necessary to characterize the specimens as described in standard D638 – 14, it is necessary to switch to the Stress-Strain curves (American Society for Testing and Materials International, 2014). Each value of the curve is calculated as shown in equations 3.3 and 3.4. Once these graphs are obtained for each scenario, Young's modulus, yield strength, tensile strength and elongation at break are calculated using Origin. To identify the elastic part of the curves, a straight line was drawn, starting from the origin, which best approximated the linear trend of this first part. Having found the limit value of deviation from linearity, corresponding to the intersection between the drawn line and the curve, two points quite distant from each other within this range are taken. The slope, or rather the angular coefficient, of the straight line passing through these two points is then calculated. This value corresponds to Young modulus of the curve. To calculate the yield instead, the line that best represents the linear section is translated as 0,002 on the abscissa. The stress corresponding to the interpolation of the line with the curve is the yield strength. In the plastic section, on the other hand, can be obtained the ultimate tensile strength as the maximum stress that the specimen can withstand, the maximum of the curve. After this the curve has a decreasing trend. To calculate the elongation at break, on the other hand, through Origin, the strain at break is determined as the last point of the curve, then a straight line is drawn from this with the same angular coefficient as the elastic part. The intersection between this line and the abscissa gives the elongation at break. The same procedure is repeated for each curve and, as indicated by the standard, the arithmetic average of the values found and their standard deviation for each scenario is made, shown in the table in Chapter 4, corresponding to the results. Furthermore, the breaking section is looked under the microscope own by Valeo Santena (Figure 2.13).

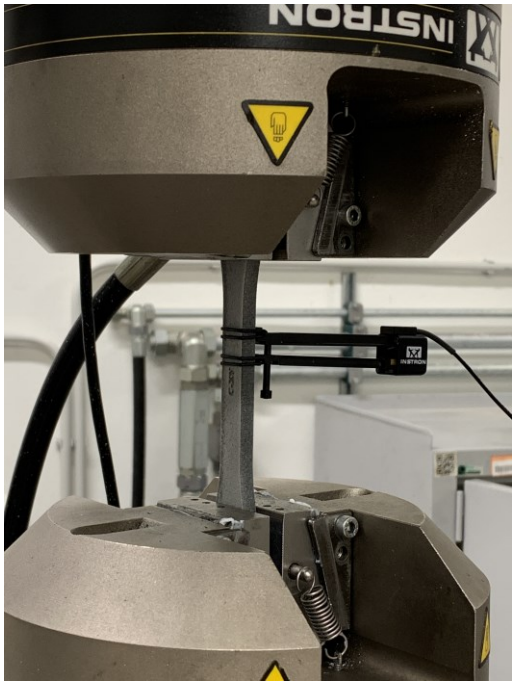

Figure 3.10: Sample and extensometer placed in INSTRON 8801 tensile machine

3.3.2 3-Point Bending Flexural test

The simulation's objective is to accurately represent a three-point bending test of a system made up of PA12 specimens so that their mechanical property, bending stiffness may be determined.

The regulations followed and readjust to determinate the flexural properties for a 3-Point Bending test is D6272 – 17 (American Society for Testing and Materials International, 2017). A bar with a rectangular cross section rests on two supports and is loaded once, at a location that is equally spaced from the neighbouring support points. The load span is one half of the support span (see Figure 3.11) with a 16:1 support span to depth ratio. Until the outer fibers rupture or the maximum fiber strain of 5% is reached, whichever comes first, the specimen is deflected. Furthermore, the greatest axial fiber stress in three point bending is placed directly beneath the loading nose. A fully calibrated testing apparatus is employed, and the error in the load measurement system shall not exceed 6% of the maximum load anticipated to be measured. This apparatus is capable of functioning at constant rates of crosshead motion over the range indicated. It must have a tool for measuring deflection. The surfaces of the loading noses and supports must be cylindrical. The radii of the loading noses should be kept as small as possible to prevent excessive indentation or failure brought on by stress concentration right under the loading noses. If there is a severe indentation or compressive failure, they must be this big. To avoid the specimen coming into contact with the noses' sides, the arc of the loading noses in contact with the specimen must be sufficiently wide. During the test, the equipment must automatically and constantly record the deflection.

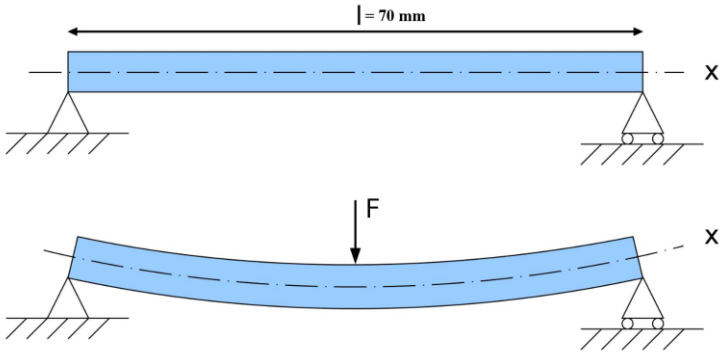

Figure 3.11: Schematic representation of the specimen exposed to 3-Point Bending Flexural test

The 3-Point Bending Flexural test is carried out using the MTS Elite Modular Control System QTest/10 machine, shown in Figure 3.12, present in DIMEAS laboratory of the Polytechnic of Turin, Italy. To choose the appropriate load to apply, the maximum bending moment that a type R specimen can support and therefore the corresponding force is calculated. The latter was found equal to 76.2 N, therefore a load of 500 N, with a velocity of 10 mm/min is applied to the sample.

Figure 3.12: MTS Elite Modular Control System QTest/10 machine, shown in Figure 3.12, present in DIMEAS laboratory of the Polytechnic of Turin, Italy

Once the correct basement for the test has been set, it's time to insert the sample in the correct position on the two cylindric supports, in a symmetric way and activate the test through the dedicated software installed in the computer connected to it. The software processes the data, the force F by means of the load cell of the test machine and the strain, inserting them in a text file and extrapolating a first view of the Force-Stroke curves, respectively in N and mm. The data processing is carried out through Excel 2020 and the Origin 2018 software. The load-stroke data obtained for each specimen, to be compared with each other, are shifted to the origin and graphed through Origin. The information calculated to characterize the specimens are: in the plastic section, the ultimate tensile strength as the maximum stress that the specimen can withstand, the maximum of the curve. After this the curve has a decreasing trend. In addition, the last point of the curve was compared without removing the non-elastic part, called the strain at break. The same procedure is repeated for each curve and, as indicated by the standard, the arithmetic average of the values found and their standard deviation for each scenario is made, shown in the table in Chapter 4, corresponding to the results. Furthermore, the breaking section is looked under the microscope own by Valeo Santena (Figure 2.13).

Figure 3.13: Sample behaviour during the 3-Point Bending Flexural test

3.3.3 Izod Impact Strength test

A dynamic test required for evaluating a material's impact resistance is the Izod impact strength test. It is the main impact test, with Charpy pendulum. In both cases, a load is applied by means of an oscillating pendulum and, from the notch done on the specimen, the fracture arises during the test. What changes between the two is the type of sample and its location. In Izod test the specimen is wedged on one side and is impacted at the free end. The fracture toughness is evaluated based on the energy required for doing this and is measured by the height reached by the pendulum after the fracture of the specimen.

An arm that pivots is raised to a certain height, then let go. The sample is broken when the arm swings downward and strikes a notched sample. The height the arm swings to after striking the sample is used to compute the amount of energy that was absorbed by it. To calculate impact energy and notch sensitivity, a sample with notches is typically employed. That is because the notch produces a stress concentration that increases the probability of a brittle, rather than a ductile, fracture. All test findings are expressed as the amount of energy absorbed per unit of specimen width or per unit of cross-sectional area under the notch.

In the absence of an Izod pendulum within the Mechanical Department (DIMEAS) of the Polytechnic of Turin, the Charpy pendulum already present in there, an Instron CEAST, has been adapted. A device has been designed by means of Solidworks, to carry out tests on these specific materials in compliance with the D256 - 10 standard (American Society for Testing and Materials International, 2010). The overall assembly consists of a base, a vise with a fixed and a movable abutment part, and the indenter, as seen from the 3D view in figure 3.14. The latter is a mass that falls and passes its kinetic energy to a specific region of the specimen. Thanks to this software, the indenter was designed to have the same weight as the previous one of Charpy, that is m = 300 g. The slots of the base were fixed by means of nuts to the fixed part of the previous Charpy pendulum. The standard provides the striking edge radius, or rather, the impact radius that the indenter must have, equal to 0.80 ± 0.20 mm, and the distance between the point of impact and the upper side of the jaws, or rather, half of the specimen, which must be 22 ± 0.05 mm. The overall assembly consists of a base, a jaw with a fixed and a movable abutment part, and the indenter, as seen from the 3D view in figure 3.14. The latter is a mass that falls and passes its kinetic energy to a specific region of the specimen. Thanks to this software, the indenter was designed to have the same weight as the previous one of Charpy, that is m = 300 g. The slots of the base were fixed by means of nuts to the fixed part of the previous Charpy pendulum. The standard provides the striking edge radius, or rather, the impact radius that the indenter must have, equal to 0,80 ± 0,20 mm,

and the distance between the point of impact and the upper side of the jaws, or rather, half of the specimen, which must be 22 ± 0,05 mm. The tables of the project, sent to the external engineering firm, can be found in the appendix at the bottom of the thesis.

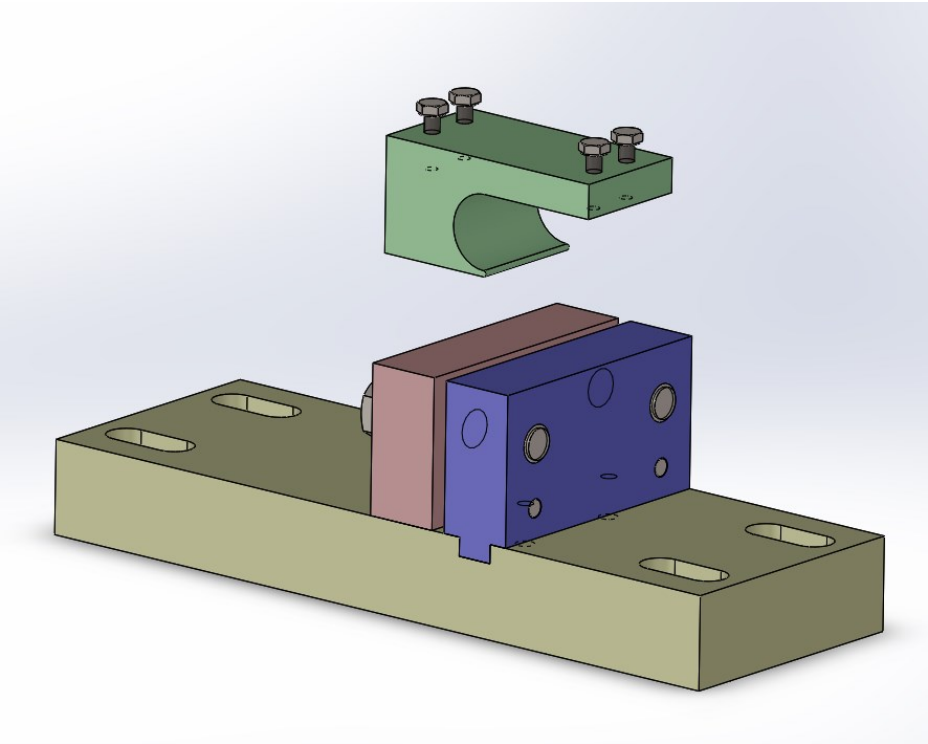

Figure 3.14: 3D project of the base, the vise and the indenter
to perform the Izod Impact Strength test

Once the designed assembly arrived, in Figure 3.15, made by an external company, it was observed that it had no defects and we proceeded to weigh the indenter on a METTLER PM 34-K DeltaRange scale, to be sure of both the weight desired and because this information will be useful to in the calculations (Figure 3.16). At this point, everything was installed in place of the Charpy pendulum, and the corresponding specimen was inserted inside the vise, which by design already has a notch, corresponding to the engraving of the name. The specimen should protrude half its length from the jaws. Once the angle at which the specimen is supposed to break was set, the inventor was dropped, like is shows in Figure 3.17. The angle corresponding to the non-breaking of the specimen was found by trial and error. This, considering that the arm, from its fulcrum to the inventor's impact radius is equal to 230 mm, was used to calculate the useful radius, as seen in equation 3.8. By being careful to enter the units of measurement of the international system, the energy absorbed, and the Izod Impact strength are calculated, equation 3.9. The values taken for each scenario were averaged and entered in the table found in chapter 4.

$$Specimen\ section\ A = 4 \cdot 10 = 40\ mm^2 = 0,00004\ m^2 \tag{3.7}$$

$$Useful\ Radius\ R_u = 230 \cdot sen(\alpha) \tag{3.8}$$

$$Izod\ impact\ strength = \frac{Absorbed\ Energy}{Specimen\ section} = \frac{R_u \cdot g \cdot m}{A} = \left(\frac{KJ}{m^2}\right) \tag{3.9}$$

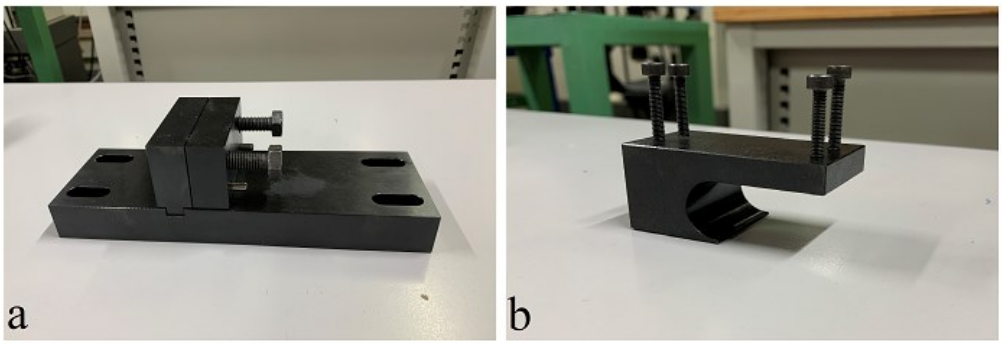

Figure 3.15: a) Base and vise, b) indenter to perform the Izod Impact Strength test

Figure 3.16: Inventor weight measured on a METTLER PM 34-K DeltaRange scale

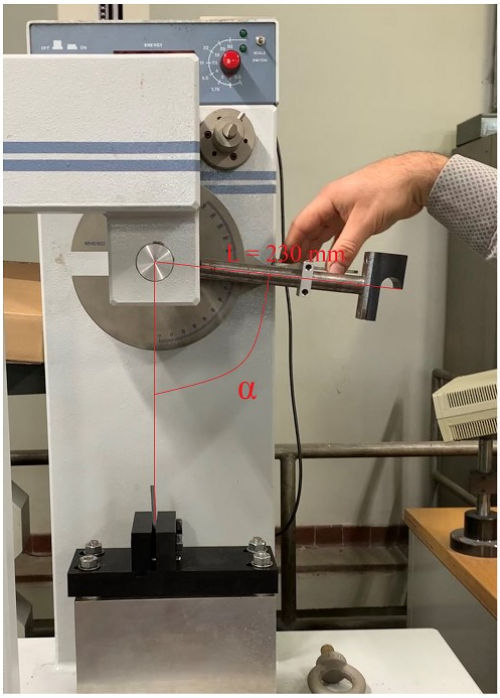

Figure 3.17: Instron CEAST pendulum readjusted with a designed base and indenter to perform the Izod Impact Strength test, located within the DIMEAS department of the Polytechnic of Turin, Italy

3.3.4 Microindentation Hardness testing

To examine small-scale changes in hardness, whether deliberate or unintentional, microindentation hardness testing is frequently performed. It is used to examine homogeneity, assess decarburization, assess the efficacy of surface hardening treatments, and assess the hardness of specimens that are too small for conventional bulk indentation testing. The Vickers and Knoop tests are the two most popular microindentation tests, they differ in the type of indenter used. The Vickers test presses the indenter into the test component by applying a steady, impact-free stress. Ten seconds are spent holding the indenter in place. In order to obtain accurate results, the indenter's physical quality and the applied load's precision must be under control. Following the removal of the load, the two impression diagonals are averaged and measured using a filar micrometer, often to the nearest 0,1 μm. The formula described in the literature is used to determine the Vickers hardness (HV).

The Microindentation Hardness testing is carried out using the Rupac Innovatest microindenter, located within the DIMEAS department of the Polytechnic of Turin, Italy. A load equal to 1 Kgf, the most suitable for this type of specimens, is set by means of a Vickers type indenter, and the 10x microscope lens is used to visualize the groove made.

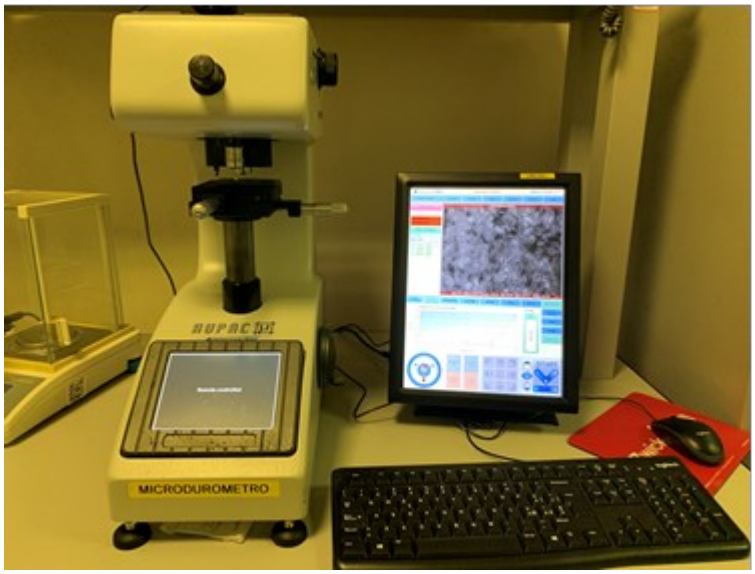

Figure 3.18: Rupac Innovatest microindenter, located within the DIMEAS department of the Polytechnic of Turin, Italy

Once the specimen is positioned on the plate, which can be translated vertically through a knob positioned on the side, the machine applies the load through the previously set indenter (Figure 3.19). Through the microscope, the software reproduces the image of the surface in real time on the screen. When the operator sees the imprint left by the indenter, the machine captures the image. The vertices of the footprint are manually determined and then the software calculates its size and the corresponding HV/1 hardness value. Three values are measured for each specimen in different parts of the surface, an arithmetic average is made and noted in the corresponding table in Chapter 4. The values are taken only on the less rough surface mentioned in the two chapters previous, or rather, the surface corresponding to the first printed layers of each specimen. The reason is that it is not visually possible to identify the grooves made by the indenter on the most wrinkled part. As the readers can see in Figure 3.20, the surface is not very homogeneous in order to obtain an adequate result for this test.

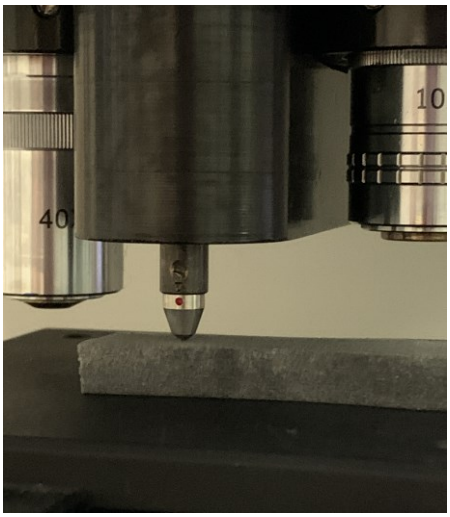

Figure 3.19: Pressure of the Vickers type indenter on a PA12 specimen printed for MJF for the measurement of the Microindentation Hardness

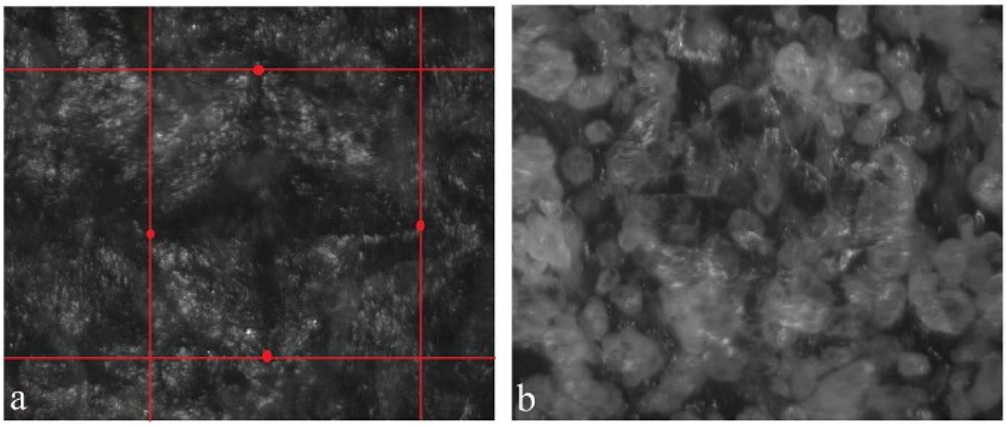

Figure 3.20: Images collected by the Rupac Innovatest microindenter, a) surface with less roughness b) surface with greater roughness

3.3.5 Shore Hardness testing

Shore hardness testers are non-destructive testing tools employed to determine the material's hardness, usually for rubbers, elastomers, and polymers, especially Shore D. The operator applies a specific force to a presser foot that is standardized, and the durometer measures the depth of the indentation in the material that is caused. This depth is influenced by the material's hardness, viscoelastic characteristics, presser foot design, and test duration. Higher numbers on the scale denote tougher materials with better indentation resistance. Less resistance and softer materials are indicated by lower values.

The Shore Hardness testing is carried out using the Shore Durometer HBD 100-0 SAUTER GmbH, located within the DIMEAS department of the Polytechnic of Turin, Italy.

Figure 3.21: Shore Durometer HBD 100-0 SAUTER GmbH, located within the DIMEAS department of the Polytechnic of Turin, Italy

Taking care to apply the same force consistently on all the specimens, the operator measures the hardness by reading the graduated bar. For each scenario, the hardness of 3 specimens is evaluated. Each of these is measured several times and the arithmetic average of the values taken is made. This research wants to underline the difference that can be found between the hardness of the rougher surface, that is the one that corresponds to the last printed layer, compared to the less rough one. The mean has been reported with its standard deviation in the bar graphs in Chapter 4.

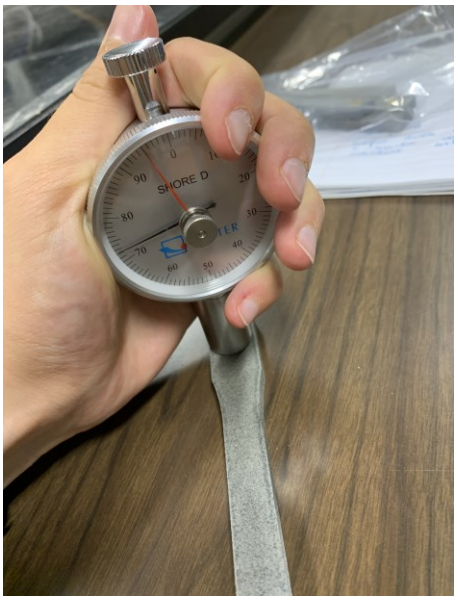

Figure 3.20: Shore Hardness testing on PA12 specimen printed with MJF technology

4. Results

In this chapter, readers can find all the results of all the tests conducted, divided by each scenario, and the specific conclusions to which each test led.

4.1 Chemical Characterization

4.1.1 FTIR-ATR

4.1.1.1 Scenario α) Dependence of the samples position inside the printed JOB;

Figure 4.1 shows the FTIR-ATR spectrum obtained from the specimens not aged, this is identical for all the three positions inside of the work area, in which they were printed. For each peak, within the Wavenumbers-Absorbance graph, it was researched in the literature for its meaning and reported in table 4.1. In the literature there are gods range of wavenumbers which, compared to those found through our test, confirm the fact that this study is dealing with the molecule of PA12 described in the first chapter and that not other links come into play. Reported in the graph, we can highlight the peaks concerning the NH bond stretch, CH_2 vibration, Amide I C=O stretch, Amide II and CH_2. Above 1500 cm^{-1} bands can be attributed to specific functional groups, while below this value the spectrum is complex lo evaluated it.

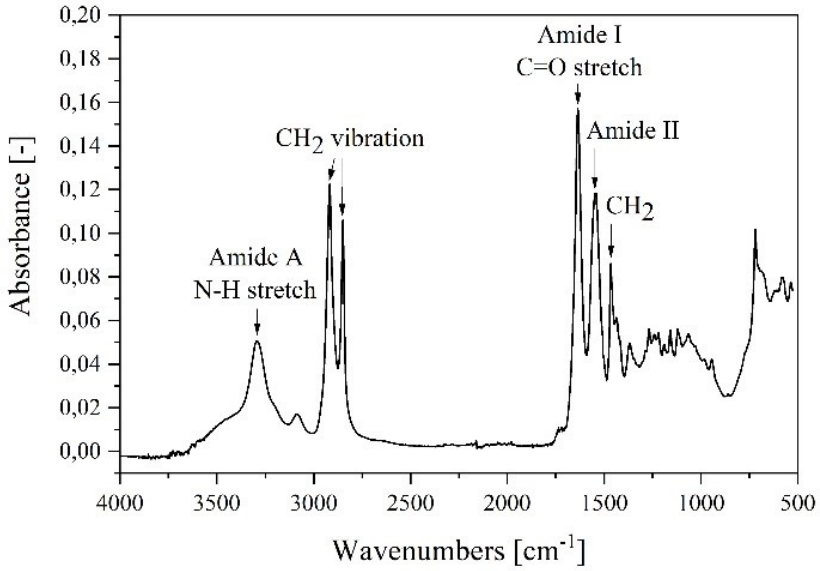

Figure 4.1: FTIR-ATR spectrum for scenario α

Table 4.1: FTIR-ATR spectrum peaks of PA12 printed in comparison with standard PA12 data

FTIR peaks [cm^{-1}]	Standard PA12 FTIR peaks [cm^{-1}]	Peak assignments
3293	3320 (α-form) 3310 (γ-form)	Hydrogen-bonded N−H stretching
3086	3080 (α-form) 3090 (γ-form)	Fermi-resonance of N–H stretching, with an overtone Amide II
2917	2930 (α-form) 2930 (γ-form)	CH_2 asymmetric stretching
2849	2860 (α-form)	CH_2 symmetric stretching

	2860 (γ-form)	
1636	1635 (α-form) 1640 (γ-form)	Amide I, C=O stretching
1545	1540 (α-form) 1563 (γ-form)	Amide II, C–N stretching + C=O in-plane bending
1466	1470 (α-form) 1466 (γ-form)	N-vic. CH_2 bend
1369	1370 (α-form) 1368 (γ-form)	CH bend, CH_2 twisting
1268	1272 (α-form) 1268 (γ-form)	Amide III (C–N stretching + C=O in-plane bending)
1159	1160 (α-form) 1160 (γ-form)	Skeletal motion involving CONH
1120	1120 (α-form) 1122 (γ-form)	C−C stretching
945	936 (α-form) 946 (γ-form)	CONH in plane
719	720 (α-form) 721 (γ-form)	CH_2 rocking
622	627 (γ-form)	Amide VI, N–H out-of-plane bending
577	578 (α-form)	Amide VI, N–H out-of-plane bending

4.1.1.2 Scenario β) Influence of the samples orientation inside the printed JOB (XY or Z);

In Figure 4.2 it is shown the graph taken for the specimens in Z direction. It is the same as Figure 4.1, there are no variations of functional groups.

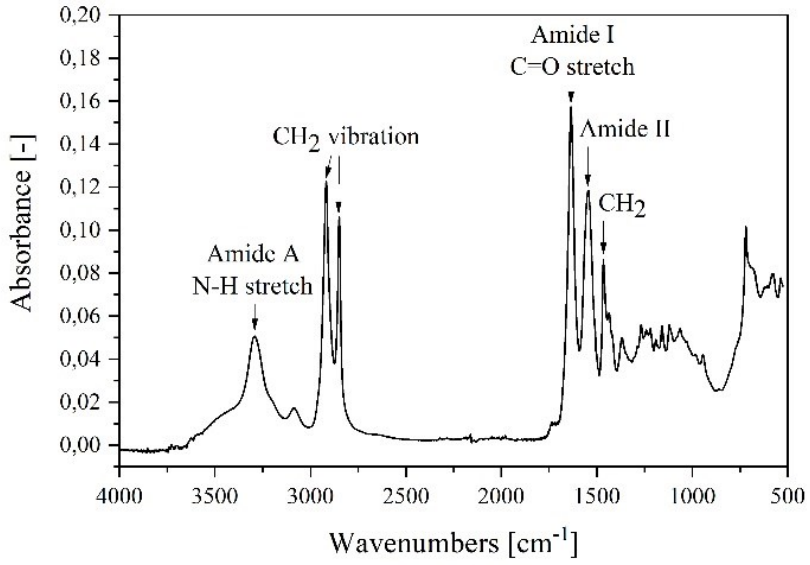

Figure 4.2: FTIR-ATR spectrum for scenario β

4.1.1.3 Scenario γ) Effect of the aging over printed samples for 3-time steps (no aged, ⅓ aged, fully aged);

Figure 4.3 shows the spectrum taken from the specimens that have undergone a third of the aging, compared to the spectrum taken for the unaged specimens. The readers can notice a difference in Absorbance, but the Wavenumbers are identical.

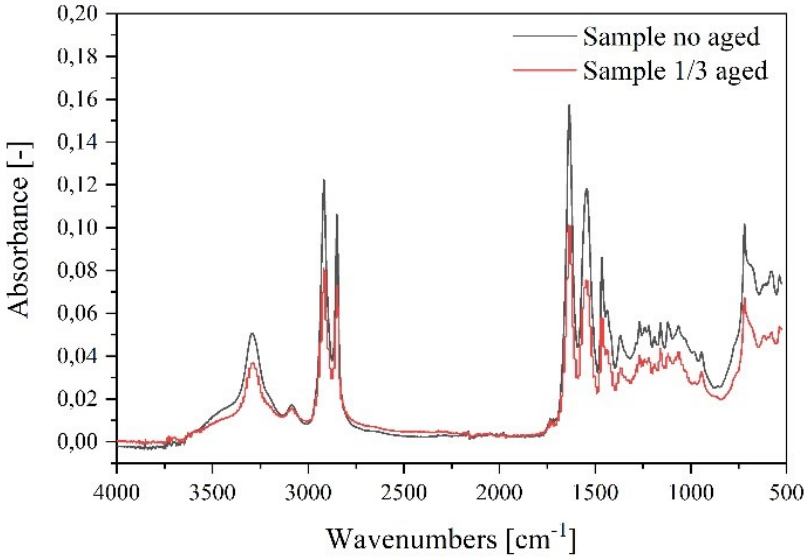

Figure 4.3: Comparison between FTIR-ATR spectrum of no aged PA12 sample with the same one aged in a climatic chamber for 240h

4.1.1.4 Conclusions

With this test it is possible to identify the PA12 molecule clearly by the corresponding functional groups. Furthermore, this research concludes that there are no variations in the macromolecule and therefore in its vibrations, if the specimens are printed in different directions or in different positions in the working area, or if they have undergone different stages of accelerated aging, through the test in high Humidity and Temperature of different duration.

4.2 Thermal Characterization

4.2.1 DSC

4.2.1.1 Scenario α) Dependence of the samples position inside the printed JOB;

As described in Chapter 3, for the DSC, the splinters taken from each specimen whose weight and the values, reported in Table 4.2, are set in the Software available. Graph 4.4 describes the performance of the Heat Flow as a function of Temperature, of the unaged and printed specimen in position A and direction XY. The minimum, or rather, the melting temperature, is positioned at 183 °C, while the inflected corresponding to the glass transition temperature is 48.4 °C. Enlarging the graph, this second temperature can be clearly seen. As specified in the graphs, the upper part relates to exothermic reactions, while the lower part relates to endothermic ones, like fusion. Subsequently, through the Origin software, it is calculated the area below the melting curve, corresponding to the percentage of crystallinity, if the equation described in chapter 3 is followed. For this specimen a crystallinity percentage of 37.51%. Graph 4.5, on the other hand, corresponds to the unaged specimen printed in position B and direction XY, also from this the readers can get the same information, or rather, a melting temperature of 184°C, a transition temperature of 48°C and a percentage of crystallinity of

40.09%. Lastly, the specimen in position C with a melting temperature of 180°C, glass transition of 47.3 °C and a crystallinity of 35.71%. All values have been reported in table 4.3. Being the glass transition temperature identified by a range, it can be said that, based on the moulding position, this temperature does not vary. The same thing was found for the melting temperature. Instead, variation was found on the percentage of crystallinity, it is greater for the specimens printed in direction B, 4,38% compared to the specimens in direction C, and almost 3% compared to specimens in direction A, due to the different type of cooling they have undergone after printing. The specimens in fact printed in points A and C are similar, as the positions are symmetrical about the center, lower and upper vertices.

Table 4.2: Weight of the specimens' splinter for scenario α

Time step	Printing orientation	Weight [mg]
No aged	AXY-11	10,8
No aged	BXY-11	9,6
No aged	CXY-11	10,5

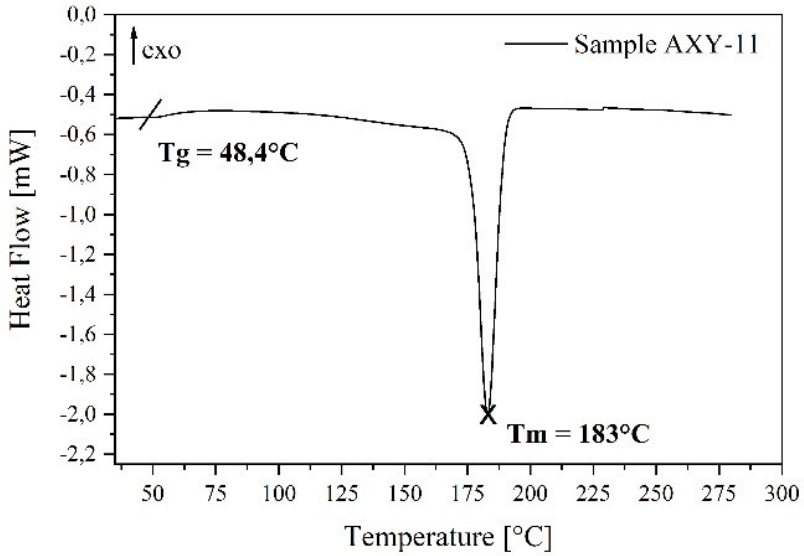

Figure 4.4: DSC curve for the specimen unaged printed in position A and direction XY

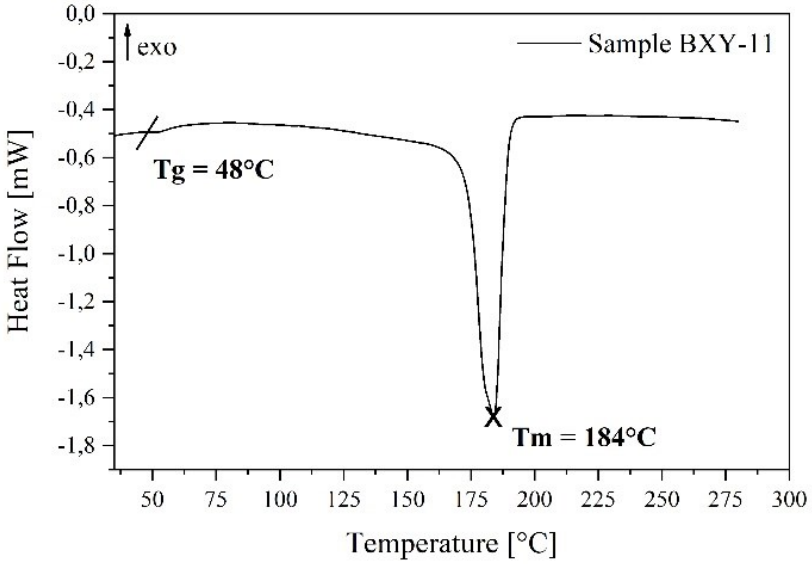

Figure 4.5: DSC curve for the specimen unaged printed in position B and direction XY

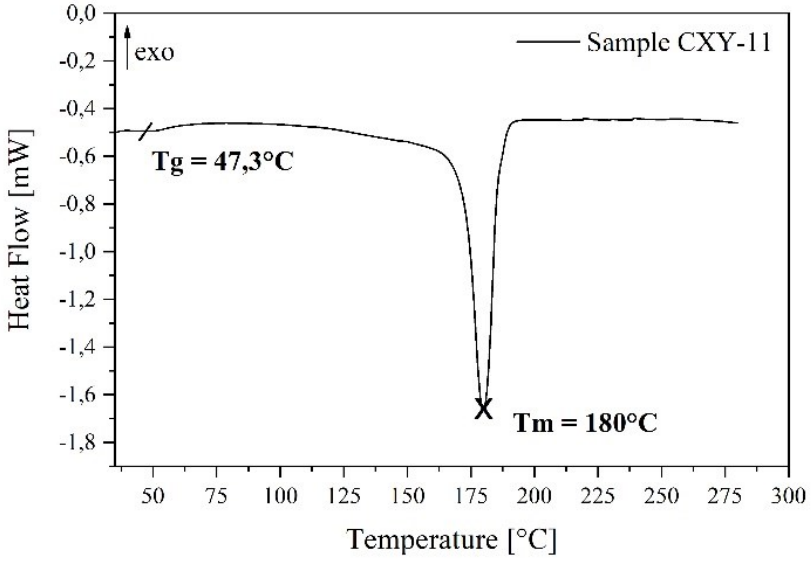

Figure 4.6: DSC curve for the specimen unaged printed in position C and direction XY

Table 4.3: Glass transition temperature, melting temperature and percentage of crystallinity for the scenario α

Time step	Printing orientation	Tg [°C]	Tm [°C]	Cristallinity [%]
No aged	AXY-11	48,4	183	37,51
No aged	BXY-11	48	184	40,09
No aged	CXY-11	47,3	180	35,71

4.2.1.2 Scenario β) Influence of the samples orientation inside the printed JOB (XY or Z);

The same procedure is performed on the printed specimen in position A but direction Z whose information is reported, in comparison with the specimen in XY direction and same position, within table 4.5. It is noted that the glass transition temperatures are equal and there is a negligible deviation from the melting temperature. The percentage of crystallinity decreases if the PA12 is printed in the Z direction, also in this case due to cooling, which is not homogeneous for the latter, as explained in chapter 3.

Table 4.4: Weight of the specimens' splinter for scenario β

Time step	Printing orientation	Weight [mg]
No aged	AZ-11	10,1

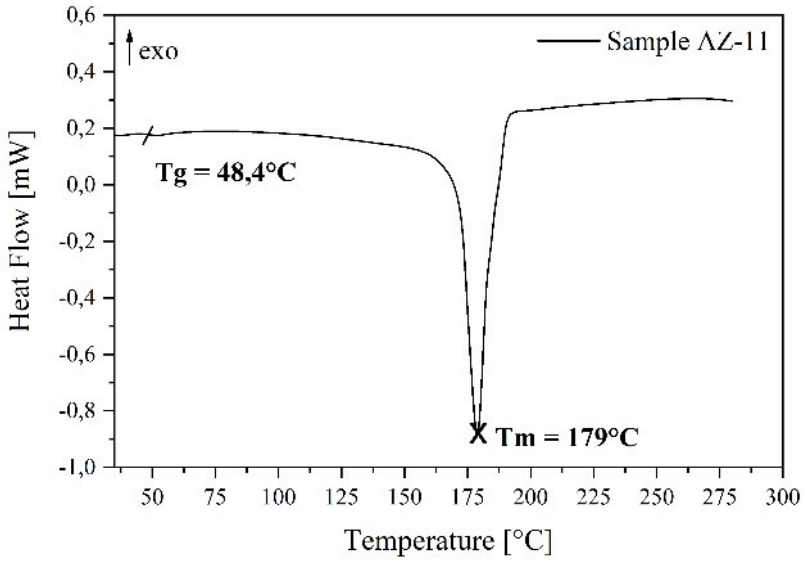

Figure 4.7: DSC curve for the specimen unaged printed in position B and direction Z

Table 4.5: Glass transition temperature, melting temperature and percentage of crystallinity for the scenario β

Time step	Printing orientation	Tg [°C]	Tm [°C]	Cristallinity [%]
No aged	AXY-11	48,4	183	37,51
No aged	AZ-11	48,4	179	34,79

4.2.1.3 Scenario γ) Effect of the aging over printed samples for 3-time steps (no aged, ⅓ aged, fully aged);

Once the specimens have undergone several stages of accelerated aging through a high temperature and high humidity test, they are allowed to cool to room temperature, placing them inside a watertight bag. Subsequently, the splinters were collected (weight values in Table 4.6) and tested inside the DSC equipment, which describes their Heat Flow as a

function of Temperature. For both stages of aging the temperature of casting did not vary compared to the unaged specimen, while a strange effect appeared a medium temperature. Enlarging the graphs of these two tests in a range that goes from 40 °C to 150°C, two well-defined inflections can be seen, around 46 °C and 95 °C, for BXY-27 and at 110 °C for BXY-44. The crystallinity, on the other hand, is lowered by 3% for the specimens at a third of the total aging total, while it rises by almost 2% for those with total aging.

Table 4.6: Weight of the specimens' splinter for scenario γ

Time step	Printing orientation	Weight [mg]
1/3 aged	BXY-27	10,8
Fully aged	BXY-44	10,0

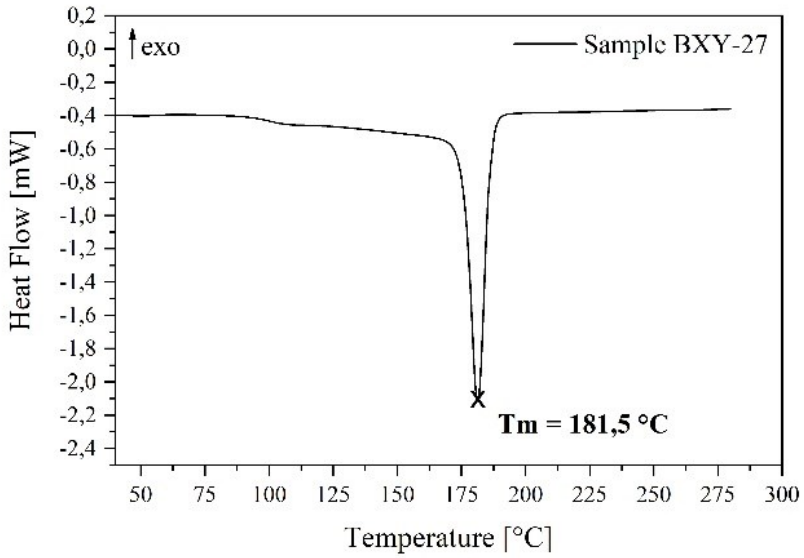

Figure 4.8: DSC curve for the specimen 1/3 aged printed in position B and direction XY

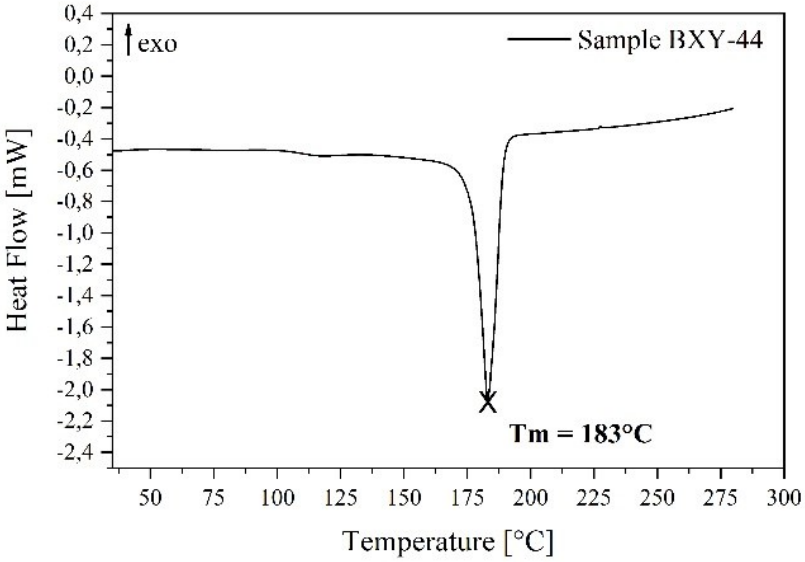

Figure 4.9: DSC curve for the specimen fully aged printed in position B and direction XY

Table 4.7: Glass transition temperature, melting temperature and percentage of crystallinity for the scenario γ

Time step	Printing orientation	Tm [°C]	Cristallinity [%]
No aged	BXY-11	184	40,09
1/3 aged	BXY-27	181,5	37,18
Fully aged	BXY-44	183	41,80

4.2.1.4 Conclusions

For all the scenarios debate, there are no changes in the melting Temperature, which has a value included in the range 179 - 184 °C, corresponding to the previous studies available in literature. There are not in these curves two melting peaks, as happens in some papers, so the germs of the spherulites have the same melting temperature. Higher percentages of crystallinity are evaluated for the specimens printed in position B, due to the different cooling time that these have undergone, being enclosed within the powder in the printing JOB. With aging, these specimens have decreased their percentage of crystallinity of 3% and then increase it by 5% at full aging, due to rearrangement of the crystalline and amorphous parts due to the temperature to which they have been subjected. The T_g, on the other hand, remains constant for all unaged specimens, while it cannot be defined with certainty for those subjected to high temperature and humidity. However reasonably, based on the others information obtained, it is supposed to remain unchanged around 46 °C. There is not enough information to give a certain and truthful meaning about the inflection that appears around 100 °C, it can however be seen that this is close to the temperature of boiling water, it is possible suppose the effect of humidity. Due to the scarcity of texts present in literature, that address this type of test, combination of temperature and humidity, for polyamides, it is important to continue the study to chemically understand what the interactions are at stake and define the veracity of this with respect to aging over time.

4.3 Mechanical Characterization

4.3.1 Tensile testing

4.3.1.1 Scenario α) Dependence of the samples position inside the printed JOB;

In the following subchapter can be found, for each position in the working area, two graphs, a Load-Stroke and the corresponding Stress-Strain calculated through the equations described in detail in Chapter 3. Graph 4.11 shows how the specimens in printing position A have an evident plastic trend that results in a ductile fracture, as seen in Figure 4.12. In this, the report attached to Figure 4.13 shows some cavities of variable length on average of about 0.50 mm, corresponding to the necking section. The results obtained through the equations described in Chapter 3 can be found in Table 4.8. The fall that the readers see in these graphs corresponds to the position at which it deviated voluntarily the external extensometer from the specimen to which it was connected.

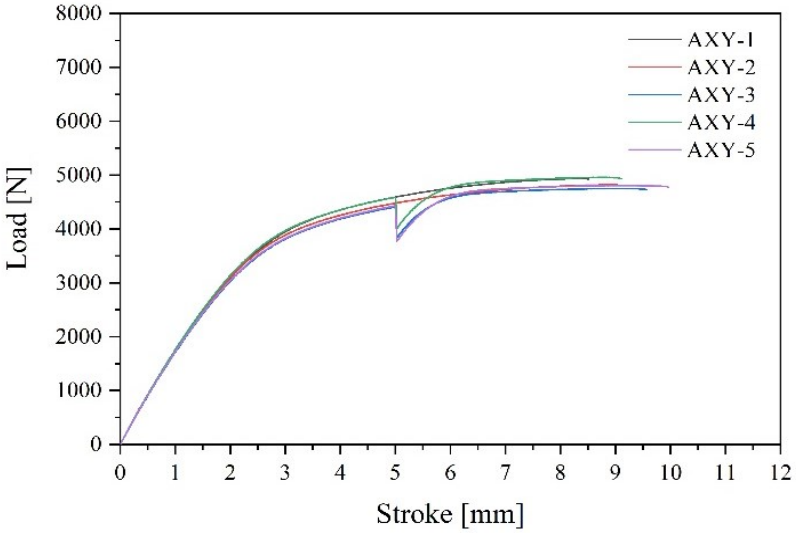

Figure 4.10: Load-Stroke curve for tensile testing perform on the specimen unaged printed in position A and direction XY

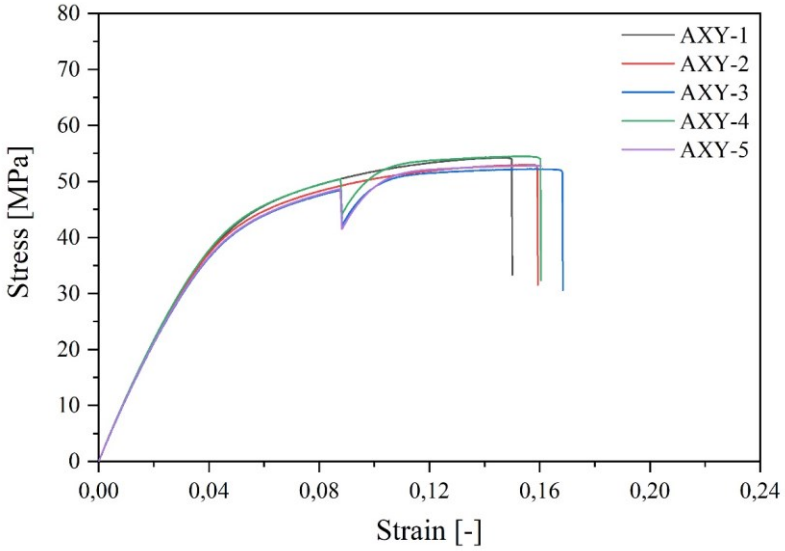

Figure 4.11: Stress-Strain curve for tensile testing perform on the specimen unaged printed in position A and direction XY

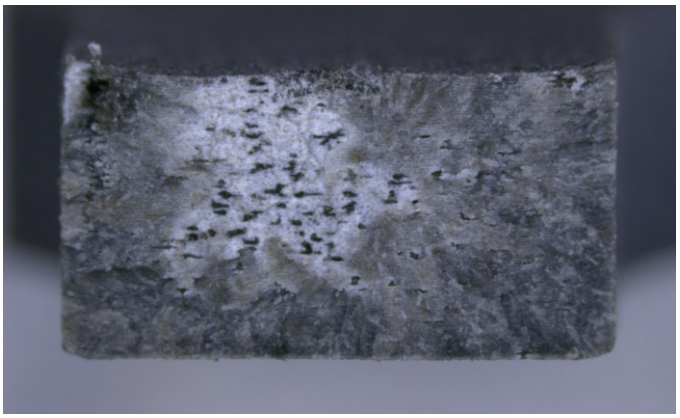

Figure 4.12: Breaking section of an unaged specimen in position A and direction XY

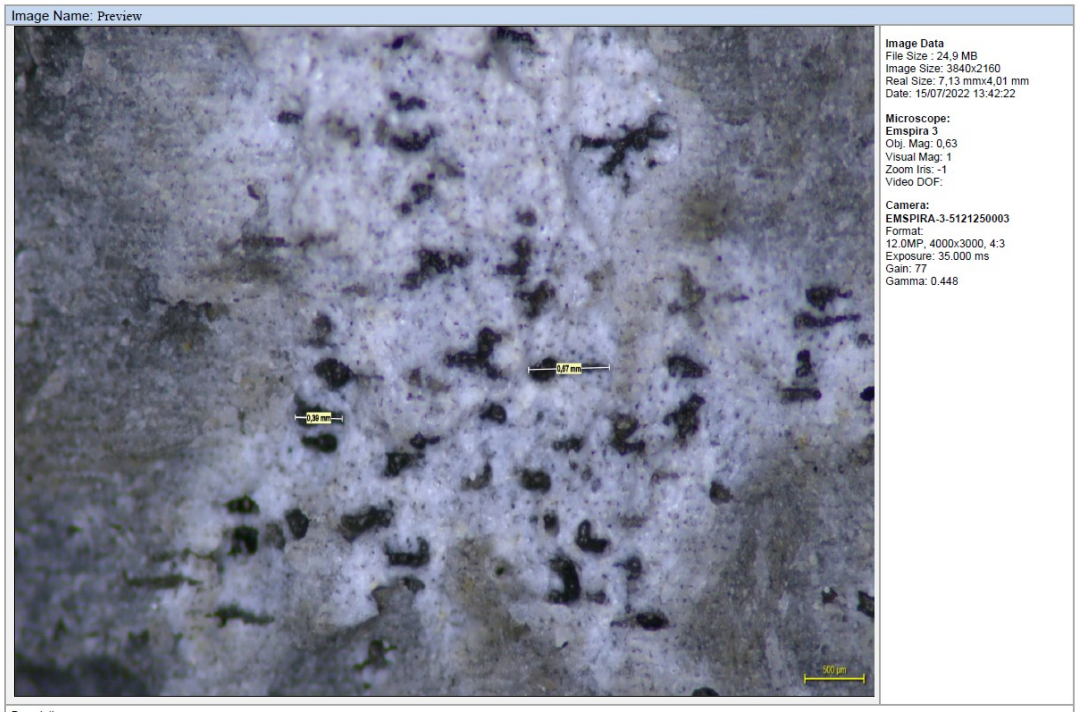

Figure 4.13: Report of the breaking section of an unaged specimen in position A and direction XY

At first sight, from the graphs showing the tensile results of the samples printed in position B, it is visible how these curves are scattered, leading to higher standard deviation. In this case one of the specimens tested suffered brittle fracture, due to a printing defect, as the readers can see in Figure 4.16 near the edges of the photographed breaking section under the microscope own by Valeo Santena.

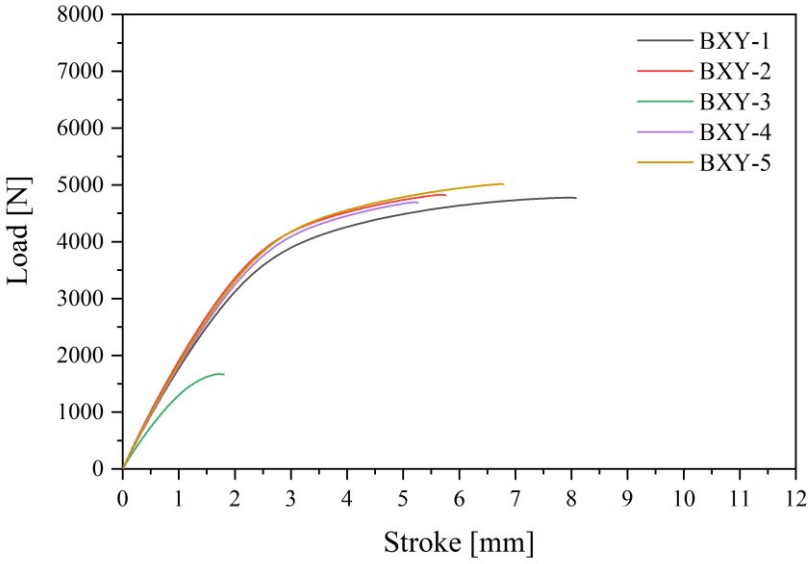

Figure 4.14: Load-Stroke curve for tensile testing perform on the specimen unaged printed in position B and direction XY

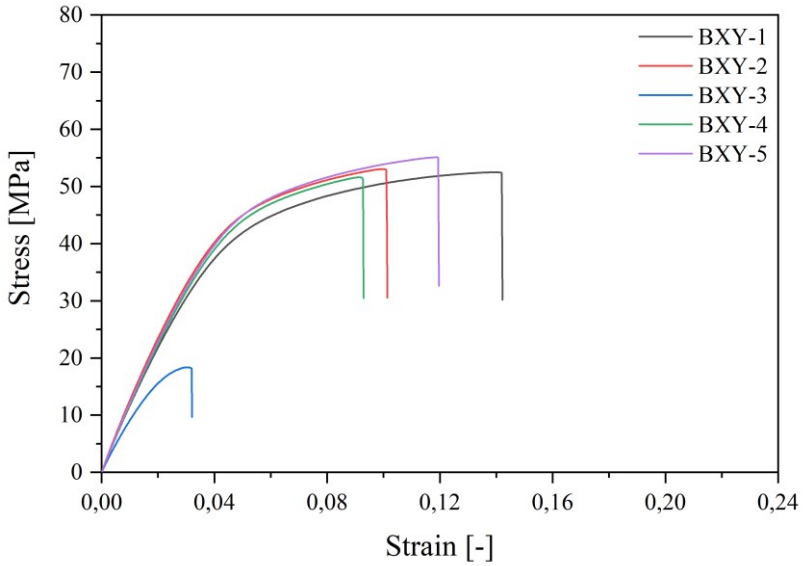

Figure 4.15: Stress-Strain curve for tensile testing perform on the specimen unaged printed in position B and direction XY

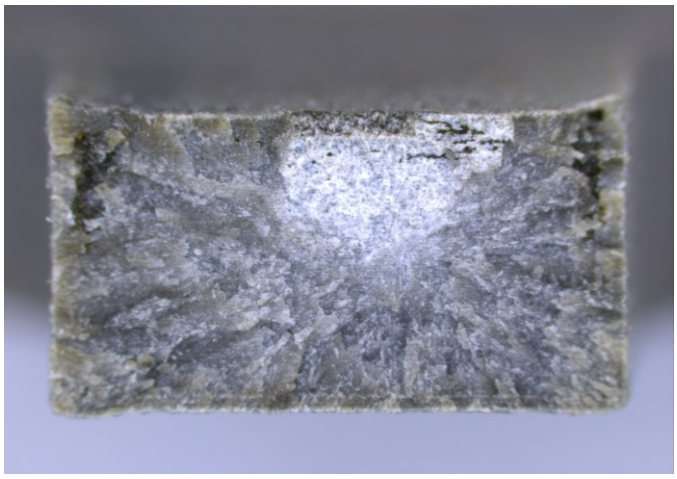

Figure 4.16: Breaking section of the unaged specimen BXY-3

The results corresponding to the specimens printed in position C are shown in Figure 4.17 and 4.18. A large plastic area is highlighted, like the photographed sections, confirm. The narrowed area is not perfectly in the center but close to the incision. The results extrapolated from the calculations are summarized in Table 4.8.

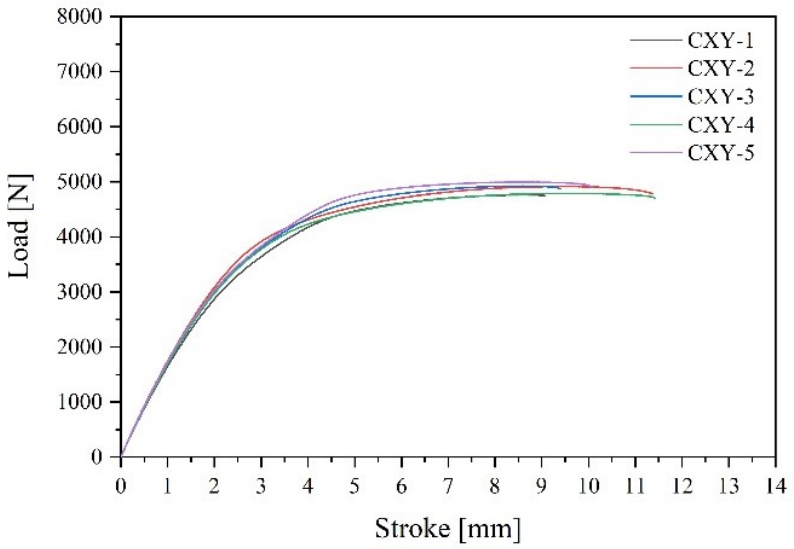

Figure 4.17: Load-Stroke curve for tensile testing perform on the specimen unaged printed in position C and direction XY

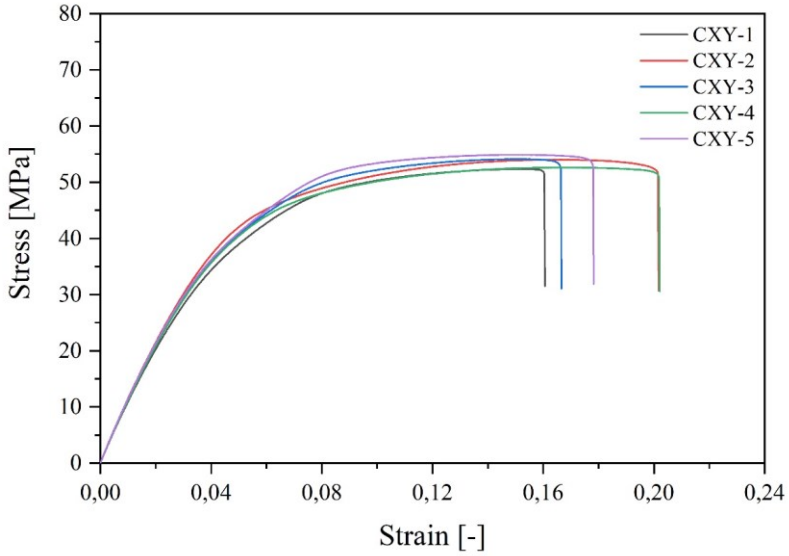

Figure 4.18: Stress-Strain curve for tensile testing perform on the specimen unaged printed in position C and direction XY

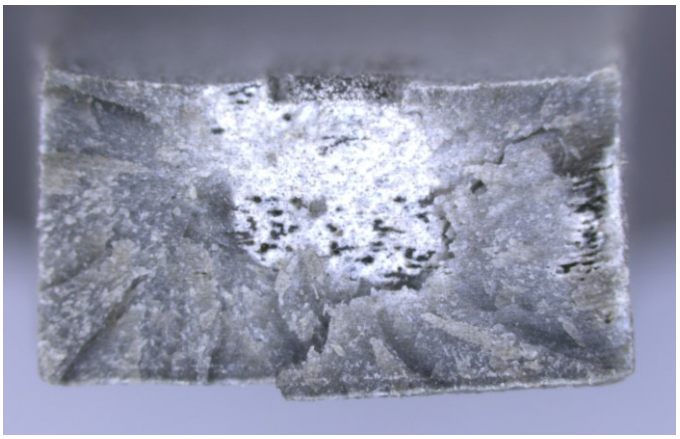

Figure 4.19: Breaking section of the unaged specimen CXY-2

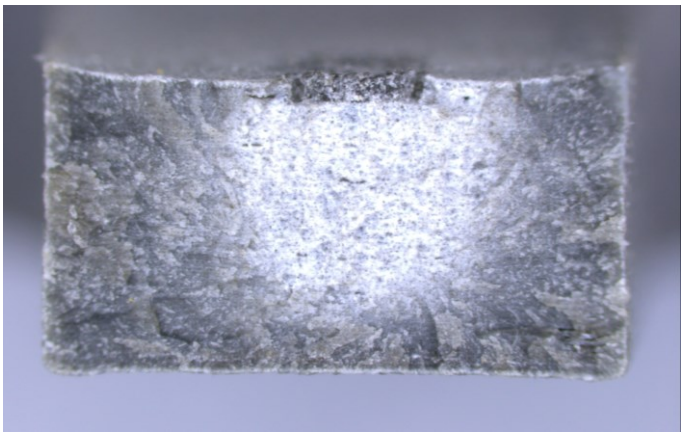

Figure 4.20: Breaking section of the unaged specimen CXY-3

Table 4.8 clearly shows the variations in mechanical properties between the areas of the JOB. The traction curves have an evident plastic trend. From the data the readers can notice a different elongation at break, for this scenario. Compared to position C, A has a smaller elongation, less than 15%, while greater for B 46%. This is also reflected in the slope of the elastic stretch, higher Young's modules for A and mostly for position B. The last one has a 11,6% decrease in the maximum stress it can withstand and an increase of 13% in its enervation. All the results obtained in position A and in position C, considering the standard deviation of each, are similar.

Table 4.8: Young modulus, 0,2% offset yield strength, ultimate tensile strength and elongation at break for the scenario α

Time step	Position into the JOB	Young modulus [MPa]	0,2% Offset yield strength [MPa]	Ultimate tensile strength [MPa]	Elongation at break [%]
No aged	AXY	996,12 ± 15,70	32,40 ± 1,36	53,34 ± 0,87	12,84 ± 0,67
No aged	BXY	1039,94 ± 26,32	35,71 ± 2,40	53,07 ± 1,28	8,06 ± 2,08
No aged	CXY	975,12 ± 18,77	31,01 ± 1,27	53,59 ± 0,97	15,10 ± 1,70

4.3.1.2 Scenario β) Influence of the samples orientation inside the printed JOB (XY or Z);

Figures 4.21 and 4.22 show the tensile test curves to which the AZ specimens were subjected. The curves deviate from each other, especially for the plastic zone. Their breaking section photographed and shown in Figure 4.23 does not show an obvious necking section like the samples printed in the same position, but in XY orientation. The fall that the readers see in these graphs corresponds to the position at which it deviated voluntarily the external extensometer from the specimen to which it was connected.

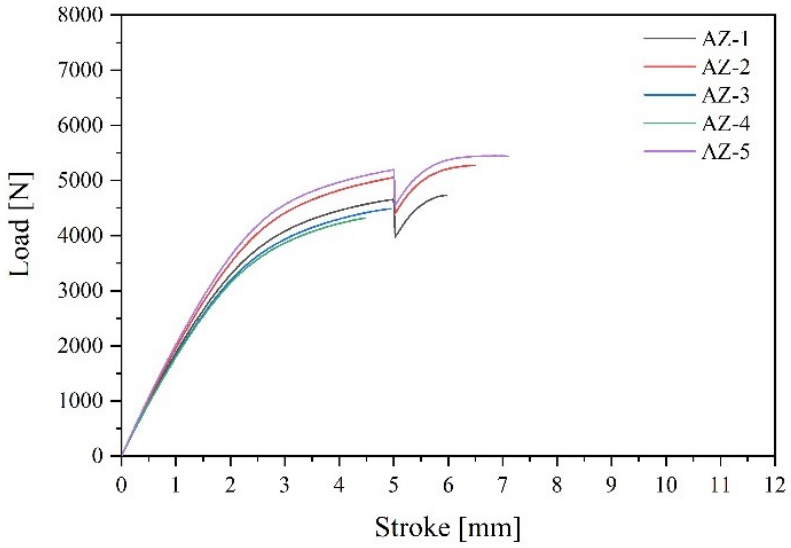

Figure 4.21: Load-Stroke curve for tensile testing perform on the specimen unaged printed in position A and direction Z

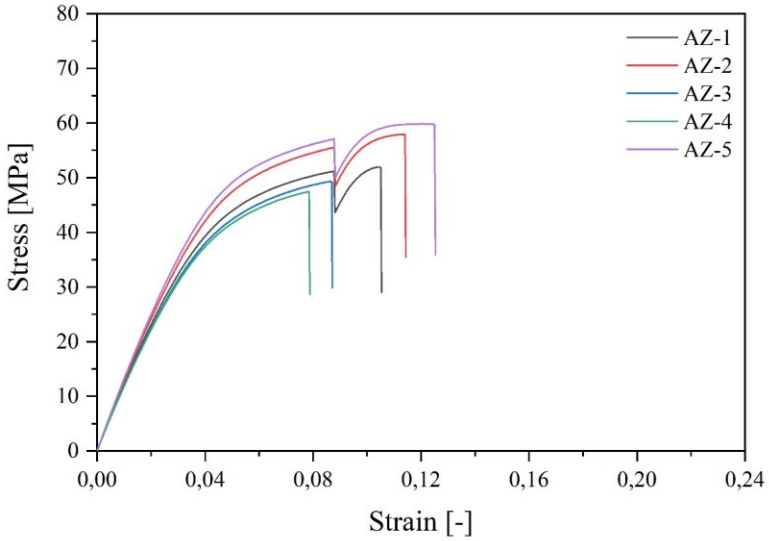

Figure 4.22: Load-Stroke curve for tensile testing perform on the specimen unaged printed in position A and direction Z

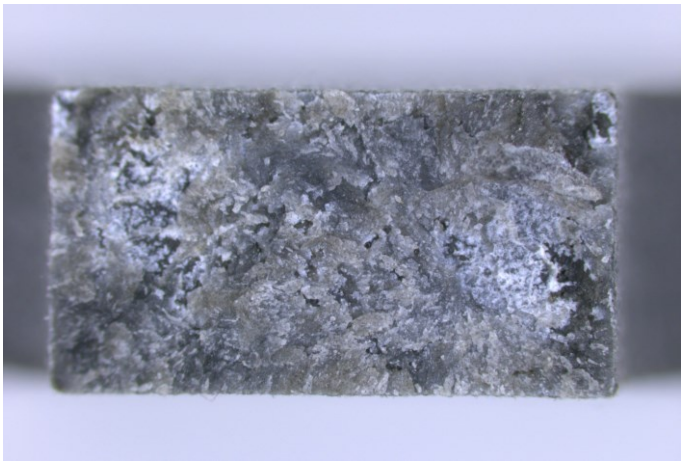

Figure 4.23: Breaking section of a unaged specimen printed in direction Z

A decrease in the plastic zone for the AZ specimens is evident, with a dispersion of the results, compared to those printed in the same position, but with a perpendicular orientation. In fact, the difference in elongation at break is 45%, it's much lower, that is justified by the orientation of the sections, function of the printing direction. In fact, during the tensile test, the creation of very evident signs of "tearing" can be seen on the edges of the specimen. Instead, Young's modulus is increasing by 9.6%. There is no obvious difference in Ultimate tensile Strength and is 8% for yield strength.

Table 4.9: Young modulus, 0,2% offset yield strength, ultimate tensile strength and elongation at break for the scenario β

Time step	Printing orientation	Young modulus [MPa]	0,2% Offset yield strength [MPa]	Ultimate tensile strength [MPa]	Elongation at break [%]
No aged	AXY	996,12 ± 15,70	32,40 ± 1,36	53,34 ± 0,87	12,84 ± 0,67
No aged	AZ	1102,15 ± 49,16	35,154 ± 3,98	53,27 ± 4,81	7,11 ± 1,52

4.3.1.3 Scenario γ) Effect of the aging over printed samples for 3-time steps (no aged, ⅓ aged, fully aged);

At first sight, observing the accelerated aged specimens, even after only 10 days, it is noticeable how the surfaces have become more homogeneous. Especially the rougher, corresponding to the last printed layers of each specimen, blackened and became less rough and similar to its opposite, as can be seen from Figure 4.24. Figures 4.25 and 4.26 show the results for the specimens printed in position B and XY direction, and kept at 85°C and 85% humidity. The plastic zone, or rather, the deviation from linearity, occurs at low values of Strain and is not very extensive, going to break with an average elongation of 6.17%. The embrittlement effect is more evident for the specimens subjected to the same temperatures and humidity for 700 h, where the curves have a mainly linear trend with a small plastic area. All this is confirmed by the photograph of the breaking section, Figure 4.29, which is presented lucid and without a necking area, that means a brittle break.

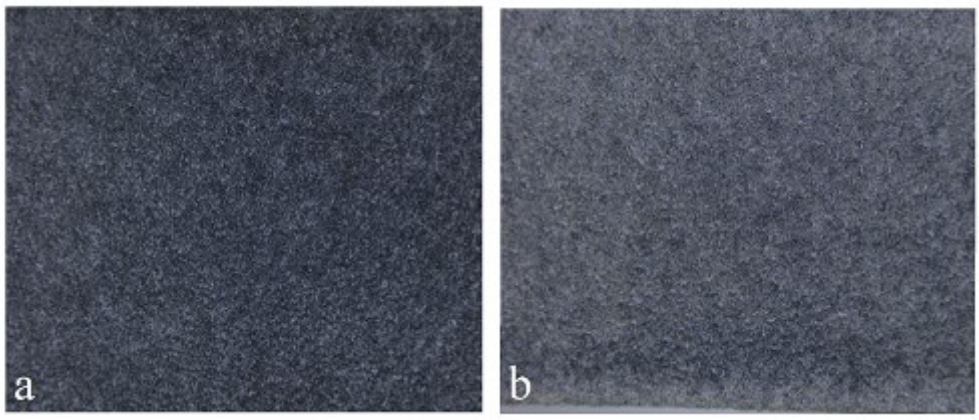

Figure 4.24: Microscope vision of the surfaces specimen after aging: a) less rough surface, b) rougher surface

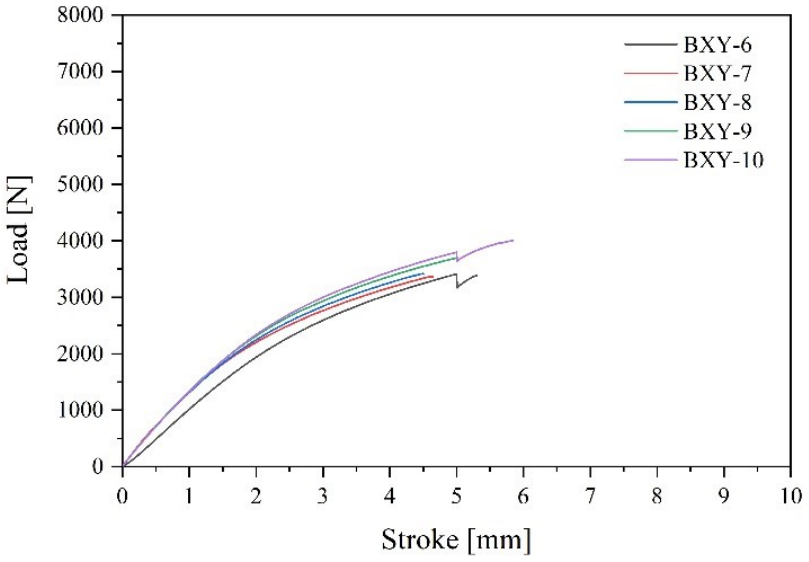

Figure 4.25: Load-Stroke curve for tensile testing perform on the specimen 1/3 aged printed in position B and direction XY

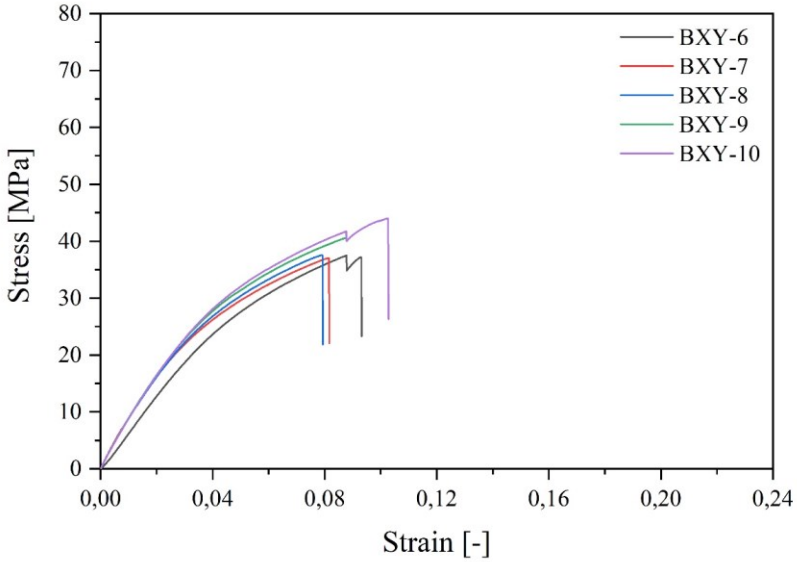

Figure 4.26: Stress-Strain curve for tensile testing perform on the specimen 1/3 aged printed in position B and direction XY

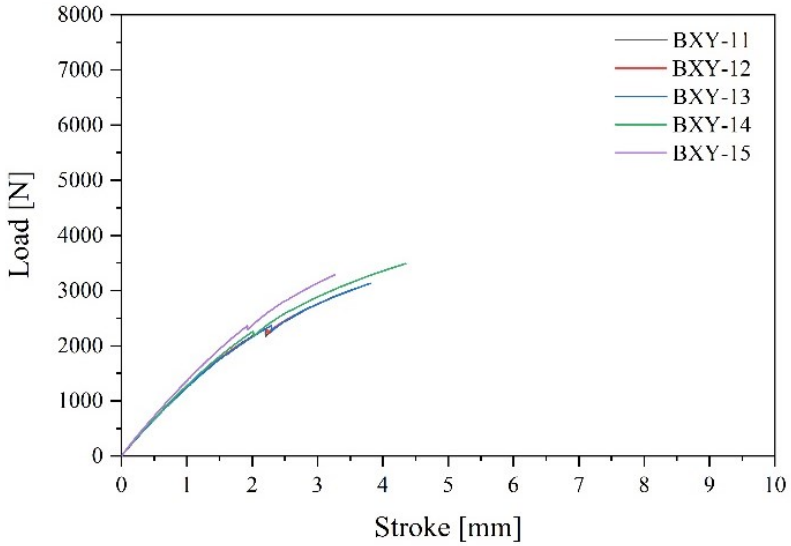

Figure 4.27: Load-Stroke curve for tensile testing perform on the specimen fully aged printed in position B and direction XY

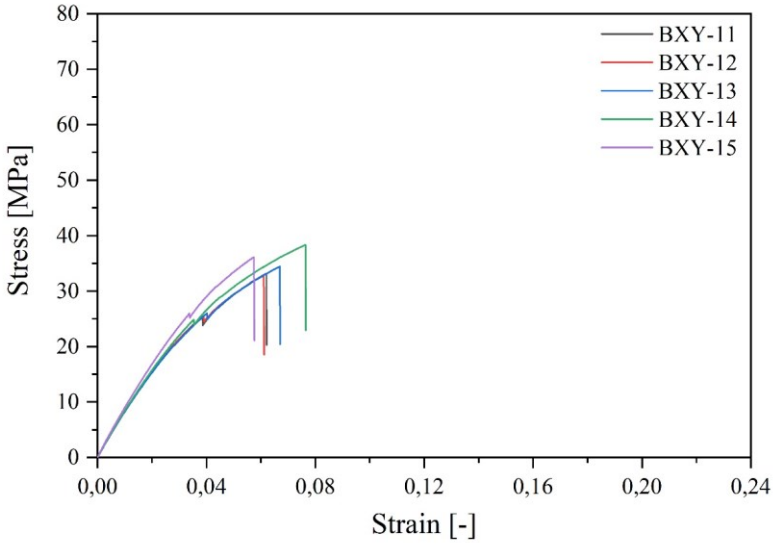

Figure 4.28: Stress-Strain curve for tensile testing perform on the specimen fully aged printed in position B and direction XY

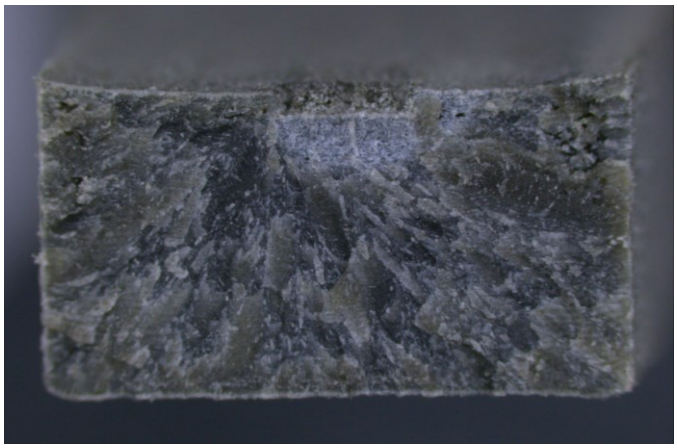

Figure 4.29: Breaking section of a fully aged specimen

With ageing, the specimens have lost, already at 1/3, plasticity (this area has become shorter and sloping), the trend is almost entirely linear, the material has become embrittled, all because in traction the tensile distribution is constant over the whole section. For the elongation at break a decrease of 23% at 1/3 and of 51% at total aging is notice. So the decline is almost linear for this property.

Table 4.10: Young modulus, 0,2% offset yield strength, ultimate tensile strength and elongation at break for the scenario γ

Time step	Position into the JOB	Young modulus [MPa]	0,2% Offset yield strength [MPa]	Ultimate tensile strength [MPa]	Elongation at break [%]
No aged	BXY	1039,94 ± 26,32	35,71 ± 2,40	53,07 ± 1,28	8,06 ± 2,08
1/3 aged	BXY	748,72 ± 62,94	21,14 ± 2,24	39,40 ± 2,63	6,17 ± 0,51
Fully aged	BXY	762,81 ± 29,18	20,20 ± 1,12	34,97 ± 2,06	3,97 ± 0,55

The graphs below, 4.30, 4.31, 4.32 and 4.33, show the decreasing trends of Young modulus, yield strength, tensile strength and elongation at break, during the aging stages. The first three, show an exponentially decreasing trend, while the elongation at break decreases linearly.

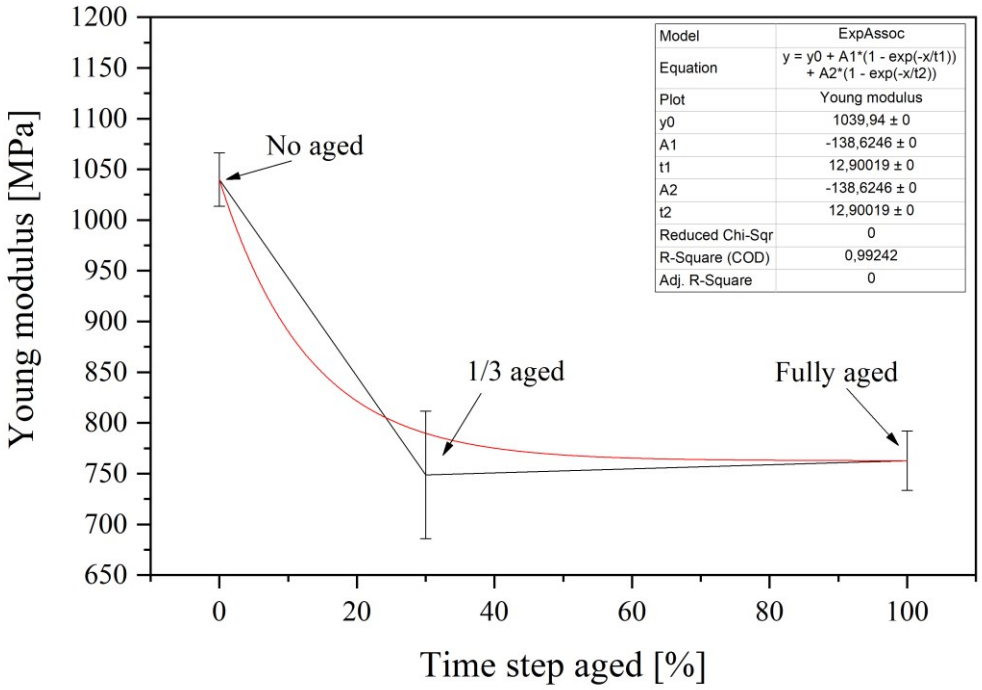

Figure 4.30: Young modulus aging trend

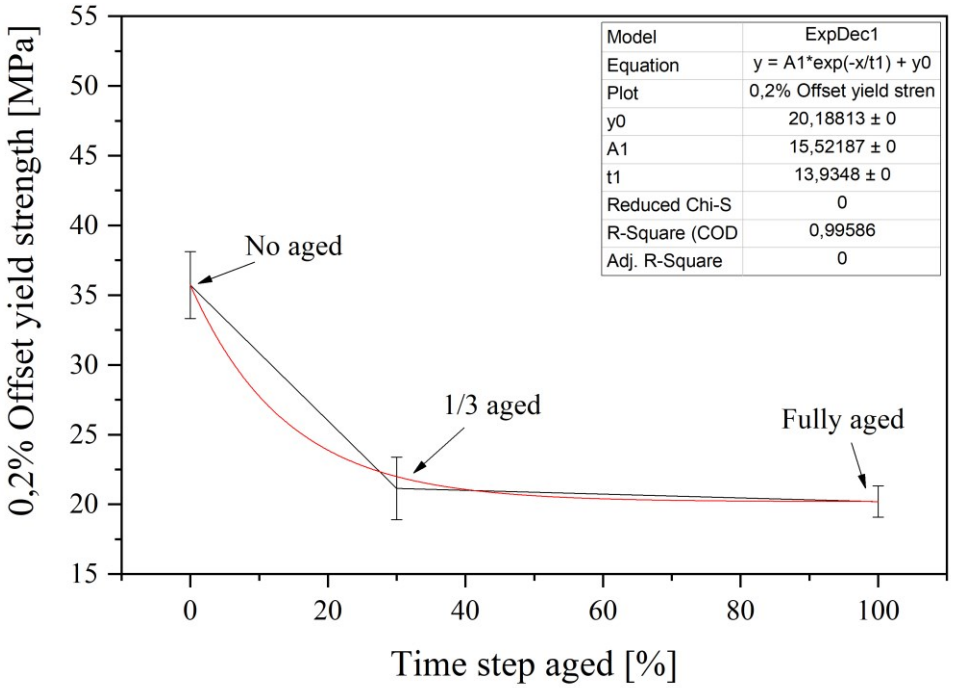

Figure 4.31: 0,2% Offset yield strength aging trend

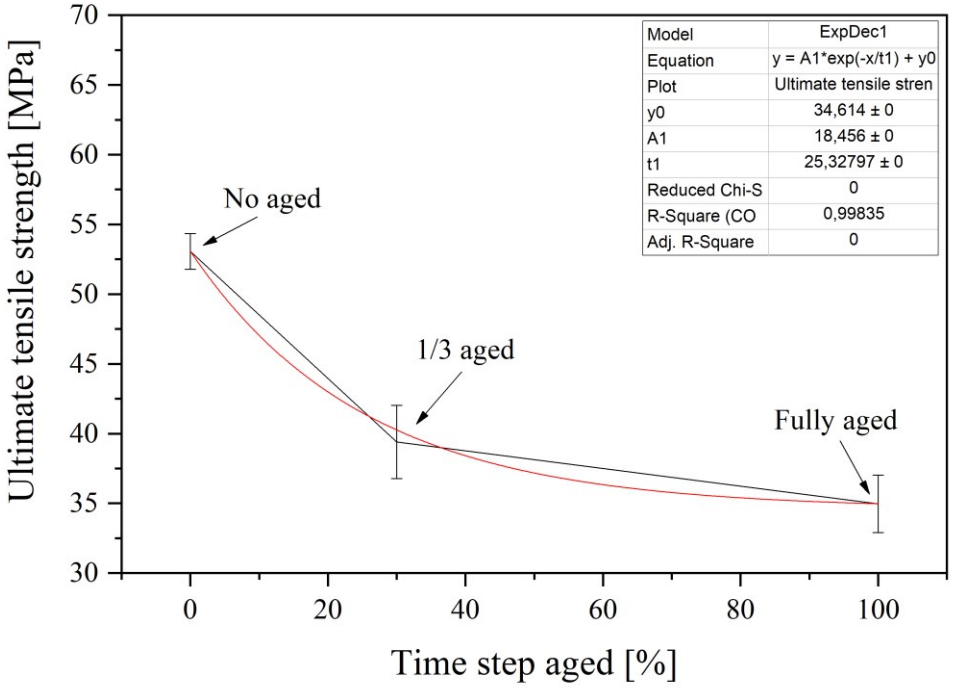

Figure 4.32: Ultimate tensile strength aging trend

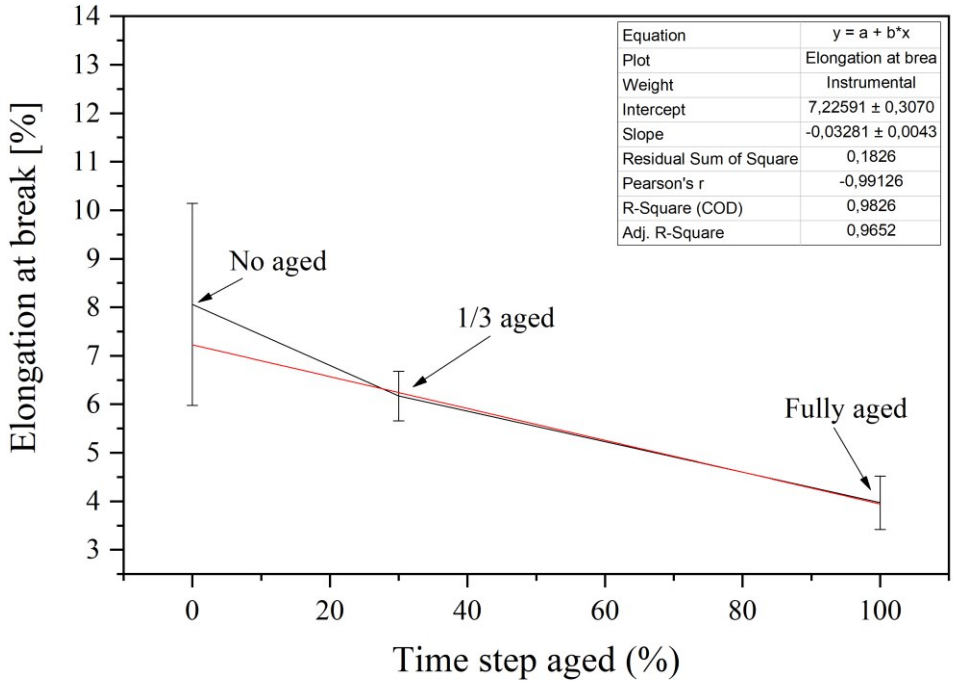

Figure 4.33: Elongation at break aging trend

4.3.1.4 Conclusions

With the tensile testing, ductile behaviors are highlighted for all the characterized areas of the JOB, with however some differences. Position B is the one that differs mostly from the others, especially from C, and has more dispersed results. It has greater stiffness, or rather, greater resistance to elastic deformation, as the elastic modulus is greater. It will experience less elastic deformation from the application of a given load. Thus, at the atomic level, smaller are the variations in the interatomic distance and the stretching of the interatomic bonds, this brings to greater interatomic bond strengths. The specimens in B therefore, have a transition from elastic to plastic behavior at a greater load, but lesser than in the other positions, it is the maximum stress that their structure can support if subjected to traction. Furthermore, the elongation at break is lower, therefore the lower is the ductility, the lower are the plastic deformation that these specimens can undergo without breaking. Therefore in B the behavior becomes more fragile but, as the yield point increases, at the static design level, the expected response should not differ much from that of the specimens in the other positions. To confirm this, it would be necessary to carry out fatigue tests on the components, this position could be the binding one as it has shorter durations.

In addition, with the tensile testing, it is found that the Z direction is the one that has the greatest stiffness, greater than the specimens in position B. They have a ductile behavior similar to these specimens, but the stress they can support is very similar to that one of the specimens in the same position but XY orientation. For these two scenarios the Young modules found are lower than those provided by HP, but are very similar to those found in the literature.

All the data seem to indicate that, with aging, the material loses mechanical properties and becomes more brittle. The specimens are less rigid, having a lower elastic modulus and therefore lower interatomic bonding forces. Furthermore, the specimens in this point pass with lower loads from elastic to plastic behavior and the lower the maximum stress they can sustain before breaking, the load limit is lowered. The stretch of plastic deformation tends to

disappear, with a low elongation at break, transforming the behavior from plastic to fragile. The degradation of the material appears already in the first third of the test, where it has a tendency to break abruptly at a low applied load.

4.3.2 3-Point Bending Flexural test

4.3.2.1 Scenario α) Dependence of the samples position inside the printed JOB;

In the following sub-chapter the readers can find, for each position in the working area, the graph corresponding to the Load-Stroke obtained through the 3-Point Bending Flexural test. For all three graphs, 4.34, 4.35 and 4.36, the plastic area is clearly distinguishable from the elastic one, these end with a 25 mm stroke since all the specimens did not face breaking, reaching the end of the machine stroke. The only exception is the BXY-7 specimen which, having a printing defect, face the break at 17 mm and with a maximum load of 121.05 N. It is not taken into consideration because it is not representative.

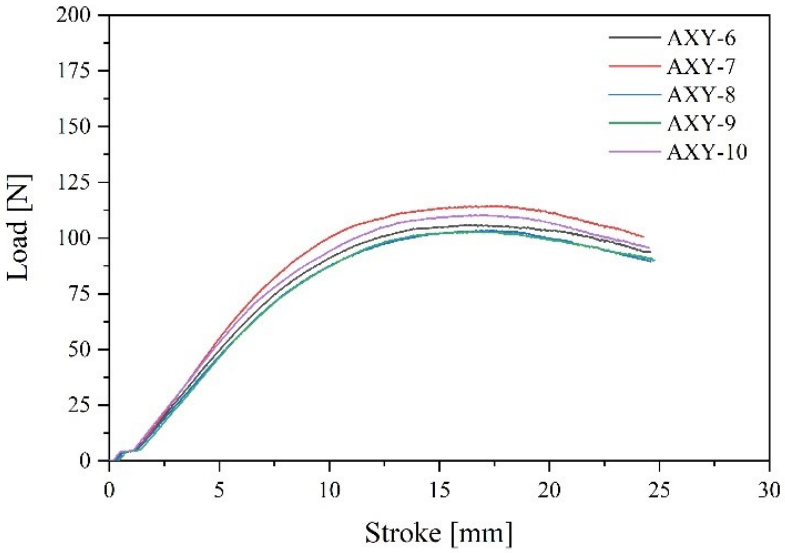

Figure 4.34: Load-Stroke curve for 3-point bending flexural test perform on the specimen unaged printed in position A and direction XY

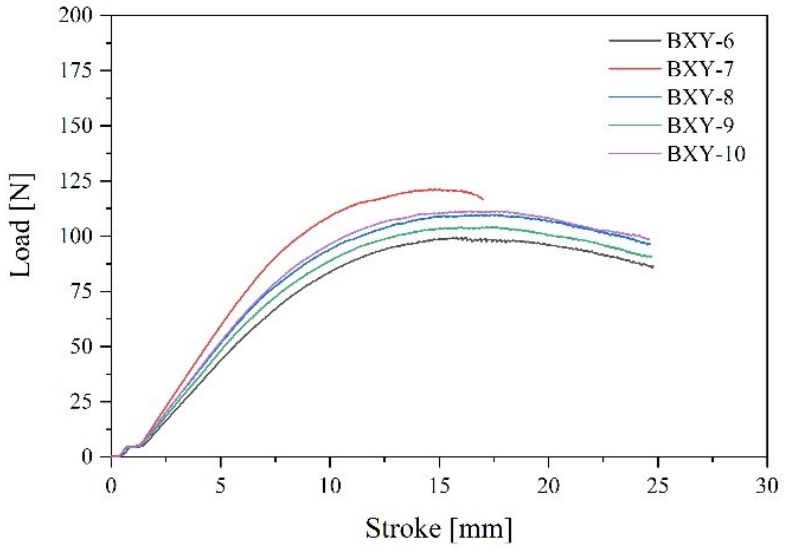

Figure 4.35: Load-Stroke curve for 3-point bending flexural test perform on the specimen unaged printed in position B and direction XY

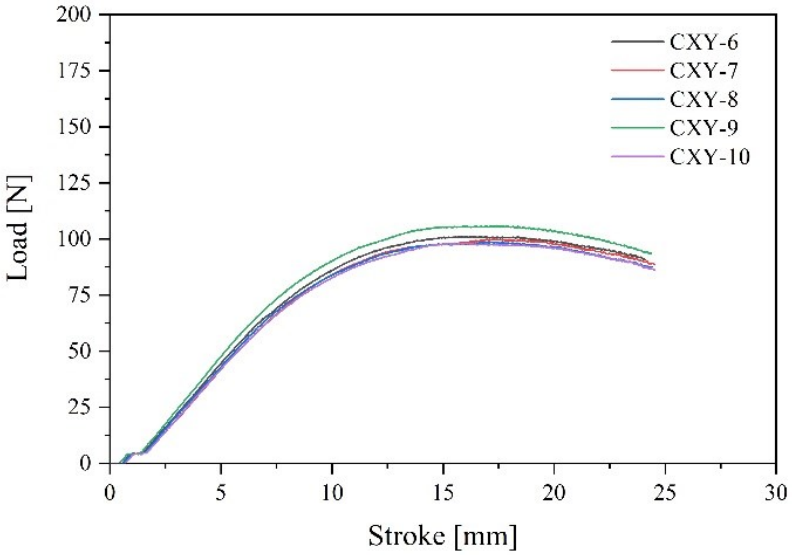

Figure 4.36: Load-Stroke curve for 3-point bending flexural test perform on the specimen unaged printed in position C and direction XY

In Table 4.11 where all the results are summarized, a minimum deviation of the maximum load, between the various moulding positions in the working area, is highlighted. A difference of 6% on the average values is highlighted between position A and C. The greater standard deviation is found in position B, in this position the results are more dispersed.

Table 4.11: Maximum load and stroke at break for scenario α

Time step	Position into the JOB	Maximum Load [N]	Stroke at break [mm]
No aged	AXY	107,13 ± 4,31	No break
No aged	BXY	105,76 ± 5,01	No break
No aged	CXY	100,41 ± 2,68	No break

4.3.2.2 Scenario β) Influence of the samples orientation inside the printed JOB (XY or Z);

Figure 4.37 shows the curve of the 3-Point Bending Flexural test to which the AZ specimens are subjected. These are similar to each other, except for the AZ-9 specimen, which face break earlier than the others, at 21,29 mm. It is however taken into account in the average, since it has a maximum load similar to the others.

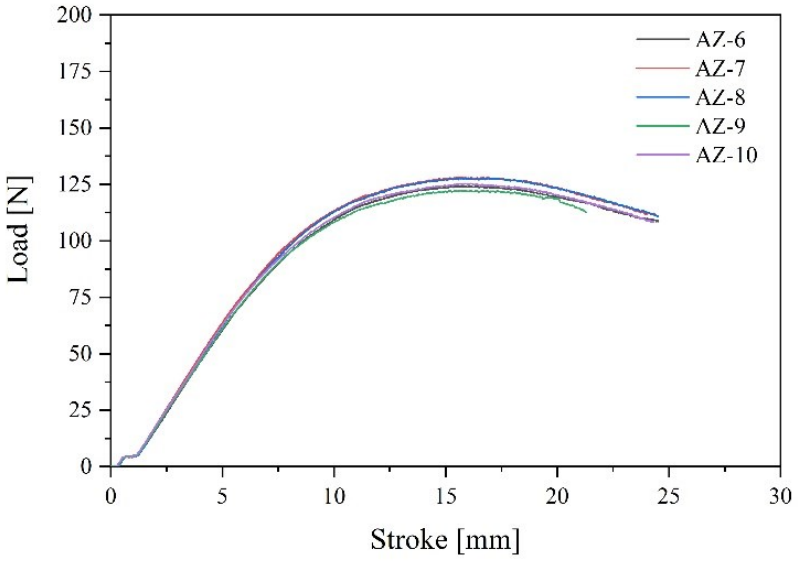

Figure 4.37: Load-Stroke curve for 3-point bending flexural test perform on the specimen unaged printed in position A and direction Z

Compared to the α scenario, there is a greater difference in the maximum load, as regards the printing direction, with a difference of 15% compared to the specimens printed in the same position, but in a direction parallel to the XY plane.

Table 4.12: Maximum load and stroke at break for scenario β

Time step	Printing orientation	Maximum Load [N]	Stroke at break [mm]
No aged	AXY	107,13 ± 4,31	No break
No aged	AZ	125,27 ± 2,14	No break

4.3.2.3 Scenario γ) Effect of the aging over printed samples for 3-time steps (no aged, ⅓ aged, fully aged);

With aging the samples face breaking. Figure 4.38 shows the values of the specimens aged in a climatic chamber for 10 days. Of these only BXY-22 has a similar trend to the same unaged specimens, larger plastic zone. In figure 4.39 we can see how the breakage is ductile, as there is a tightened area in the lower left corner. All the other curves have a mainly linear trend with an almost non-existent plastic zone, this is a symptom of a fragile breaking. The BXY-25 specimen is not taken to account because it is not representative, having an evident printing defect, as seen in figure 4.40. The greater embrittlement is more evident for the specimens aged for the total number of hours.

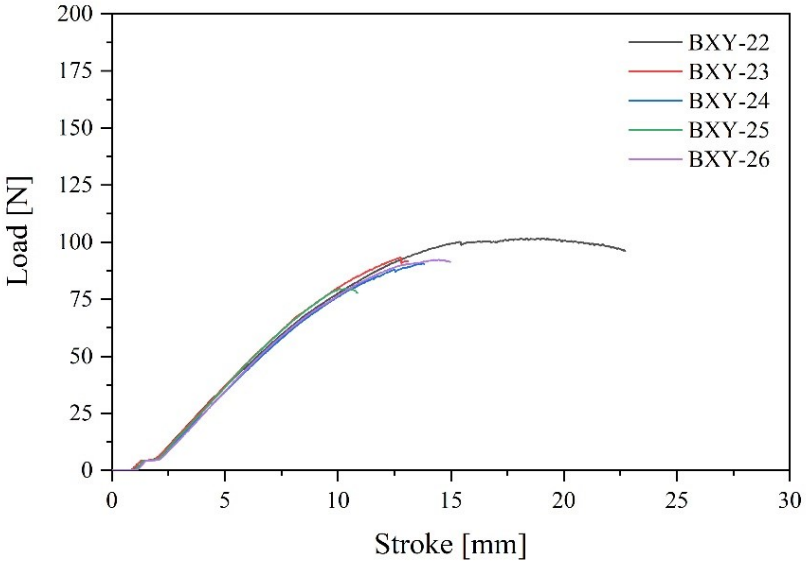

Figure 4.38: Load-Stroke curve for 3-point bending flexural test perform on the specimen 1/3 aged printed in position B and direction XY

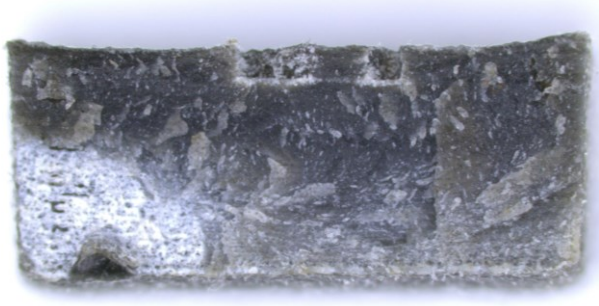

Figure 4.39: Breaking section of a 1/3 aged specimen

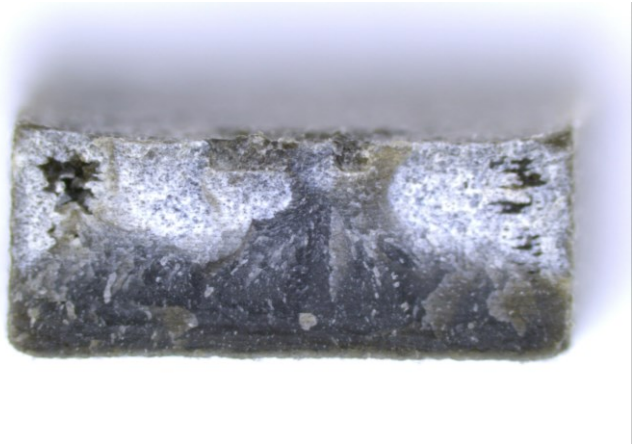

Figure 4.40: Breaking section of a 1/3 aged specimen, BXY-25

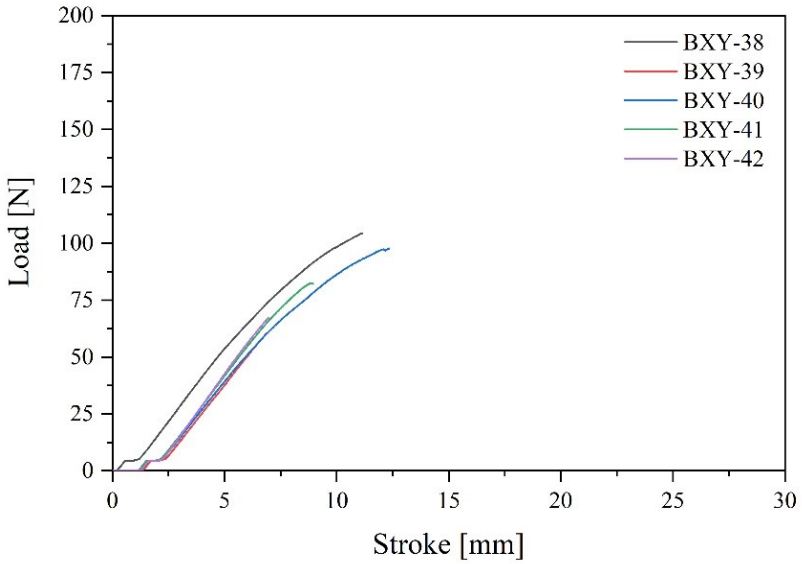

Figure 4.41: Load-Stroke curve for 3-point bending flexural test perform on the specimen fully aged printed in position B and direction XY

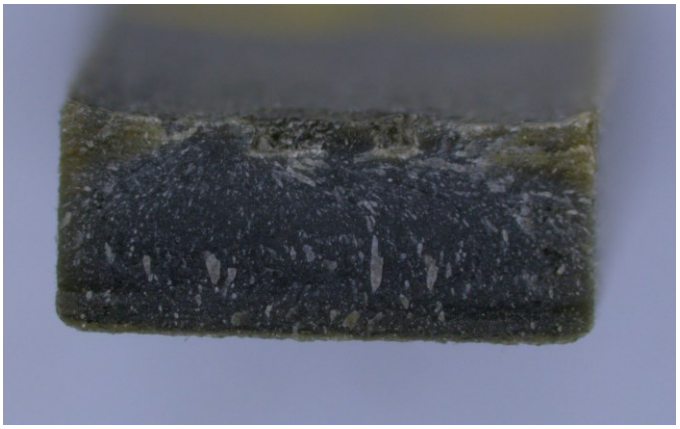

Figure 4.42: Breaking section of a fully aged specimen

The curves, with respect to the various stages of aging, have a very similar trend, this is a symptom of similarity between the heart and skin of the samples, they are homogeneous. Furthermore, also here it is highlighted how the specimens have become brittle by breaking, while those not aged have deformed without breaking. The Maximum Load decreases with a linear trend with respect to the aging steps.

Table 4.13: Maximum load and stroke at break for scenario γ

Time step	Position into the JOB	Maximum Load [N]	Stroke at break [mm]
No aged	BXY	105,76 ± 5,01	No break
1/3 aged	BXY	94,90 ± 3,86	16,13 ± 3,86
Fully aged	BXY	82,62 ± 17,02	9,26 ± 2,12

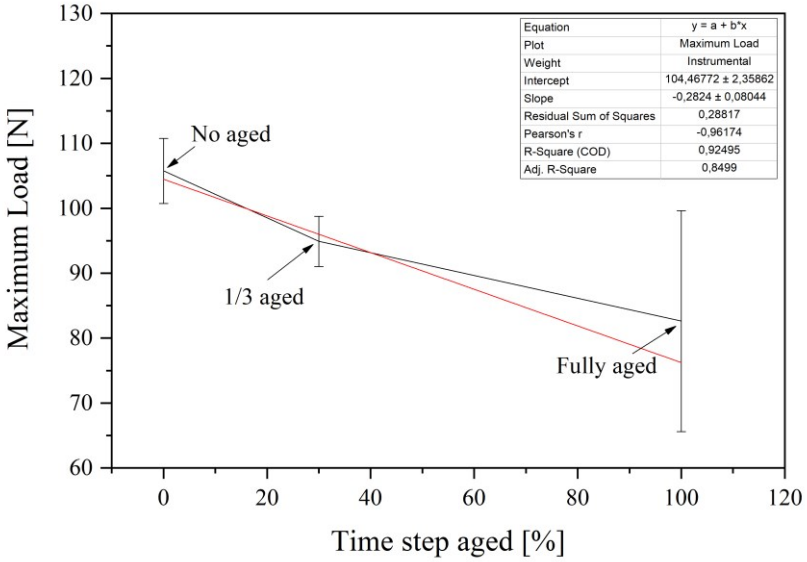

Figure 4.43: Maximum load aging trend

4.3.2.4 Conclusions

Also for the 3-Point Bending Flexural test it is clear that the specimens printed in every position and direction of the JOB have a ductile behavior, having reached the end of the machine stroke. The dispersion of the data in A and B is similar, and is much higher than the curves taken for the specimens printed in position C. For this test there are no large variations on the maximum load values, the greatest difference is 6% between the values in A and C. On the other hand, there is a greater difference as regards a different printing direction, AZ is more resistant to bending.

Already at one third of the total aging time there is a decrease in ductility, because they all undergo breakage. The trend of the maximum force stress values to which the specimens can be subjected is decreasing and, considering the standard deviations, has a linear trend with respect to the time steps. The graphs and curves show a lower dispersion of the data between the various specimens if aged at ⅓, while with complete aging it drastically increases. For a low aging time, therefore, the specimens, if subjected to high temperature and high humidity for a period of 10 days, tend to become uniform while, going on with the test, aging acts in a different way on them, discretizing the results.

4.3.3 Izod Impact Strength test

4.3.3.1 Scenario α) Dependence of the samples position inside the printed JOB;

In the following sub-chapter the readers can find for each position in the working area the summary table of the average results calculated through the equations described in chapter 3 for the Izod Impact Strength test. Through the comparison between the accumulated energies, it can be said that there are no big differences respect to the position in the JOB. In B it is noticed that it is less than 2%.

Table 4.14: Impact strength for scenario α

Time step	Position into the JOB	Impact strength [kJ/m^2]
No aged	AXY	16,83
No aged	BXY	16,49
No aged	CXY	16,79

4.3.3.2 Scenario β) Influence of the samples orientation inside the printed JOB (XY or Z);

In AZ the Impact strength value decreases by 7% respect to that one printed with orientation XY,, it is a little more fragile, it accumulates less energy on impact.

Table 4.15: Impact strength for scenario β

Time step	Printing orientation	Impact strength [kJ/m^2]
No aged	AXY	16,83
No aged	AZ	15,69

4.3.3.3 Scenario γ) Effect of the aging over printed samples for 3-time steps (no aged, ⅓ aged, fully aged);

When aging is complete, the accumulated energy is about half. In fact, as can be seen from graph 4.44, the Impact strength decreases with an exponential trend.

Table 4.16: Impact strength for scenario γ

Time step	Position into the JOB	Impact strength [kJ/m^2]
No aged	BXY	16,49
1/3 aged	BXY	10,65
Fully aged	BXY	7,155

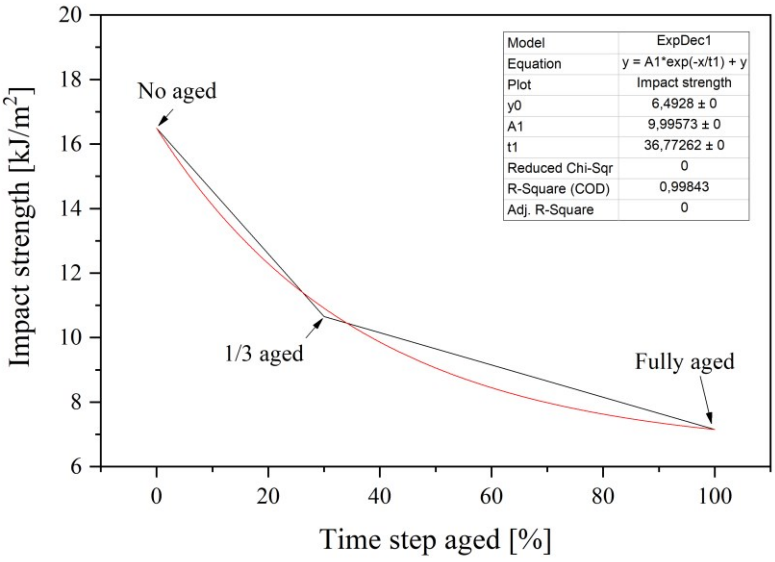

Figure 4.44: Impact strength aging trend

4.3.3.4 Conclusions

Results taken for the Izod Impact Strength test cannot be compared with those provided by HP as they are collected through the adaptation of a Charpy pendulum to an Izod test. The difference is in the length of the arm. However, a comparison between the results taken for each scenario, that is the aim of this thesis, can be done. There are no big differences respect to the position in the JOB, it may be due to a lesser perception of the difference. In fact, in accordance with the results obtained from the tensile test, in B we obtain a lower impact energy value of 2%. This confirms the production of less ductile specimens in this position. Always in accordance with tensile testing are the results obtained in position A with different molding orientation. In AZ the Impact strength is less than 7%. An important embrittlement is also noticeable at a low accelerated aging time.

4.3.4 Microindentation Hardness testing

4.3.4.1 Scenario α) Dependence of the samples position inside the printed JOB;

For Microindentation Hardness testing, bar graphs have been created that correspond to the average of the values taken in each specimen printed in the position shown in the abscissa. There are no major differences between them, more than anything else a dispersion of the data in C. An example of an incision made by the Vickers indenter on the less rough surface is shown in figure 4.46.

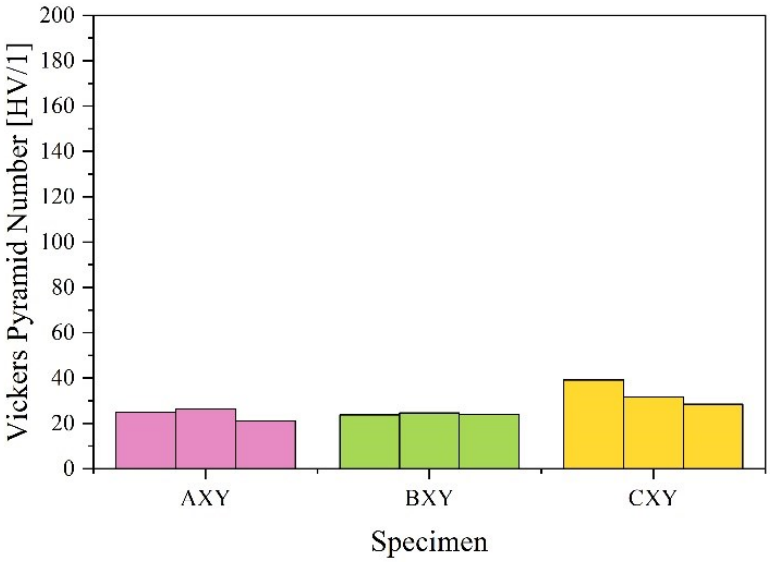

Figure 4.45: Vickers pyramid number for scenario α

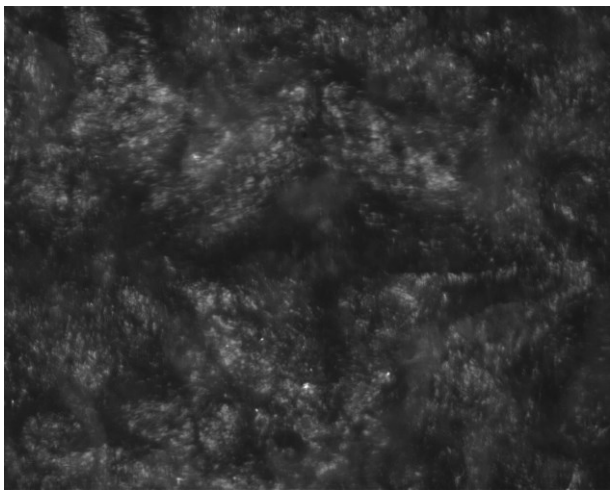

Figure 4.46: Groove made by Vickers indenter on no aged surface

4.3.4.2 Scenario β) Influence of the samples orientation inside the printed JOB (XY or Z);

There are no major differences even regarding the printing orientation, more than anything else, a dispersion of data in AZ.

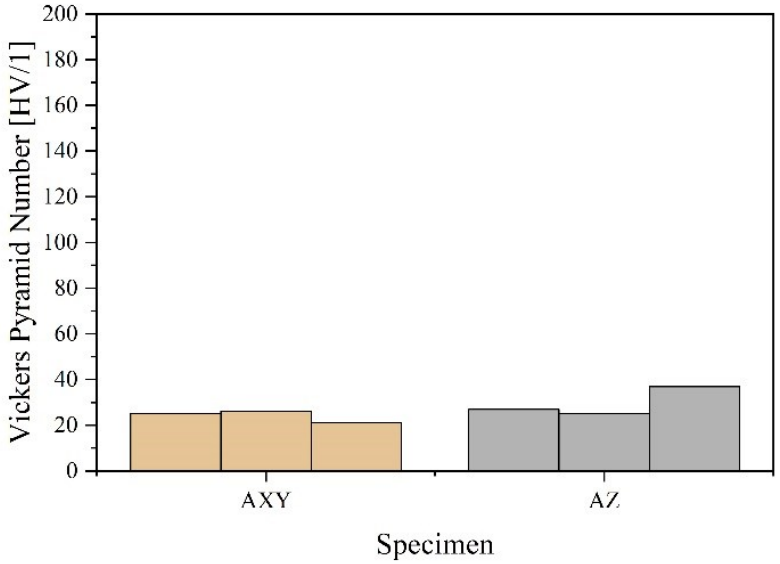

Figure 4.47: Vickers pyramid number for scenario β

4.3.4.3 Scenario γ) Effect of the aging over printed samples for 3-time steps (no aged, ⅓ aged, fully aged);

With aging, on the other hand, it can be notice how the specimens become much harder, the Vickers number (HV / 1) grows exponentially.

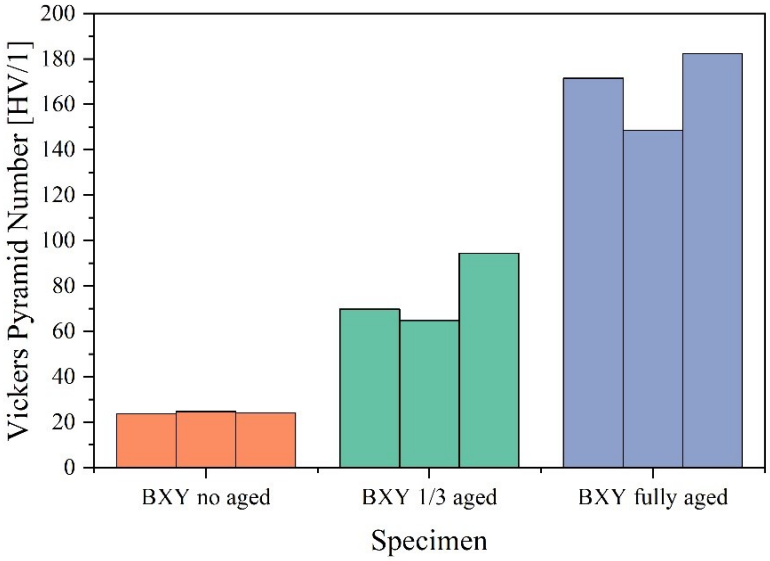

Figure 4.48: Vickers pyramid number for scenario γ

Figure 4.49 shows the cross-shaped incisions made by the inventor Vickers on the surfaces of 3 specimens with different aging stages. It is noticed how the crosses decrease in length and also an increase in surface homogeneity, although the least rough surface is represented, or rather, the one corresponding to the first layers of each specimen.

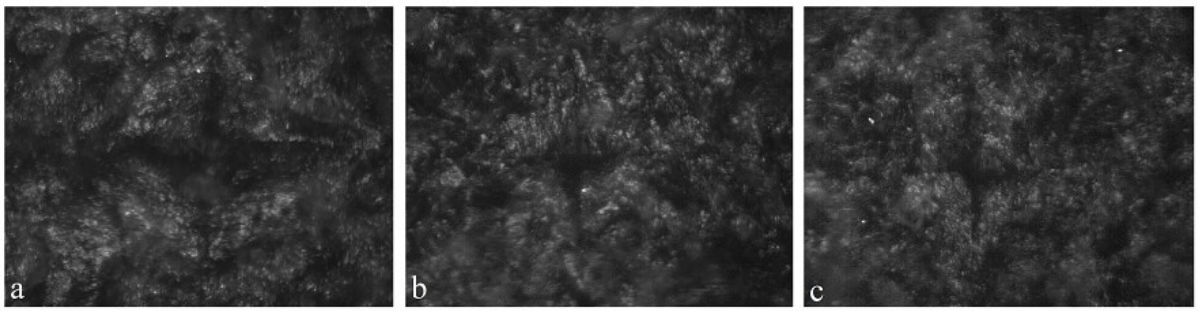

Figure 4.49: Grooves made by Vickers indenter on surfaces subjected to different aging step: a) no aged, b) 1/3 aged c) fully aged

4.3.4.4 Conclusions

As can be found in the literature, there are many mistakes that can be made through this tool, considering the difficulty in taking the results. There are many factors that can influence the quality of microindentation test results. Such as, for example, the heterogeneity of the specimens, the accuracy of the operator, the optical distortion, the non-uniformity of illumination, the lateral movement of the indenter or specimen. Furthermore, from my experience with this measuring instrument, it is important to highlight the difficulty in carrying out the measurement due to the non-homogeneity of the surface.

Considering therefore that this test measures the hardness of the specimens in a microscopic way, it can be said that no differences were found based on the moulding position, not even the direction. A big difference, on the other hand, was noted in accelerated aging. Here the hardness, even already at a third, increases dramatically.

Considering therefore that this test measures the hardness of the specimens in a microscopic way, it can be said that no differences were found based on the molding position, not even the direction. A big difference, on the other hand, was noted in accelerated aging. Here the hardness, even already at a third increases dramatically.

4.3.5 Shore Hardness testing

4.3.5.1 Scenario α) Dependence of the samples position inside the printed JOB;

As for Shore Hardness testing, the readers immediately notice how the front part has a greater hardness than the area subject to the capillarity defect. There is no big difference between the positions, position C is the hardest microscopically.

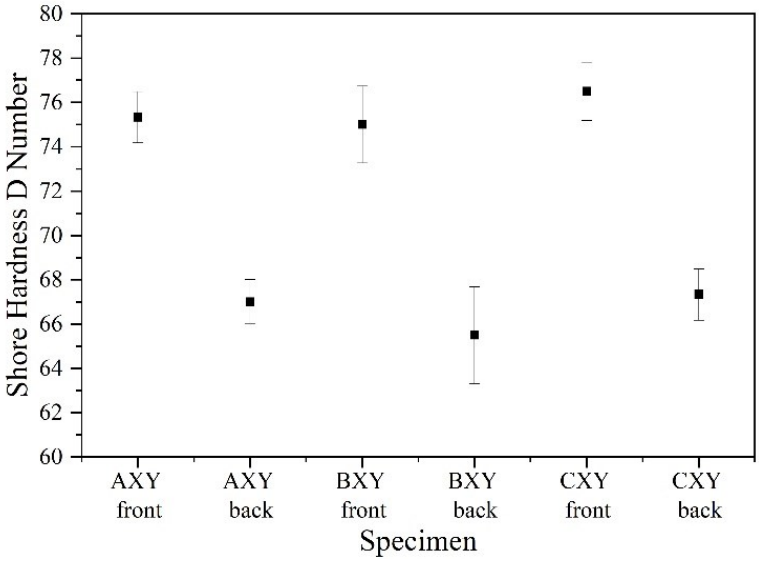

Figure 4.50: Shore hardness D number for scenario α

4.3.5.2 Scenario β) Influence of the samples orientation inside the printed JOB (XY or Z);

Specimens printed in the Z direction have a very low, almost imperceptible standard deviation and its two surfaces are uniform to each other, indicating that cooling matters in the distribution of behavior.

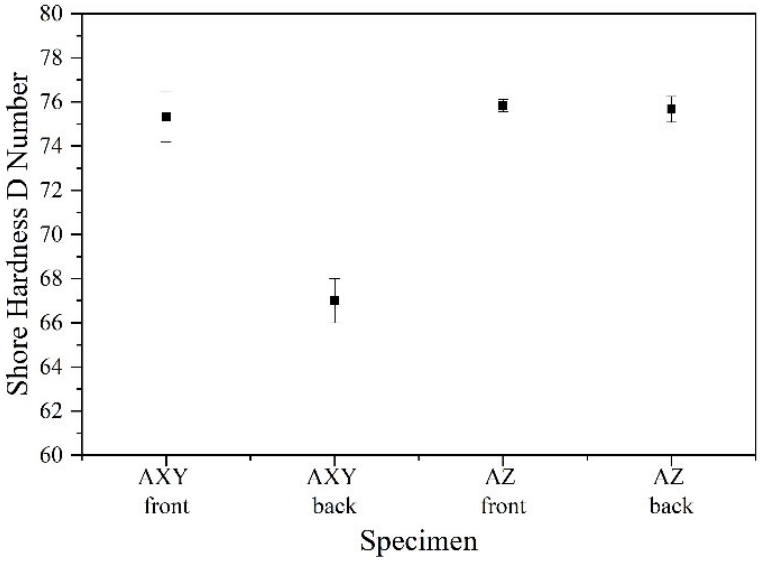

Figure 4.51: Shore hardness D number for scenario β

4.3.5.3 Scenario γ) Effect of the aging over printed samples for 3-time steps (no aged, ⅓ aged, fully aged);

Aged specimens follow the same trend, but they have more uniform values than non-aged ones, have a low standard deviation.

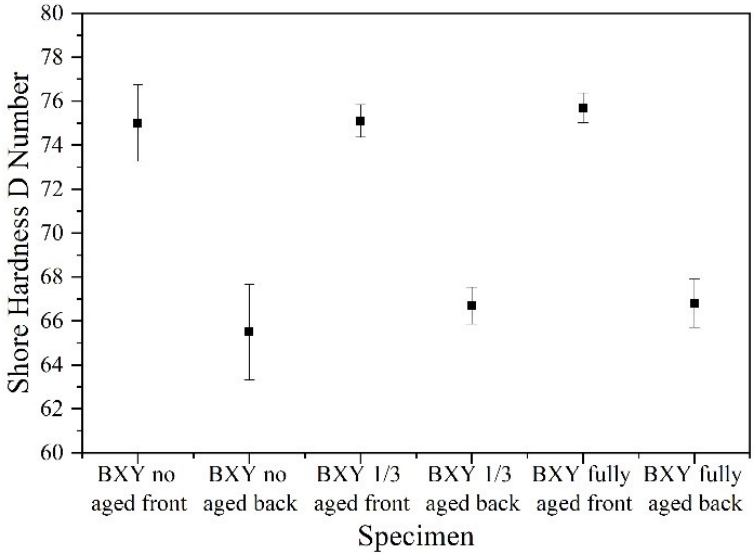

Figure 4.52: Shore hardness D number for scenario γ

4.3.5.4 Conclusions

It is important to highlight that Shore Hardness testing is a test that measures hardness in a macroscopic way. The greatest variations in hardness can be seen on the same specimen, where the rougher surface has a lower hardness than the less rough surface. The differences, on the other hand, are minimal as regards the scenarios. However, it is possible to highlight a higher hardness for the specimens in position C, the homogeneity between the hardness of the surfaces of the AZ specimens, a minimum standard deviation for the AZ specimens and for the aged BXY specimens.

5. Conclusions

This study is devoted to broaden the knowledge on the conformity and applicability of the components produced through the Additive Manufacturing technology created by the company HP Inc., the Multi Jet Fusion (MJF). Analysing the evolution of the chemical, thermal and mechanical properties of Polyamide 12 (PA12) components in relation to their position in the printing area, orientation and aging, this aim is been reached. Assuming the specimen's characteristics as symmetrical in the printing area, three points considered cruxes are analysed, in the research this is called scenario α. The samples, with their dimensions dictated by the specific standards, are printed in these points, and with different printing orientations, scenario β. Regarding accelerated aging, the "Environmental specification for electrical/electronic (E/E) components" is followed, relating to Valeo Santena product line, the "Interior Switches and Control" (ISC). This means that the specimens, tested in a climatic chamber where Temperature and Humidity are controlled, are inspected at ⅓ and at the end of the vehicle's life, scenario γ.

The material is characterized by means of infrared spectrophotometry in attenuated total reflectance (FTIR-ATR), to examine the functional groups. The thermal analysis used is differential scanning calorimetry (DSC). As for the mechanical tests, the evolution of Young modulus (E), elongation at break, yield and ultimate tensile strength, are observed through the tensile testing. The maximum load and stroke at break, through the three-point bending flexural test. To determine the notch toughness of the material, the Izod impact strength test is also carried out, designing the indenter and the base with the annexed vise. Lastly, the hardness with a Shore durometer type D and the microindentation hardness testing with the Vickers indenter.

The results that this study has obtained, based on each scenario are:

1) **Scenario α** - there are no variations in the macromolecule that is possible to identify like PA12, also no changes on the glass transition temperature and on the melting temperature, with values like the one found in literature. On the other hand, higher percentages of crystallinity are evaluated for the specimens printed in position B. The tensile testing showed ductile behaviours for all the characterized zones of the working area, also confirmed with the 3-point bending flexural test, but variations have been found, especially for position B. These specimens have a more fragile behavior but, as the yield point increases, at the static design level, the expected response should not differ much from that of the specimens in the other positions. To confirm this, it would be necessary to perform fatigue tests on the components, this position could be the binding one having shorter durations. Furthermore, in B the data are more dispersed. By bending instead there are variations of 6% on the maximum load values between A and C. Even if the change is minimal, on impact, a decrease of the energy absorbed by the specimens B is still less than 2%. On the other hand, there are no differences in terms of micro-hardness and even through Shore Hardness testing. The greatest variations in hardness can be seen on the same specimen, where the rougher surface has a lower hardness than the less rough surface.
2) **Scenario β** - there are no variations in the macromolecule that is possible to identify like PA12, also no changes on the glass transition temperature and on the melting temperature, with values like the one found in literature. The tensile testing shows ductile behaviours for both orientations, also confirmed with the 3-point bending flexural test, but variations are found. The Z direction is the one that has greater stiffness and less ductility. In bending, on the other hand, the specimens printed in the

Z direction, have greater resistance than those oriented according to the XY plane. Even if low, at impact, a decrease in the energy absorbed by the AZ specimens is nevertheless noticed. On the other hand, there are no differences in terms of micro-hardness and even through Shore Hardness testing.

3) **Scenario γ** - there are no variations in the macromolecule that is possible to identify like PA12 and no changes in the melting Temperature, with values like the one found in literature. The high temperature and high humidity create another inflection in the DSC curve in addition to that of the glass transition temperature, it is necessary to study this effect in more detail with other types of tests. Furthermore, the effect on the percentage of crystallinity is variable according to the aging step to which the specimen has been subjected, it decreases to one third of the total aging and increases when it is subjected to the complete test. All the data seem to indicate that, with aging, the material loses mechanical properties and becomes more brittle with properties decreasing exponentially, except for the elongation at break which decreases linearly with the time step. This embrittlement result is also evident for the bending test and the Izod Impact Strength test. A big difference in hardness was noticed at accelerated aging, where already at one third it increases drastically, but it must be considered that this measures the hardness of the specimens in a microscopic way. However, minimal variations were found during the Shore Hardness testing, which measures the hardness in a macroscopic way.

Although the transition from rapid prototyping to serial production is not immediate, it is still important to continue these preliminary studies to better understand these technologies. The continuation of this research, which brings new information to the basic knowledge of Multi Jet Fusion technology, could be the comparison with the injection moulded PA12 specimens, proceeding with the same tests carried out in this thesis with a greater number of specimens, also printed for several JOBs. Furthermore, to better investigate at a microscopic level what is the combined effect of high temperature and high humidity, it would be necessary to carry out deepened analyses, for example with XRD.

References

Aharoni, S.M. (1997) *N-nylons: Their synthesis, structure and properties*. Chichester, England: Wiley.

Alomarah, A. et al. (2019) "Compressive properties of a novel additively manufactured 3D auxetic structure," *Smart Materials and Structures*, 28(8), p. 085019. Available at: https://doi.org/10.1088/1361-665x/ab0dd6.

American Society for Testing and Materials International (2017) *D6272 − 17, Standard test method for flexural properties of unreinforced and reinforced plastics and electrical insulating materials by four-point bending*. West Conshohocken, PA, United States: ASTM International.

American Society for Testing and Materials International (2008) *D785 − 08, Standard Test Method for Rockwell Hardness of Plastics and Electrical Insulating Materials*. West Conshohocken, PA, United States: ASTM International.

American Society for Testing and Materials International (2013) *D7426-08, Standard Test Method for Assignment of the DSC Procedure for Determining Tg of a Polymer or an Elastomeric Compound*. West Conshohocken, PA, United States: ASTM International.

American Society for Testing and Materials International (2014) *D638 − 14, Standard Test Method for Tensile Properties of Plastics*. West Conshohocken, PA, United States: ASTM International.

American Society for Testing and Materials International (2017) *E384 − 17, Standard Test Method for Microindentation Hardness of Materials*. West Conshohocken, PA, United States: ASTM International.

American Society for Testing and Materials International (2010) *D256 − 10, Standard Test Methods for Determining the Izod Pendulum Impact Resistance of Plastics*. West Conshohocken, PA, United States: ASTM International.

American Society for Testing and Materials International (2015) *D2240 − 15, Standard Test Method for Rubber Property—Durometer Hardness*. West Conshohocken, PA, United States: ASTM International.

CustomPartNet (2008) *Schematic representation of FDM technique, CUSTOMPART.NET*. Available at: https://www.custompartnet.com/ (Accessed: September 12, 2022).

CustomPartNet (2008) *Schematic representation of PolyJet technology, CUSTOMPART.NET*. Available at: https://www.custompartnet.com/ (Accessed: September 15, 2022).

CustomPartNet (2008) *Schematic representation of SLA technology, CUSTOMPART.NET*. Available at: https://www.custompartnet.com/ (Accessed: September 13, 2022).

CustomPartNet (2008) *Schematic representation of SLS technique, CUSTOMPART.NET*. Available at: https://www.custompartnet.com/ (Accessed: September 15, 2022).

Ellis, A., Noble, C.J. and Hopkinson, N. (2014) "High speed sintering: Assessing the influence of print density on microstructure and mechanical properties of nylon parts," *Additive Manufacturing*, 1-4, pp. 48–51. Available at: https://doi.org/10.1016/j.addma.2014.07.003.

FCA US - Quality & Reliability Engineering - 5200 and FCA ITALY - Electrical/Electronics - Electronic Architecture, Talevski, M. and Molina, A. (2015) *CS.00056 - Environmental specification for Electrical / Electronic (E/E) components*. Fiat Chrysler Automobiles.

Ferrari (2019) *Ferrari's Steering wheel with capacitive buttons and switches, Ferrari*. Available at: https://www.ferrari.com/it-IT/auto/gamma (Accessed: November 2, 2022).

Fontana, M.G. (2005) "Chapter 5," in *Corrosion Engineering*. 3°. New Delhi, India: Tata McGraw-Hill, pp. 219–271.

Goglio, L. (2015) *Resistenza dei Materiali e Dei collegamenti*. Torino, Italy: Levrotto & Bella.

HP Inc. (2020) *White paper | HP 3D Printing materials for the HP Jet Fusion 5200 Series 3D Printing Solution - Mechanical Properties*. HP Development Company, L.P.

HP Inc. (2022) *Tecnologia di Stampa 3D hp multi jet fusion - stampante 3D per fusione di letto di polvere, Tecnologia di stampa 3D HP Multi Jet Fusion - Stampante 3D per fusione di letto di polvere* | HP® Italia. Available at: https://www.hp.com/it-it/printers/3d-printers/products/multi-jet-technology.html (Accessed: September 20, 2022).

Maserati (2013) *Maserati's Steering wheels with mechanical buttons and switches, Maserati*. Available at: https://www.maserati.com/it/it/modelli (Accessed: November 2, 2022).

Mele, M. et al. (2020) "Investigation into effects of cooling rate on properties of polyamide 12 parts in the multi jet fusion process," *Rapid Prototyping Journal*, 26(10), pp. 1789–1795. Available at: https://doi.org/10.1108/rpj-04-2020-0080.

Mele, M., Campana, G. and Monti, G.L. (2021) "Modelling of the capillarity effect for cylindrical shapes in multi jet fusion technology," *Progress in Additive Manufacturing*, 6(4), pp. 859–869. Available at: https://doi.org/10.1007/s40964-021-00200-7.

Morales-Planas, S. et al. (2018) "Multi Jet Fusion PA12 manufacturing parameters for watertightness, strength and tolerances," *Materials*, 11(8), p. 1472. Available at: https://doi.org/10.3390/ma11081472.

O'Connor, H.J., Dickson, A.N. and Dowling, D.P. (2018) "Evaluation of the mechanical performance of polymer parts fabricated using a production scale multi jet fusion printing process," *Additive Manufacturing*, 22, pp. 381–387. Available at: https://doi.org/10.1016/j.addma.2018.05.035.

Piergiovanni, L. and Limbo, S. (2010) "Chapter 8," in *Food Packaging Materiali, Tecnologie e qualità degli alimenti*. Milano, Italia: Springer Milan, pp. 205–238.

Quinlan, H.E. et al. (2017) "Industrial and consumer uses of Additive Manufacturing: A discussion of capabilities, trajectories, and challenges," *Journal of Industrial Ecology*, 21(S1). Available at: https://doi.org/10.1111/jiec.12609.

Riedelbauch, J., Rietzel, D. and Witt, G. (2019) "Analysis of material aging and the influence on the mechanical properties of Polyamide 12 in the multi jet fusion process," *Additive Manufacturing*, 27, pp. 259–266. Available at: https://doi.org/10.1016/j.addma.2019.03.002.

Rahim T. N. A. T., et al. (2017) "The improvement of mechanical and thermal properties of polyamide 12 3D printed parts by fused deposition modelling", *Express Polymer Letters*, 11, 12, 963–982.

Rosso, S. et al. (2020) "In-depth comparison of polyamide 12 parts manufactured by Multi Jet Fusion and Selective Laser Sintering," *Additive Manufacturing*, 36, p. 101713. Available at: https://doi.org/10.1016/j.addma.2020.101713.

Salmoria, G.V., Leite, J.L. and Paggi, R.A. (2009) "The microstructural characterization of PA6/PA12 blend specimens fabricated by Selective Laser Sintering", *Polymer Testing*, 28(7), pp. 746–751. Available at: https://doi.org/10.1016/j.polymertesting.2009.06.010.

Scherer, B., Kottenstedde, I.L. and Matysik, F.-M. (2020) "Material characterization of polyamide 12 and related agents used in the multi-jet Fusion Process: Complementary application of high-resolution mass spectrometry and other advanced instrumental

techniques," *Monatshefte für Chemie - Chemical Monthly*, 151(8), pp. 1203–1215. Available at: https://doi.org/10.1007/s00706-020-02646-x.

Singh, A.P. and Pervaiz, S. (2021) "Current status and prospects of Multi-Jet Fusion (MJF) based 3D printing technology," *Volume 2A: Advanced Manufacturing* [Preprint]. Available at: https://doi.org/10.1115/imece2021-73547.

Smith, J.G., Menichetti, S. and Capperucci, A. (2018) "Chapter 3," in *Fondamenti di Chimica Organica*. Milano etc., Italy: McGraw-Hill education.

Stagnaro, P., Luciano, G. and Utzeri, R. (2016) "La calorimetria differenziale a scansione e l'analisi termogravimetrica nella caratterizzazione termica dei materiali polimerici." Available at: https://moodle2.units.it/pluginfile.php/283832/mod_resource/content/1/Appunti-%20DSC-TGA.pdf (Accessed: November 5, 2022). Istituto per lo Studio delle Macromolecole del CNR, ISMAC-CNR, Genova

Umeda R.E., et al. (2022) "Simulation of Hydrolytic Ring Opening Polymerization of Nylon 12 from Laurolactam", *Chemical Engineering Transactions*, 92, 613-618 DOI:10.3303/CET2292103

Valeo S.p.a (2021) *Our story, Valeo*. Available at: https://www.valeo.com/en/our-story/ (Accessed: November 3, 2022).

Wang, Y. et al. (2020) "Current status and prospects of polymer powder 3D printing technologies," *Materials*, 13(10), p. 2406. Available at: https://doi.org/10.3390/ma13102406.

Wohlers, T. and Campbell, R.I. (2017) Wohlers report 2017: 3D Printing and Additive Manufacturing State of the industry: Annual worldwide progress report. Fort Collins, CO, United States: Wohlers Associates, Inc.